DEPARTMENT OF PHYSICS, UNIVERSITY OF JYVÄSKYLÄ
RESEARCH REPORT No. 7/2000

SHAPE COEXISTENCE IN Hg, Tl AND Pb NUCLEI BEYOND THE 82<N<126 MID-SHELL

BY
MAARIT MUIKKU

Academic Dissertation
for the Degree of
Doctor of Philosophy

Jyväskylä, Finland
August, 2000

URN:ISBN:978-951-39-9492-1
ISBN 978-951-39-9492-1 (PDF)
ISSN 0075-465X

Jyväskylän yliopisto, 2023

ISBN 951-39-0769-4
ISSN 0075-465X

DEPARTMENT OF PHYSICS, UNIVERSITY OF JYVÄSKYLÄ
RESEARCH REPORT No. 7/2000

SHAPE COEXISTENCE IN Hg, Tl AND Pb NUCLEI BEYOND THE 82<N<126 MID-SHELL

BY
MAARIT MUIKKU

Academic Dissertation
for the Degree of
Doctor of Philosophy

To be presented, by permission of the
Faculty of Mathematics and Natural Sciences
of the University of Jyväskylä,
for public examination in Auditorium FYS 1 of the
University of Jyväskylä on September 22, 2000,
at 12 o'clock noon

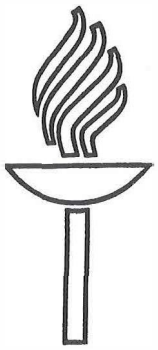

Jyväskylä, Finland
August, 2000

Preface

This work has been carried out at the Department of Physics of the University of Jyväskylä during the years 1996-2000.

First of all, I would like to express my sincere gratitude to the leader of the γ group and my supervisor Prof. Rauno Julin for his guidance and encouragement during the course of this thesis. I am also grateful to Dr. Sakari Juutinen and Dr. Pete Jones who patiently guided me into the secrets of the measurement electronics and data analysis. I want to thank the leader of the RITU group Prof. Matti Leino for introducing me the world of α-spectroscopy. Thanks go also to all group members of the RITU-γ group. It has been a great pleasure to work in such a competent and inspiring group as the RITU-γ group.

I want to express my warm thanks to the staff of the Department of Physics for the friendly and stimulating atmosphere. It really has been a privilege to work at the Department. I also would like to thank the foreign collaborators for their valuable help in the measurements discussed in this thesis.

The financial support from the University of Jyväskylä, the Graduate School of Particle and Nuclear Physics, the Academy of Finland, Emil Aaltosen Säätiö and Suomen Kulttuurirahasto are gratefully acknowledged.

I am deeply indebted to my friends for the numerous discussions, which renewed my belief in this work. Finally, I would like to thank my family for their support and Markku for his encouragement and patience during these years.

Jyväskylä, August 2000

Maarit Muikku

Abstract

In this thesis coexisting structures in the neutron-deficient ^{174,176,177}Hg, ^{183}Tl and ^{182,184}Pb nuclei have been studied at the Accelerator Laboratory of the University of Jyväskylä. To probe these nuclei in the close vicinity of the proton drip-line the Recoil-Decay-Tagging (RDT) technique based on the use of a germanium detector array in conjunction with the gas-filled recoil separator RITU has been utilised. The excited states have been observed for the first time in ^{174,177}Hg and ^{182,184}Pb nuclei. The energies of newly observed levels in ^{176}Hg and the band-head of the yrast $\pi i_{13/2}$ band in ^{183}Tl have been determined. The experimental results are compared both to the level-energy systematics of the heavier isotopes and theoretical predictions. The new results are in accordance with the scheme of the intruding prolate-deformed structures minimising their energies near the N=104 neutron mid-shell in Hg and Pb nuclei.

TABLE OF CONTENTS

1. Introduction

To achieve a better understanding of the nuclear structure and nucleon-nucleon interactions, the limits of the applicability of theoretical models have to be tested by probing nuclei under extreme conditions. This can be done, for example, by studying exotic nuclei having extreme values of the neutron to proton ratio or probing the level structures of nuclei at high spin. The primary aim of the present work was to extend the knowledge of the coexistence of different shapes in very neutron-deficient nuclei beyond the neutron mid-shell near the Z=82 shell gap. The present in-beam studies were focused on Hg, Tl and Pb nuclei lying very close to the proton drip line as seen in Figure 1.1, where the part of the nuclear chart relevant for the present work is shown. In this work excited states were observed for the first time in $^{182,\ 184}$Pb and ^{174}Hg nuclei.

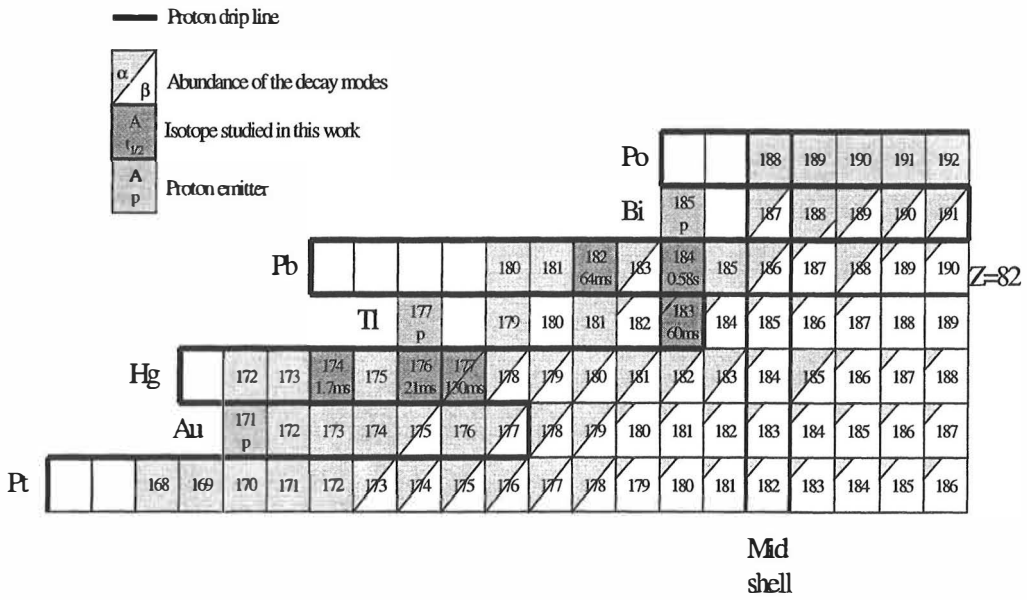

Figure 1.1 Part of the nuclear chart relevant for the present work. Identified isotopes have been marked with the mass number. The proton drip line [Lir76], the Z=82 closed shell and the N=104 neutron mid-shell have been marked with the thick lines.

There exists a large body of experimental information supporting the coexistence of deformed and near-spherical states at low excitation energies in the nuclei near the

Z=82 closed shell. Although the ground states of Pb nuclei with the Z=82 closed proton shell are considered to have spherical shape, low-lying states based on both oblate and prolate structures have been observed near the 82<N<126 mid-shell [All98, And00]. In Hg isotopes these low-lying deformed intruder states have been observed to minimise their energies near the neutron mid-shell. These intruder structures can be associated with two-proton excitations across the shell gap. When exciting one (or more) proton pair(s) to an orbit above the shell gap a large effective number of valence protons are formed. The term valence protons includes both the protons and the holes. The low excitation energy of intruder states is explained to result from the combined effect of the pairing interactions and the large gain from the residual proton-neutron interaction between the particle-hole configurations and the valence neutrons [Hey87]. Near the neutron mid-shell the number of the valence neutrons is highest and, therefore, the gain in excitation energy is also largest. Another way to describe the intruder states is to use, for example, the Nilsson model [Nil55]. In the Nilsson model the single-particle energies for protons and neutrons are calculated in an axially symmetric deformed potential. According to this model, the conserved quantum numbers are the parity (π) and the projection of the angular momentum on the symmetry axis (Ω). The low-Ω orbits have a large spatial overlap with a prolate deformed core and thus, they are lowered in energy when going towards more prolate deformation. Likewise the high-Ω orbits overlap with an oblate core and are lowered in energy with increasing oblate deformation. The energy needed for exciting protons across the shell gap is lowered dramatically compared to the spherical situation.

For in-beam spectroscopic studies the neutron-deficient Hg, Tl and Pb isotopes studied in this work can only be produced using heavy-ion induced fusion-evaporation reactions. However, in the reactions used in the present work over 90% of the total cross section goes into the fission channels. Furthermore, the channel of interest covers only a small fraction of the total fusion-evaporation cross-section. The typical cross-sections for the reactions used to produce the nuclei of interest in this work range from some hundreds of nanobarns to some microbarns. In in-beam γ-ray spectroscopic studies γ rays are detected at the target area. Most of the γ rays detected originate from the unwanted reaction products. Therefore, the separation of the

channel of interest, not only from the fission products but also from the stronger evaporation channels, is essential.

Several methods to separate the fusion-evaporation channels from each other and from the fission background have been developed for γ-ray spectroscopy. For example, by detecting α particles, protons and neutrons evaporated in the reaction the reaction channel leading to the nucleus of interest can be selected [Kur92, Sar96, Sav98]. The actual reaction products can also be detected. For instance, a recoil filter detector (RFD) [Hee93] has been used to separate fusion evaporation channels from the fission background. In α-decay studies recoil separators have been successfully used to separate fusion evaporation products from the unwanted background of fission fragments, projectiles and target-like products [e.g. Lei95b, Tot99]. A powerful tool to probe the structure of nuclei produced via weak fusion-evaporation channels is formed when a recoil separator is combined with an efficient γ-ray detector array for detecting prompt γ rays from the target [Sch86, Sim86].

In the present work the Recoil-Decay-Tagging (RDT) method based on use of the combination of a γ-ray detector array and a recoil separator is employed to study the nuclei of interest. The basic idea of the method is to identify a recoil via its characteristic radioactive decay. Only those γ-ray events detected at the same time with the identified recoil are accepted. The method was first used at GSI to probe the shape of ^{180}Hg [Sch86, Sim86]. At the Department of Physics, University of Jyväskylä (JYFL), first tests to combine a γ-ray detector array and the gas-filled recoil separator RITU were performed in 1995. The results obtained were promising. Since then several efficient γ-ray detector arrays have been used in conjunction with RITU. These set-ups have been employed in more than 50 experiments to study neutron-deficient nuclei with the proton number ranging from 53 to 103. The most recent of these arrays is Jurosphere II. The experiments discussed in this work demonstrate well the power of the RDT method.

A part of the results presented in this work has been reported also in the following publications:

1. M. Muikku, J.F.C. Cocks, P.T. Greenlees, K. Helariutta, P.M. Jones, R. Julin, S. Juutinen, H. Kankaanpää, H. Kettunen, P. Kuusiniemi, M. Leino, R.D. Page, P. Rahkila, A. Savelius, W.H. Trzaska and J. Uusitalo
   Probing the shape of ^{176}Hg along the yrast line
   Phys. Rev. C **58**, R3033 (1998)
   https://doi.org/10.1103/PhysRevC.58.R3033
2. J.F.C. Cocks, M. Muikku, W. Korten, R. Wadsworth, S. Chmel, J. Domscheid, P.T. Greenlees, K. Helariutta, I. Hibbert, M. Houry, D. Jenkins, P. Jones, R. Julin, S. Juutinen, H. Kankaanpää, H. Kettunen, P. Kuusiniemi, M. Leino, Y. Le Coz, E. Mergel, R.D. Page and A. Savelius
   First observations of excited states in ^{184}Pb; Spectroscopy beyond the neutron mid-shell
   Eur. Phys. J. A **3**, 17 (1998)
   https://doi.org/10.1007/s100500050144
3. D.G. Jenkins, M. Muikku, P.T. Greenlees, K. Hauschild, K. Helariutta, P.M. Jones, R. Julin, S. Juutinen, H. Kankaanpää, N.S. Kelsall, H. Kettunen, P. Kuusiniemi, M. Leino, C. Moore, P. Nieminen, C.D. O'Leary, R.D. Page, P. Rahkila, W. Reviol, M. Taylor, J. Uusitalo and R. Wadsworth,
   First observation of excited states in ^{182}Pb
   Phys. Rev. C **62**, 021302(R) (2000)
   https://doi.org/10.1103/PhysRevC.62.021302

2. Theoretical aspects

The nuclear shell model has proved to be an important tool when trying to describe quantitatively the behaviour of nuclei. The basic assumption of the shell model is that the nucleons move independently of each other in an average central potential created by themselves. The shell model has been successful both in reproducing the experimentally observed magic numbers and in explaining the basic properties of spherical nuclei near the closed shells. For the region between the closed shells the original shell model of spherical nuclei has to be modified to encorporate observed collective effects. One way to do this is to use the Nilsson model where single-particle states are generated using a deformed potential. However, the description of the shape-coexistence phenomenon observed in many nuclei [Woo92] near the closed shell is a challenge for both the spherical and deformed shell models. In the next two sections the spherical and deformed shell model approaches for deformed intruder states in even-even nuclei are described.

2.1 The spherical shell-model approach to intruder states

2.1.1 Even-even nuclei

The basic mechanism for creating low-lying 0^+ intruder states near the closed shells can be understood from the scheme shown in Figure 2.1. The orbits filled by protons and neutrons have been marked with j_π and j_ν, respectively. An excited proton configuration of 2p-2h nature is formed by exciting two protons to the orbit j'_π above the shell gap. This kind of 2p-2h excitation is characterised by a large effective number of valence protons. The term valence protons includes both protons and holes. In the Figure 2.1 particles and holes have been marked with filled and open circles, respectively. The solid curve represents the neutron distribution. The low excitation energy of intruder states results from the combined effect of the pairing interactions and the large gain from the residual proton-neutron interaction between the particle-hole configurations and the valence neutrons. The proton-neutron interaction is

strong, especially when the proton orbits j'_π are in the same major shell as the neutron orbits j_ν, which is the case in the nuclei studied in the present work.

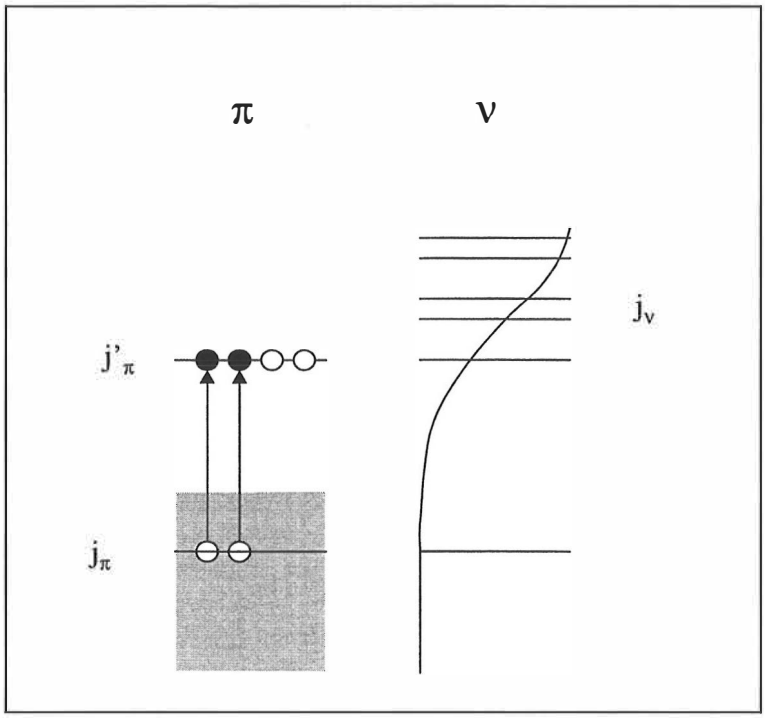

Figure 2.1 Schematic representation of the intruder 2p-2h 0^+ configurations. Particles and holes have been marked with filled and open circles, respectively. The solid line represents the neutron distribution.

In the unperturbed system the energy of the 2p-2h configurations near the closed shells can be written as [Hey87]

$$\Delta = 2(\varepsilon_{j'\pi} - \varepsilon_{j\pi}), \qquad (2.1)$$

where $\varepsilon_{j\pi}$ and $\varepsilon_{j'\pi}$ denote the proton single-particle energies in the two major shells. To get a more realistic expression some modifications have to be done. First, in creation of the 2p-2h configurations particle and hole pairs coupled to $I^\pi=0^+$ are formed and, therefore, the change in the pairing correlation energy has to be taken into account. This binding energy gain due to the pairing can be determined by starting from empirical values of one (S_p) and two-proton (S_{2p}) separation energies.

For a 2p-2h configuration it is given by

$$\Delta E_{pairing} = \Delta E_{pairing}(p) + \Delta E_{pairing}(h) \qquad (2.2)$$

with

$$\Delta E_{pairing}(p) = 2S_p(Z+1,N) - S_{2p}(Z+2,N) \qquad (2.3)$$

$$\Delta E_{pairing}(h) = 2S_p(Z,N) - S_{2p}(Z,N) \qquad (2.4)$$

where (Z,N) denotes the closed-shell proton and neutron number and p and h particles and holes, respectively. These definitions are obtained from the energy of the 0^+ 2p(2h) pair state relative to the unperturbed energy for the 2p(2h) state, which is twice the 1p(1h) single-particle (-hole) energy. The contribution of the pairing energy to the total energy correction is illustrated in Figure 2.2 (straight dashed line).

The proton single-particle energies ($\varepsilon_{j\pi}$, $\varepsilon_{j'\pi}$) are also dependent on the occupation of the valence orbits j_ν by neutrons. The correction due to the occupation of the neutron orbital j_ν can be obtained using

$$\varepsilon\hat{}_{j\pi} = \varepsilon_{j\pi} + \sum_{j_\nu} \langle j_\pi j_\nu \mid V_{\pi\nu} \mid j_\pi j_\nu \rangle v^2_{j\nu} \qquad (2.5)$$

where $V_{\pi\nu}$ represents the proton-neutron residual interaction and $\varepsilon\hat{}_{j\pi}$ and $v_{j\nu}$ are the corrected single-particle energy and the occupation probability, respectively. The proton-neutron monopole binding energy gain ΔE_M when promoting two particles from the j_π orbital to the j'_π orbital can be calculated using

$$\Delta E_M = 2(\varepsilon\hat{}_{j'\pi} - \varepsilon\hat{}_{j\pi}) - 2(\varepsilon_{j'\pi} - \varepsilon_{j\pi}) \qquad (2.6)$$

It is the difference between the radial structures of the j_π and j'_π orbitals that determines whether a 2p-2h configuration will be favoured or not when occupying the valence neutron orbital. In Figure 2.2 this monopole correction (dashed line) is shown in a schematic way for the Z=82 region.

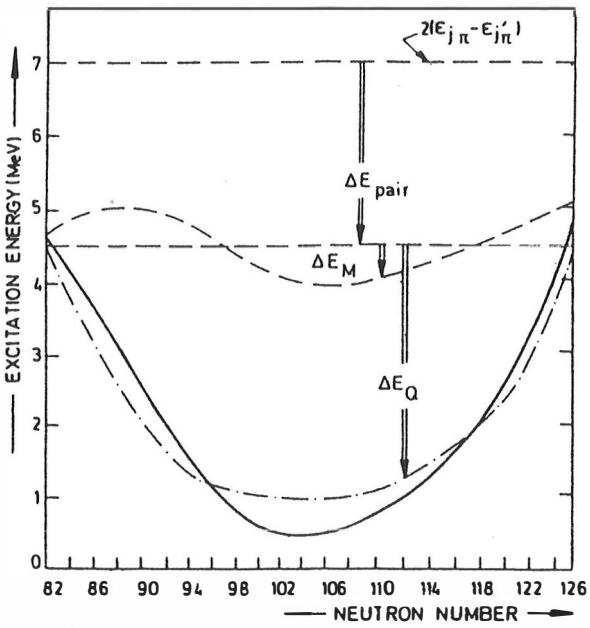

Figure 2.2 The full line represents the total energy corrections for the lowest 0^+ intruder state for the Z=82 region. The different contributions due to the pairing (straight dashed line), the monopole correction (dashed line) and the quadrupole correction (dot-dashed line) are also shown in a schematic way. The upper straight dashed line shows the unperturbed energy. Figure has been taken from reference [Hey87].

Finally, the effect of the binding energy gain due to the proton-neutron quadrupole interaction to the proton single-particle energies has to be considered. The strongly attractive proton-neutron force modifies the 0^+ pair distribution and gives rise to an extra binding energy for the intruder state. The long-range quadrupole part of the proton-neutron interaction is the major term in this interaction and it induces $J^\pi=0^+ \rightarrow J^\pi=2^+$ pair breaking for both the protons and neutrons. This is called a core polarisation effect. The 0^+ ground-state and intruder-state wave functions change to the following form:

$$\left|0_\pi^+ \otimes 0_\nu^+\right\rangle \rightarrow \left|0_\pi^+ \otimes 0_\nu^+\right\rangle + \alpha\left|2_\pi^+ \otimes 2_\nu^+\right\rangle + \ldots. \qquad (2.7)$$

The quadrupole polarisation energy gain ΔE_Q (dot-dashed line in Figure 2.2) can be calculated using, for example, the perturbation theory or the SU(3) model estimate. For more details see reference [Hey87].

Resulting from the discussion above, an expression for the energy of the lowest intruder 0^+ state can be written as:

$$E_{\text{int}}(0^+) = 2(\varepsilon_{j'\pi} - \varepsilon_{j\pi}) - \Delta E_{pairing} + \Delta E_M + \Delta E_Q \qquad (2.8)$$

In Figure 2.2 this total energy correction (solid line) has been plotted in a schematic way as a function of the neutron number for the Z=82 region. It illustrates the combined effect of the pairing ($\Delta E_{pairing}$) and the monopole (ΔE_M) and quadrupole (ΔE_Q) proton-neutron interaction when exciting two protons across the shell gap. Consequently, the low excitation energy of the intruder states is mainly due to the quadrupole component of the proton-neutron interaction. According to this model, the intruder states should minimise their energies near the neutron mid-shell with N=104 [Cos00, Hey89] and, indeed, this has been observed to occur in Hg and Pt nuclei.

Heyde et al. [Hey92, Hey94] introduced the idea that it is the number of bosons (particle pairs outside the closed shell and hole pairs inside the closed shell) which determines the energy level structure of the intruder bands. In this scheme the deformed intruder bands can be classified according to their intruder spin, characterised by $I^{(i)} = N/2$ and $I_z^{(i)} = (N_p - N_h)/2$, where N is the number of proton (neutron) bosons and N_p (N_h) is the number of particle (hole) bosons. According to this classification, intruder spin multiplets are formed of nuclei having similar kinds of level structure.

The prolate intruder structures in Pb and Pt nuclei are assumed to be due to 4p-4h ($I^{(i)} = 2, I_z^{(i)} = 0$) and 2p-6h ($I^{(i)} = 2, I_z^{(i)} = -1$) excitations across the Z=82 shell gap, respectively. This membership in an $I^{(i)} = 2$ multiplet should, according to the intruder multiplet scheme, indicate close similarities of the corresponding bands. In Hg nuclei an intruding prolate band is expected to be based on the 2p-4h ($I^{(i)} = 3/2, I_z^{(i)} = -1/2$) structure and therefore, the band is supposed to have level spacings different from those of Pb and Pt nuclei, but similar to those seen in the ground state bands of Os nuclei (6h; $I^{(i)} = 3/2, I_z^{(i)} = -3/2$).

2.1.2 Odd-mass nuclei

In the odd-mass nuclei near the closed shells the 1p-2h or 2p-1h excitations form the origin of the intruder states whereas in even-even nuclei 2p-2h excitations give rise to the lowest 0^+ intruder states. Thus, for odd-mass nuclei the energy of the lowest intruder state can be calculated in a similar way as for even-even nuclei i.e. by taking into account the pairing energy correction ($\Delta E_{pairing}(odd)$) and the corrections due to the monopole ($\Delta E_M(odd)$) and quadrupole ($\Delta E_Q(odd)$) proton-neutron interactions. An expression for the energy of the lowest intruder state ($E_{int}(j_\pi)$) in odd-mass nuclei can be written as [Hey88]:

$$E_{\text{int}}(j_\pi) = (\varepsilon_{j'\pi} - \varepsilon_{j\pi}) - \Delta E_{pairing}(odd) + \Delta E_M(odd) + \Delta E_Q(odd) \qquad (2.9)$$
$$\approx \frac{1}{2} E_{\text{int}}(0^+; even)$$

The energy of a 1p-2h intruder state is very near to half of the excitation energy of the corresponding 2p-2h 0^+ intruder state in even-even nuclei.

2.2 The deformed shell-model approach to intruder states

Models for calculating the single-particle energies for protons and neutrons in a deformed potential have been developed for example by Mottelson [Mot55] and Nilsson [Nil55]. The Nilsson model is discussed here in more details. The Nilsson model is introduced for axially symmetric deformed nuclei and it was originally based on a modified harmonic oscillator potential. Another potential commonly used for nuclei far from stability is the deformed Woods-Saxon potential. When using the deformed potential the angular momentum j of a single nucleon is no longer a good quantum number. The conserved quantum numbers are the parity (π) and the projection of the total angular momentum on the symmetry axis (Ω). The single-particle levels are labelled with a set of asymptotic quantum numbers. These Nilsson quantum numbers are written in a form of $\Omega^\pi[Nn_z\Lambda]$, where N is the principal oscillator quantum number, n_z is the number of nodes along the symmetry axis and Λ is the projection of the angular momentum l on the symmetry axis. In addition, Λ=

$\Omega+\Sigma=\Omega\pm1/2$, where Σ is the projection of the intrinsic spin along the symmetry axis. There is also a relation between the permissible values of n_z and Λ such that their sum must be even (odd) if N is even (odd). Instead of the $2j+1$ degeneracy each $\Omega^{\pi}[Nn_z\Lambda]$ state is two-fold degenerate corresponding to particles with $\pm\Omega$. The low-Ω orbits have a large spatial overlap with a prolate ($\beta_2>0$) deformed core and they are consequently lowered in energy when going towards prolate deformation. Likewise the high-Ω orbits overlap with the oblate core and are lowered in energy with increasing oblate ($\beta_2<0$) deformation. With $\beta_2=0$ the spherical shell-model levels are obtained. In the Z=82 region the steeply down-sloping $\pi h_{9/2}9/2^-[505]$, $\pi h_{9/2}1/2^-[541]$, $\pi h_{9/2}3/2^-[532]$, $\pi i_{13/2}1/2^+[660]$, $\pi f_{7/2}1/2^-[530]$ orbitals and up-sloping $\pi s_{1/2}1/2^+[400]$, $\pi d_{3/2}3/2^+[402]$, $\pi h_{11/2}11/2^-[505]$ orbitals play an important role when explaining the shape-coexistence phenomenon. For both the prolate and oblate shapes the energy needed to excite quasi-particles across the shell gap is lowered dramatically compared to the spherical situation. This is visualised in Figure 2.3 where a deformed single-proton level diagram (Nilsson diagram) around $Z=82$ is shown ($\varepsilon_2 \sim 0.95\beta_2$).

The possibility of the shape coexistence in the neutron-deficient Pb, Pt and Po isotopes was anticipated theoretically using the deformed shell-model approach by May, Pashkevich and Frauendorf in 1977 [May77]. Later calculations using the Woods-Saxon deformed potential and a pairing force for the residual particle-particle interaction have been done by Nazarawicz [Naz93] and Bengtsson et al. [Ben87, Ben89] for the nuclei in the Pt-Pb region. In Figure 2.4 a) and b) excitation energies of various shape-coexisting configurations (0^+ band-head energies) in the even-even Hg isotopes with $86\leq N\leq120$ and Pb isotopes with $96\leq N\leq120$ are shown, respectively. For neutron-deficient isotopes with $N<110$ these calculations predict a competition between low-lying prolate and oblate shapes. In their ground states Hg isotopes with $N\geq96$ are predicted to have a deformed oblate shape, while the lighter isotopes should be spherical. The Pb isotopes are typically spherical in their ground states. Oblate states (dots) involving a two-proton excitation to the $9/2^-[505]$ ($1h_{9/2}$) orbital are predicted to occur in Pb isotopes with $N\leq118$.

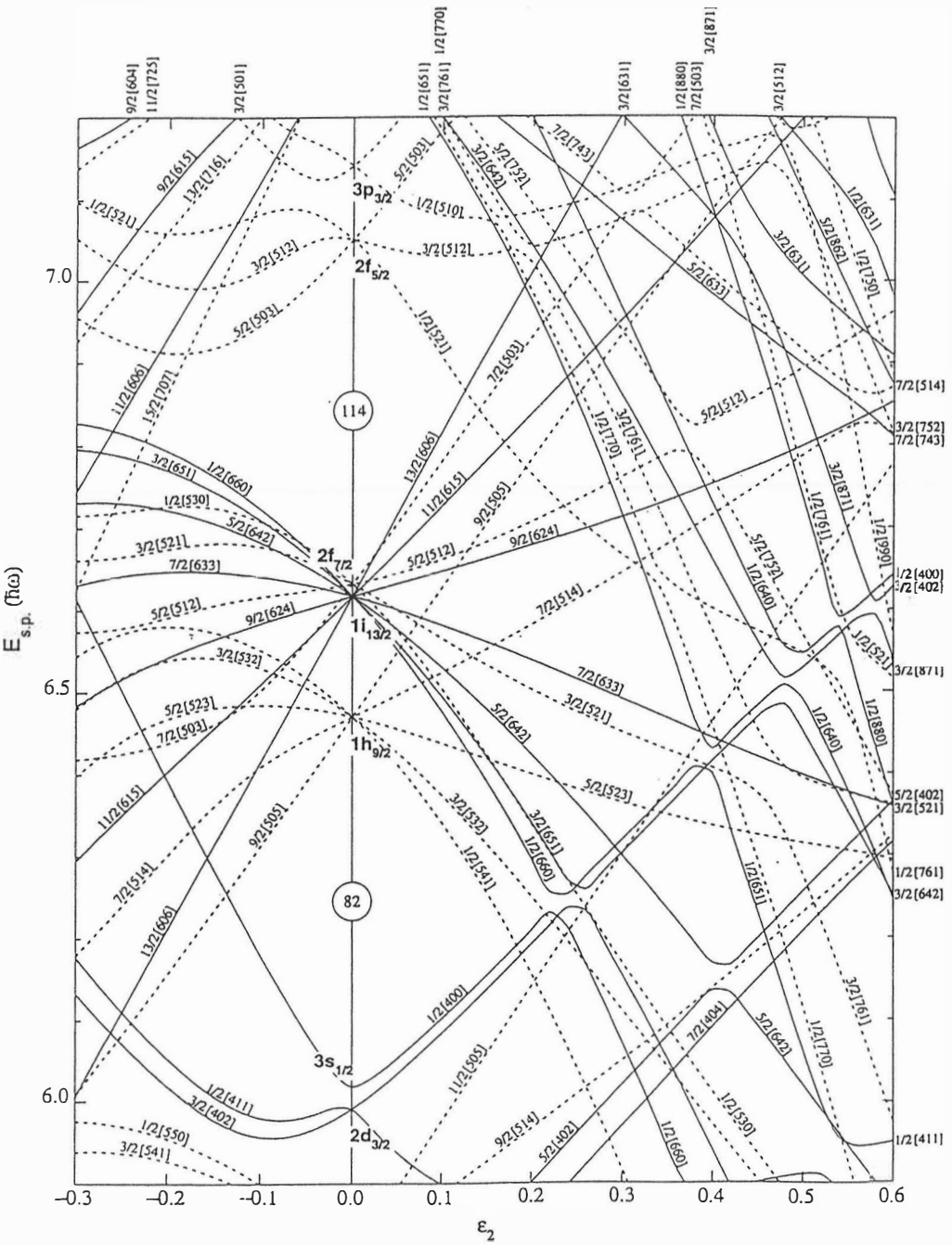

Figure 2.3 Deformed single-proton level diagram around Z=82 ($\varepsilon_2 \sim 0.95\beta_2$). The diagram has been taken from reference [Fir96].

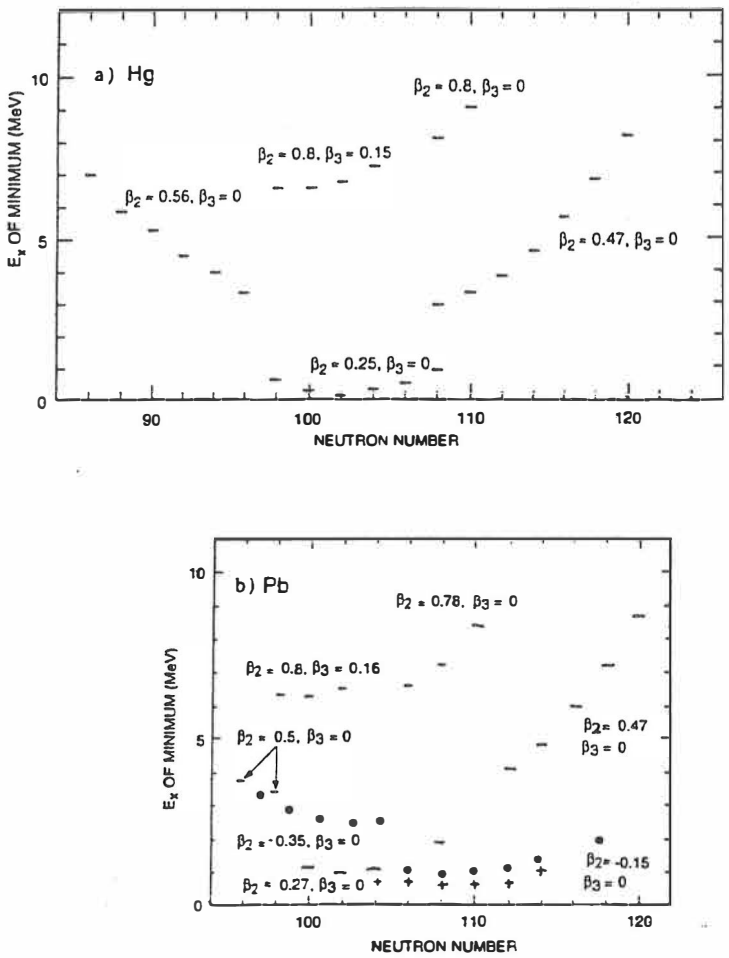

Figure 2.4 Excitation energies of various shape-coexisting configurations in the even-even a) Hg isotopes with $86 \leq N \leq 120$, b) Pb isotopes with $96 \leq N \leq 120$. The prolate (oblate) states are indicated by dashes (dots). The crosses show the experimental energies of deformed 0^+ states. Picture has been taken from reference [Naz93].

Well-deformed prolate states (dashes) are predicted to appear in both the Pb and Hg nuclei with $N \leq 110$. This large quadrupole deformation is caused by the occupation of strongly prolate-driving low-Ω $1h_{9/2}$ and $2f_{7/2}$ states and emptying the oblate driving $1h_{11/2}$ orbits [Naz93]. In Pb nuclei the prolate shape is assumed to be due to the four-proton excitation to the orbits above the shell gap. One reason why four-proton

excitation in Pb nuclei leads a prolate shape can be understood with reference to Figure 2.3. The orbital density on the prolate side of the diagram with $\varepsilon_2 \sim 0.25$ is higher than that of the oblate side with $\varepsilon_2 \sim -0.15$. Therefore less energy is needed to excite four protons when having the prolate shape instead of the oblate one.

The deformed shell-model approach has also been used to explain the shape coexistence phenomenon in odd-mass nuclei. For example, in odd-mass Tl isotopes the low-lying $9/2^-$ isomeric states have suggested to be due to the odd proton occupying the oblate-driving $9/2^-[505]$ orbit [New70].

2.3 Comparison of the spherical and deformed shell-model approaches to intruder states

If a comparison is made between the two models of the intruder states described above some common features can be seen. The excitations, which are called intruder 2p-2h excitations in Section 2.1 correspond to the deformed configurations having a quadrupole equilibrium different from the ground state value described in Section 2.2. The approach starting from a deformed single-particle mean field including residual pairing interaction gives the same results as the approach starting from a spherical shell model including the proton-neutron interaction. This is visualized in Figure 2.5 where the total excitation energy for the lowest 0^+ intruder state of Pb isotopes calculated starting both from the Nilsson model and from the spherical shell model is shown. In the same picture the experimentally observed excited 0^+ states are plotted. Both models succeed rather well in reproducing the 0^+ levels of Pb isotopes.

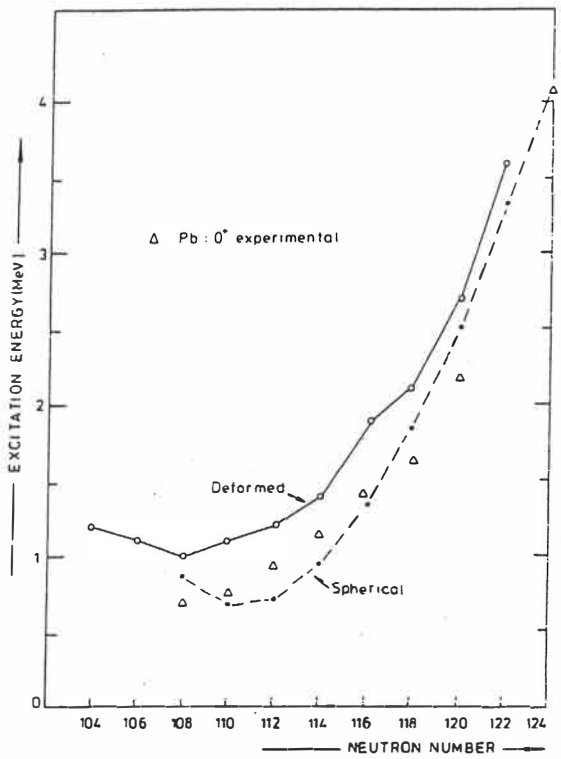

Figure 2.5 The total excitation energy for the lowest 0^+ intruder state of Pb isotopes calculated starting both from the Nilsson model and from the spherical shell model. The experimentally observed 0^+ states are marked with open triangles. Figure has been taken from reference [Hey89].

3. Experimental methods

Due to the lack of suitable beam and target combinations, the only way to produce very neutron-deficient Hg, Tl and Pb nuclei for the in-beam spectroscopic studies is to use heavy-ion induced fusion-evaporation reactions. However, the production cross sections for the nuclei of interest in this work are very small and, therefore, a special technique was needed to separate these nuclei from the dominant fission products and the residues from the stronger evaporation channels as well as from the beam particles and transfer products. In this chapter the experimental set-up and data analysis methods will be presented. In the first part, general properties of the heavy-ion induced fusion-evaporation reactions are discussed. The gas-filled separator RITU and the Ge-detector arrays used in the present work are described next. The end of the chapter describes a short introduction to the data analysis when utilising the recoil-decay-tagging (RDT) method.

3.1 Heavy-ion induced fusion-evaporation reactions

In the present work the nuclei of interest were produced via heavy-ion induced fusion-evaporation reactions. This production method proved to be ideal for the RDT technique. Firstly, the angular acceptance of RITU is rather small (10 msr [Lei95b]) and, thus, the RDT method can be utilised efficiently only if the angular distribution of recoils flying out of the target is strongly forward peaking. Secondly, when the recoiling products fly towards forward angles the γ-ray detection angle with respect to the recoil can be determined easily and, therefore, the Doppler corrected γ-ray transition energies can be obtained. In the reactions used in the present work over 90% of the total cross section went into the fission channels. The remaining small fusion-evaporation cross section was fragmented into many channels and, therefore, it was essential to separate the channel of interest not only from the primary heavy-ion beam and fission products but also from the other, usually stronger evaporation channels. For example, in the ^{176}Hg measurement the 2p2n evaporation channel leading to ^{176}Pt was the strongest one, being over 100 times stronger than the 4n-channel producing the nucleus of interest. The production cross-section for the 4n

channel was approximately 5 μb. In practice, using a typical beam intensity of 15 pnA and target thickness of 500 $\mu g/cm^2$ approximately 3000 ^{176}Hg nuclei were produced per hour. About 650 γ-rays originating from the ^{176}Hg nuclei were detected per hour. This was a very small fraction of the total Ge-detector counting rate of 7×10^9 events/hour.

In a fusion-evaporation reaction a target nucleus and a projectile fuse together forming a compound nucleus. In this process the kinetic energy of the projectile is partly converted into excitation energy of the compound system. After the collision thermodynamic equilibrium occurs within about 10^{-20} seconds, after which the compound system decays by either high-energy γ-ray emission (such as giant resonance decay) or by nucleon evaporation, where neutrons, protons and α-particles are emitted. The particle evaporation continues until the system reaches a state where the excitation energy is less than the particle separation energy. The remaining excitation energy and angular momentum are dissipated by a series of electromagnetic transitions.

Essential to the compound-nucleus model is the assumption that the relative probability for decay into any specific set of final products is independent of the means of formation of the compound nucleus. However, this is not exactly true. The decay probability depends both on the total energy and the total angular momentum given to the system. Target and projectile combinations, which lead to the same compound nucleus at the same excitation energy, have different probabilities to produce a compound nucleus with certain angular momentum. In general, when using a heavy projectile more angular momentum is brought into the compound system and high-spin states near the yrast line are populated, while with lighter projectiles low-spin states further away from the yrast line can be populated in the residual nuclei.

The type of the open reaction channels can also change depending on the neutron number. Due to the Coulomb barrier charge-particle emission is inhibited compared to neutron evaporation for a compound system relatively close to the valley of stability. When moving towards the neutron-deficient side the neutron separation energy increases and the proton separation energy decreases allowing charged particle

emission to compete and often even dominate over neutron evaporation. In the present work very neutron-deficient nuclei were studied and, indeed, the strongest fusion-evaporation channels were 2pxn channels.

The Coulomb repulsion between the target nucleus and the projectile determines the minimum energy needed to form the compound nucleus. This repulsion is characterised by the Coulomb barrier:

$$B_C = \frac{e^2}{4\pi\varepsilon_0}\frac{Z_p Z_t}{r} \qquad (3.1)$$

where Z_p and Z_t are the atomic numbers of the projectile and target nuclei, respectively and r is the interaction radius defined as $r = R_0(A_p^{1/3} + A_t^{1/3})$, $R_0 =$ 1.45fm [Lei77].

The excitation energy (E_{ex}) of the compound nucleus is related to the centre of mass kinetic energy (E_{cm}) of the collision and the Q-value of the reaction:

$$E_{ex} = E_{cm} + Q \qquad (3.2)$$

Q is the difference between initial and final masses of the nuclei involved.

In the reactions used in the present work evaporation of one neutron reduced the excitation energy of the compound nucleus on the average by an amount of approximately 13 MeV, where 11 MeV went to the binding energy and 2 MeV to the kinetic energy of the neutron.

3.2. Gas-filled separators

3.2.1 General properties

A gas-filled separator provides an effective tool to separate fusion-evaporation products from the unwanted background of fission fragments, projectiles and target-like products. The separation method is based on the use of a dipole magnet with the field region filled with a dilute gas such as helium. This separation technique was first applied by Cohen and Fulmer [Coh58] for the separation of fission fragments. The

technique was developed some years later by Armbuster et al. [Arm71]. For the study of residues from fusion-evaporation reactions a gas-filled separator was used at Dubna by Karnaukhov et al. [Kar69] and at Berkeley by Ghiorso et al. [Ghi88]. Besides RITU, the gas-filled separators in operation nowadays are the JINR-Dubna separator [Laz93], the GARIS separator in Osaka [Miy87] and the Berkeley gas-filled separator BGS [Nin99].

In heavy-ion induced reactions slow recoils have broad velocity and ionic charge distributions. The use of the filling gas is essential when trying to collect all charge states of the fusion evaporation residues to the detector at the focal plane. From the Lorentz force, the radius (ρ) of the trajectory of a particle in a homogeneous magnetic field (B), where $\overline{B} \perp \overline{v}$, is determined by

$$\rho = \frac{mv}{Bq} \qquad (3.3)$$

where m, v and q are the mass, velocity and charge of the ion, respectively. From (3.3) it can be seen that the broad ionic charge distribution leads to a wide spatial distribution of the recoils at the focal plane of the separator, which is difficult to cover with a realistic detector. However, in gas the recoils undergo atomic charge-changing collisions. The recoils follow approximately an average trajectory corresponding to their momenta and the average charge state ($\overline{q}$) when traversing through the dipole magnet filled with gas of low pressure. The average charge-state is independent of the initial distribution of charge states. It depends only on the mass (A) and atomic number (Z) of the recoils. Figure 3.1 shows a schematic view of the tracks of the ions both in vacuum and in gas. Derived from the Thomas-Fermi model of the atom the average charge-state can be expressed by:

$$\overline{q} = \frac{v}{v_0} Z^{1/3} \qquad (3.4)$$

for a velocity range $1 < v/v_0 < Z^{2/3}$[Boh41]. The v_o = 2.19 × 10^6 m/s is the Bohr velocity. The equation (3.3) can now be rewritten as:

$$B\rho = 0.0227 \times \frac{A}{Z^{1/3}} [Tm] \qquad (3.5)$$

where the term $B\rho$ is the magnetic rigidity of the ion and A and Z are the atomic mass number and the proton number of the ion, respectively [Ghi88].

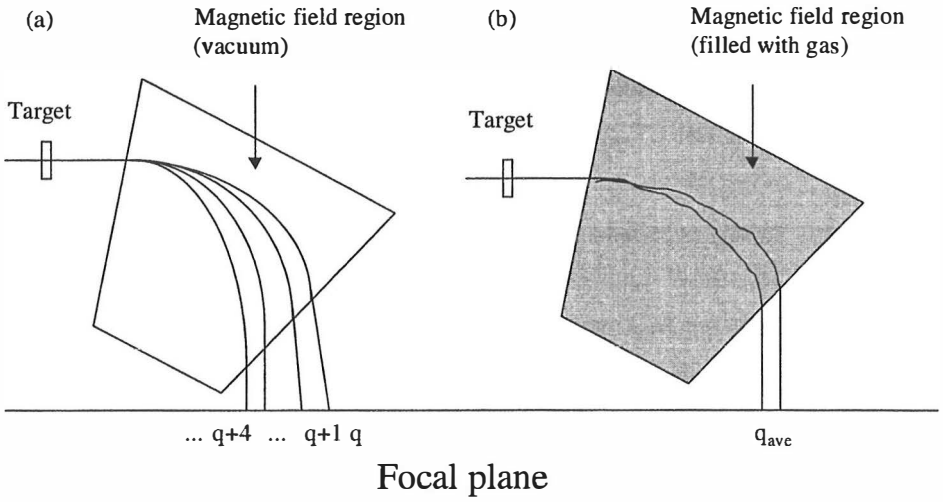

Figure 3.1 A schematic view of the trajectories of the ions both in vacuum (a) and in gas (b).

Due to the narrower spatial distribution of the recoils the recoil detection efficiency is higher when using a gas-filled separator than when using a separator operating in vacuum mode. Consequently, the transmission of a gas-filled separator is typically higher than that of a vacuum-mode separator. In the heavy-ion induced fusion reactions used in this work the transmission was around 20% - 30%. However, the high transmission is achieved at the expense of the Bρ-resolution of the separator. The Bρ-resolution of a gas-filled separator is low, typically of the order of 10% [Lei95b]. The Bρ-resolution depends on the pressure of the filling gas as illustrated in Figure 3.2 where the typical behaviour of the Bρ-resolution as a function of the pressure of the filling gas is shown. Finding the optimum pressure is a question of finding a balance between charge state focusing and multiple scattering phenomena. In practice, the gas-filled separator used in the present work cannot separate different fusion-evaporation channels. In the present study the identification of an evaporation residue was based on the detection of subsequent characteristic α-decay.

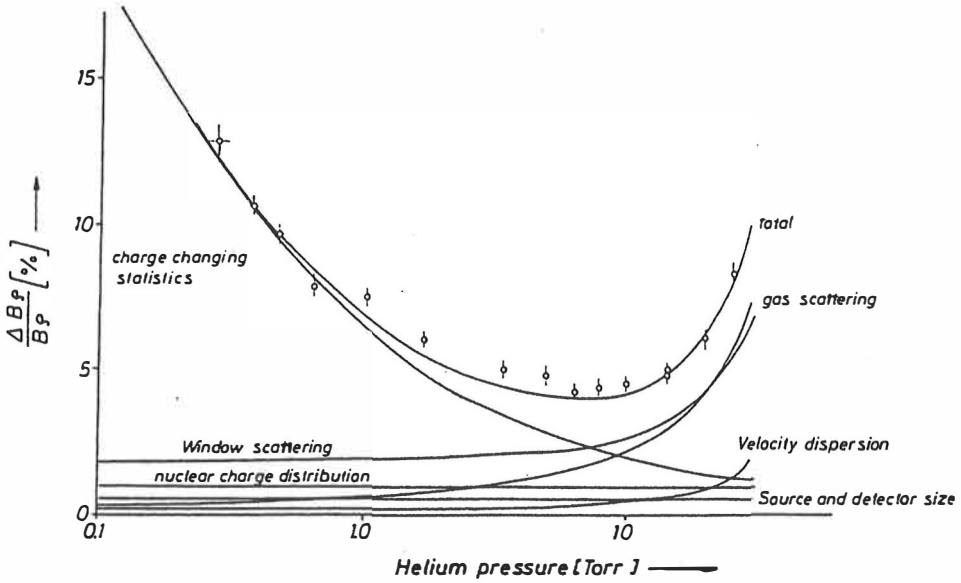

Figure 3.2 The typical behaviour of the Bρ-resolution as a function of the pressure of the filling gas in gas-filled separators. Figure taken from reference [Arm71]

3.2.2 The gas-filled separator RITU

The ion optical configuration of the gas-filled recoil separator RITU (Recoil Ion Transport Unit) is QDQQ, where Q stands for a focusing quadrupole magnet and D for a separating dipole magnet. RITU differs from most of the gas-filled separators, which have been designed so that separation of the primary beam takes place immediately after the target (DQQ-configuration). In RITU, a small, strong vertically focusing quadrupole has been added in front of the dipole to achieve better matching to the dipole magnet acceptance. The scheme of RITU in conjunction with a Ge-detector array is shown in Figure 3.5. Normally a helium gas pressure of 0.5 – 3 mbar is used. Continuous gas flow is used to remove gaseous impurities from the separator field region. The high vacuum of the cyclotron beam line is separated from the gas-filled chamber by a carbon or nickel foil. Typical thickness of these foils is from 50 to 500 $\mu g/cm^2$. In in-beam measurements the thickness of the foil should be minimised in order to reduce the background radiation near the backward Ge-detectors. In this work a 50 $\mu g/cm^2$ carbon foil was used.

At the focal plane of RITU there is a PIPS (Passivated Implanted Planar Silicon) detector to detect recoils and their subsequent α-decays. The thickness of the detector is 300 μm and the effective size is 80mm (horizontal) × 35mm (vertical). The detector consists of 16 separate strips of 5 mm width, each position-sensitive in the vertical direction. Position sensitivity is achieved through the use of a resistive layer. The measured position resolution is better than 500 μm for each strip. In practice, the effective number of pixels is less than the number obtained by taking into account the number of strips and the position resolution. The reason is that the recoils are not evenly distributed over the surface of the detector. Especially in the vertical direction the counting rate is much higher in the centre of the detector than at the edges of the detector. In the horizontal direction the Si detector covers approximately 70% of the recoil distribution at the focal plane. The effective number of pixels can be determined from the ratio of the rate of the recoil candidates implanted into the detector to the rate of the random correlations. Typically this number is about 200. The energy signal from the event in the Si detector is obtained by summing the signals from the top and bottom ends of the detector. To process signals from the preamplifiers two different amplification channels are used. One channel is suitable for low-energy (decay) events and the other for high-energy (recoil) events.

In the first part of the Jurosphere II experiments 110 mm up-stream from the Si detector a multiwire proportional avalanche counter (MWPAC) was installed to separate recoil-like events from the decay-like events and thereby to clean the alpha spectrum. The pressure of the isobutane gas used in the counter was about 3 mbar. The total thickness (isobutane thickness) of the detector was 20 mm but the thickness where the charge collection took place was only 6 mm. The isobutane was isolated from RITU's helium volume and the silicon detector chamber vacuum with two 100 $\mu g/cm^2$ Mylar foils. Intrinsic detection efficiency of this 110mm (horizontal) × 64mm (vertical) detector for recoils and beam particles is better than 99%. In Figure 3.3 it can be seen that when demanding that the avalanche counter signal is not present (decay-like event) the background caused by scattered beam particles and recoils can be reduced significantly. Later in the Jurosphere II measurements the gas counter was placed about 90 mm closer to the Si strip detector to detect escaping α particles. This is essential especially when studying proton emitters because typical energies of the

backwards escaping α particles fall in the same region as proton decay energies i.e. 1-2 MeV. In this set-up it was also possible to place degrader foils between the gas counter and the Si strip detector to choose a suitable recoil energy range and to stop low-energy beam-like particles. In addition, two quadrant Si detectors were installed 3-4 mm behind the Si strip detector to detect very energetic protons and α particles flying through the Si strip detector. The background caused by these punch-through particles can be reduced significantly when demanding that the signal from the quadrant is not present.

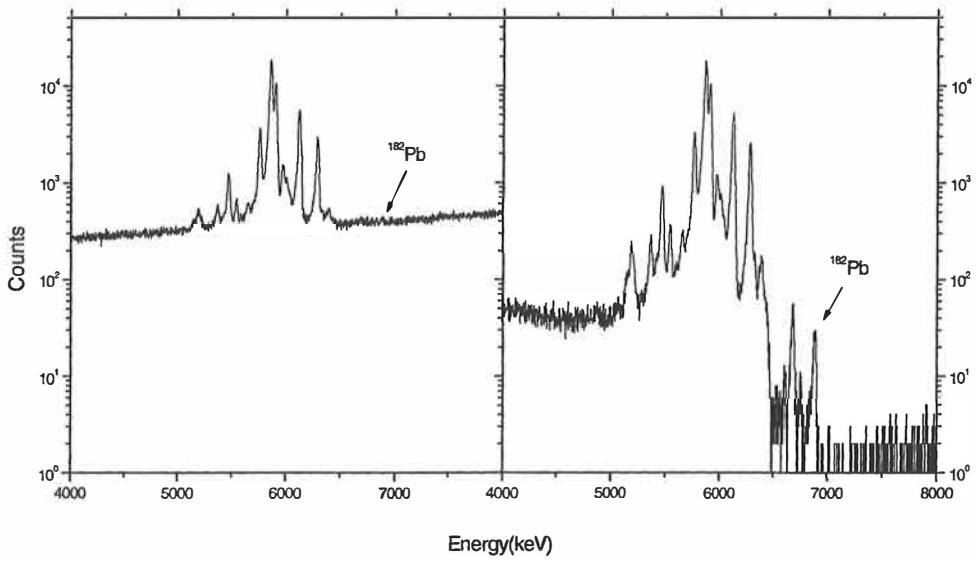

Figure 3.3 a) A singles α-particle energy spectrum from the reaction $^{42}Ca + ^{144}Sm \rightarrow ^{186}Pb^*$, b) the same spectrum when demanding that the avalanche counter signal is not present.

3.3 Gamma-ray detector arrays

3.3.1 Compton-suppressed Ge detectors

In the present work TESSA-type [Nol85] and Eurogam Phase I [Bea92] and Nordball-type [Mos89] high purity Ge semiconductor detectors with escape suppression shields, shown in Figure 3.4, were used in γ-ray detection. A closed end coaxial n-type Ge crystal is the main component of all of these detectors. In γ-ray spectroscopy the n-type Ge detectors are preferred over the p-type detectors because of their better

resistance to the radiation damage induced by the fast neutrons. The neutron-damaged n-type Ge detectors can also be annealed in the home laboratory at JYFL. In Table 3.1 crystal dimensions, photo-peak efficiencies, measured energy resolutions and peak-to-total (P/T) values with the anti-Compton shields are listed. The photo-peak efficiencies are given for 1.33 MeV γ-rays relative to a 76mm × 76mm NaI(Tl) scintillation detector, which has an absolute efficiency of 1.2×10^{-3} at a distance of 25 cm from the source.

Table 3.1. Comparison of properties of different high purity Ge detectors used in the present work.

Detector type	Diameter of the crystal [mm]	Length of the crystal [mm]	Photo-peak efficiency [%]	Measured energy resolution at 1.3 MeV [keV]	Measured peak-to-total at 1.3 MeV [%]
TESSA	52	57	20-25	2.0 – 2.5	40-45
Eurogam	69-75	≥ 70	65-85	2.4 – 3.0	40-50
Nordball	≤56	≤75	25-40	2.2 – 2.7	45-55

The efficiencies of the detectors and the shapes of the escape suppression shields used to reduce the background caused by the Compton scattering differ from each other, but the structure in general is the same in all of them. An anti-Compton shield surrounding the Ge crystal consists of several optically separated bismuth germanate (BGO) crystals each of them viewed by a photomultiplier tube. In TESSA-type BGO shields a detector made of NaI(Tl) is installed at the front part of the shield to catch the low energy γ-rays backscattered from the Ge crystal. The NaI(Tl) material is used because of the light output ten times higher than that of BGO. Heavy metal or lead collimators shaped for each shield geometry were installed in the front of the BGO shield to prevent γ-rays from the target directly hitting the shield crystal.

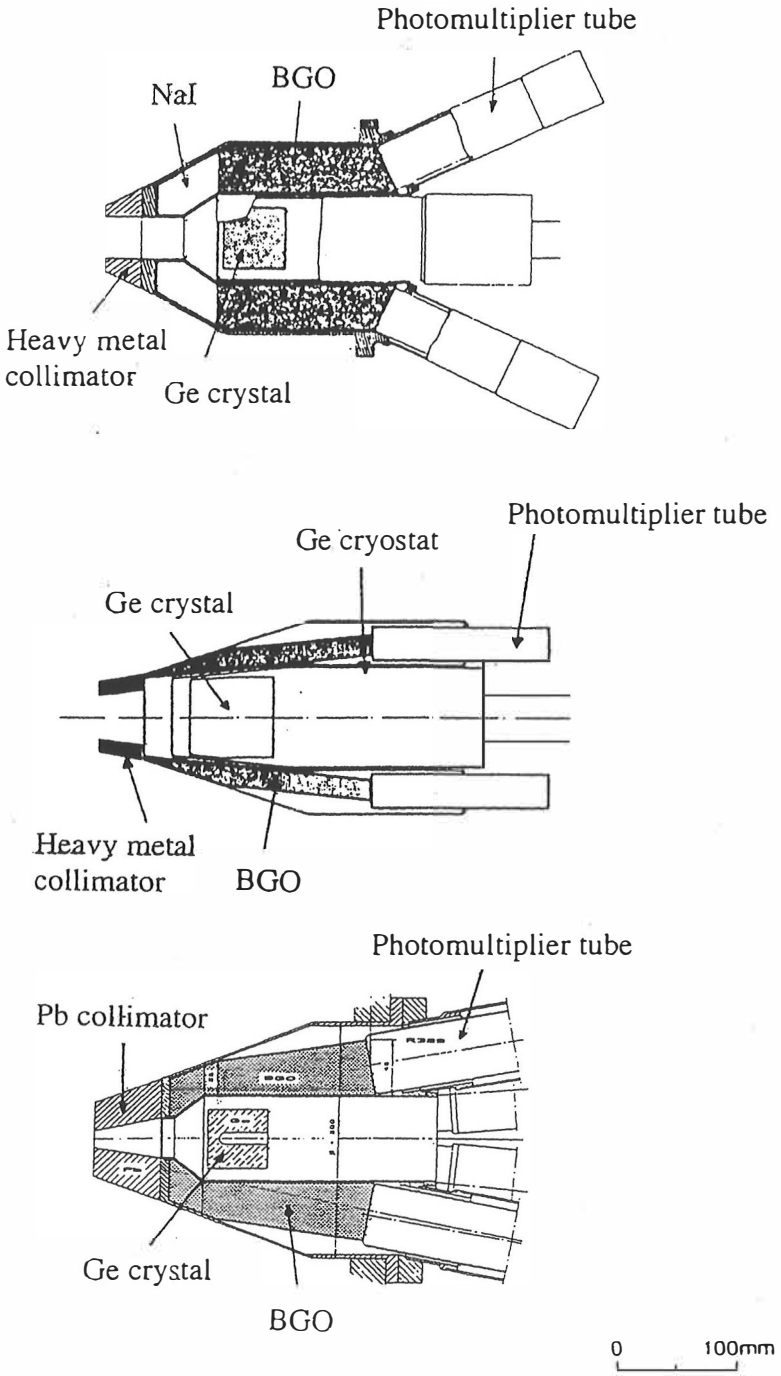

Figure 3.4 a) TESSA-type [Twi83], b) Eurogam Phase I [Bea92] and c) Nordball-type [Mos89] Ge detectors with an escape suppression shield.

3.3.2 Jurosphere arrays

The Jurosphere array (Figure 3.5) consisted of 15 Eurogam Phase I and 10 TESSA-type Compton-suppressed Ge detectors placed at the distances of 20.5 cm and 22 cm from the target, respectively. The Jurosphere II array could accommodate 15 Eurogam Phase I, 7 TESSA-type and 5 Nordball-type detectors, each with an escape suppression shield. The Eurogam Phase I detectors were placed at the same distance as in the Jurosphere array, but the Nordball detectors and five of the TESSA detectors were positioned closer, at the distance of about 20 cm from the target. The two remaining TESSA detectors were at the distance of 22 cm. In both set-ups the Eurogam Phase I detectors were mounted into a section of a Eurogam frame, ten at 134° and five at 158° relative to the beam direction. The TESSA and Nordball detectors were in three rings of angles 63°, 79° and 101°. In the measurements discussed in this work copper (0.5 mm) and tin (0.25 mm) absorbers were used to reduce the counting rate due to the low-energy X-rays.

In the first part of the Jurosphere II experiments there was also an array of five Compton-suppressed Ge detectors (three Nordball detectors and two TESSA detectors) placed around the Si detectors at the focal plane. In the later Jurosphere II experiments only one Compton-suppressed Nordball detector was used at the focal plane.

The measured absolute photo-peak efficiencies of the Jurosphere and Jurosphere II arrays for 1.33 MeV γ-rays were about 1.5% and 1.7%, respectively. For Jurosphere II the efficiency calculated from the given photo-peak efficiencies of the detectors listed in Table 3.1 was about 2.4%. Due to dead time, Compton suppression and use of the collimators the measured efficiencies tend to be lower than that calculated ones. In this case, tested with one TESSA detector, the efficiency measured using a collimated shield was found to be about 30% lower than that measured without the shield.

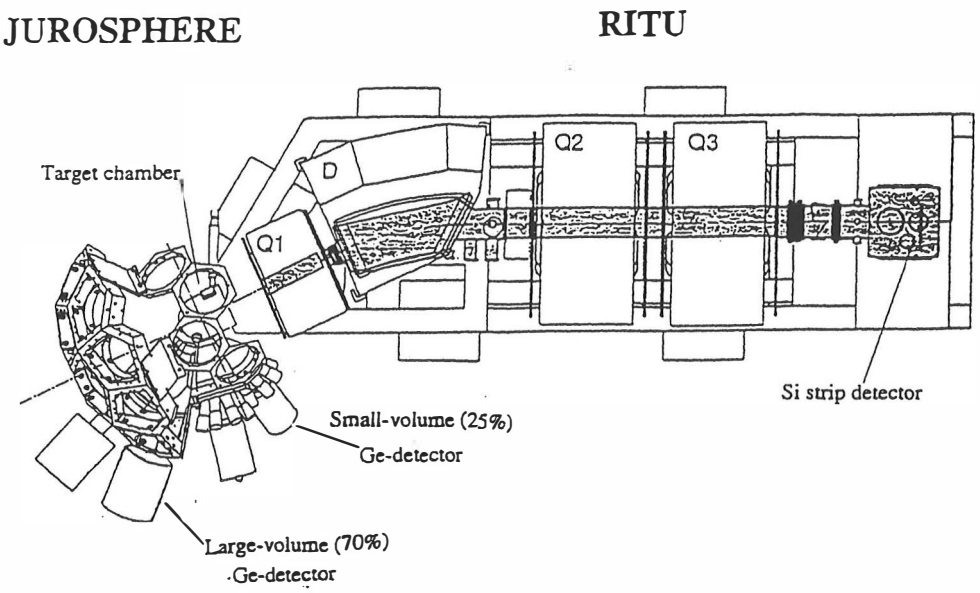

Figure 3.5 Jurosphere Ge detector array in conjunction with the gas-filled recoil separator RITU.

3.4 Electronics

In Figure 3.6 the block diagram of the pulse shaping and digitisation electronics used in the Jurosphere II set-up is shown. In case of the Jurosphere a similar scheme of electronics was used.

3.4.1 Ge detectors

The signals from the detectors were processed using NIM electronics. Linear spectroscopy amplifiers (AMP) were used to amplify the energy signals from the Ge detector preamplifiers. Following this the amplification signals were digitised in analogue-to-digital converters (ADC) before being fed into the data acquisition system. In order to produce the timing information, fast timing filter amplifiers (TFA) were used to amplify and properly shape the preamplifier signals. When using the TFA the rise time information of the preamplifier signal is maintained. The analogue timing signal from the TFA was fed to a constant fraction discriminator (CFD) to obtain a logic timing signal for the coincidence unit (COIN). The TFA and CFD units were tuned to achieve the best possible amplitude and rise-time compensation. The COIN unit was used to reject the γ-rays scattered from the Ge detector to the BGO shield. This was performed by demanding an anti-coincidence between the signals

from the Ge detector and the corresponding BGO shield CFD. The same COIN unit was also used for pile-up rejection. If two γ-rays hit the detector within a too short time interval compared to the signal processing time of the spectroscopy amplifier the amplifier signals pile-up to form an output pulse of distorted shape. In the present set-up the piled-up pulses were rejected by using their timing signals: The latter γ-event was rejected in the first COIN unit (a) in Figure 3.6 using the busy signal (w ~ 20 μs) from the linear amplifier. The fact that the zero crossing point of the piled-up bipolar signal is delayed was utilised to reject the first of the pile-up events in the second COIN unit (b) in Figure 3.6. The zero crossing point was determined using a timing cross-over unit (TCO). The signals which were not rejected neither in the Compton suppression nor in the pile-up rejection were stretched and delayed in a gate and delay generator (GDG) in order to form an individual ADC gate for each Ge detector. A multiplicity logic unit (MLU) was used to obtain γγ-coincidence information. The overlap coincidence time was 300 ns.

To record the γ-rays time information both individual time-to-digital converters (TDC) and common time-to-amplitude converters (TAC) were used. In a TDC the common start signal was the cyclotron radio frequency (RF) signal in coincidence with the γ-recoil event and the individual stop was a Ge detector timing signal. In Jurosphere II set-up an additional condition was set so that no energy information from the Ge detectors was recorded if the TDC signal was not present, thus removing prompt accidental γ-rays. In this set-up there were in fact two TDC spectra for each Ge detector: one described above with a time scale of 1 μs and the other with a longer range of 32 μs to record the time information for the delayed γ-ray events. In the latter TDC the common start signal was a recoil event and the stop was a signal from an individual Ge detector. In both Jurosphere set-ups a common time spectrum for the arrays both in the target area and at the focal plane were generated. A γγ-coincidence event was used to start a TAC and any Ge detector signal to stop the TAC in both cases. There was also one TAC unit to record the time information between a recoil and any prompt γ-ray and one to record the time information between a recoil and any delayed γ-ray observed at the focal plane. In the Jurosphere II set-up one TAC unit was also added to record a time difference between the avalanche counter signal and any prompt γ-ray.

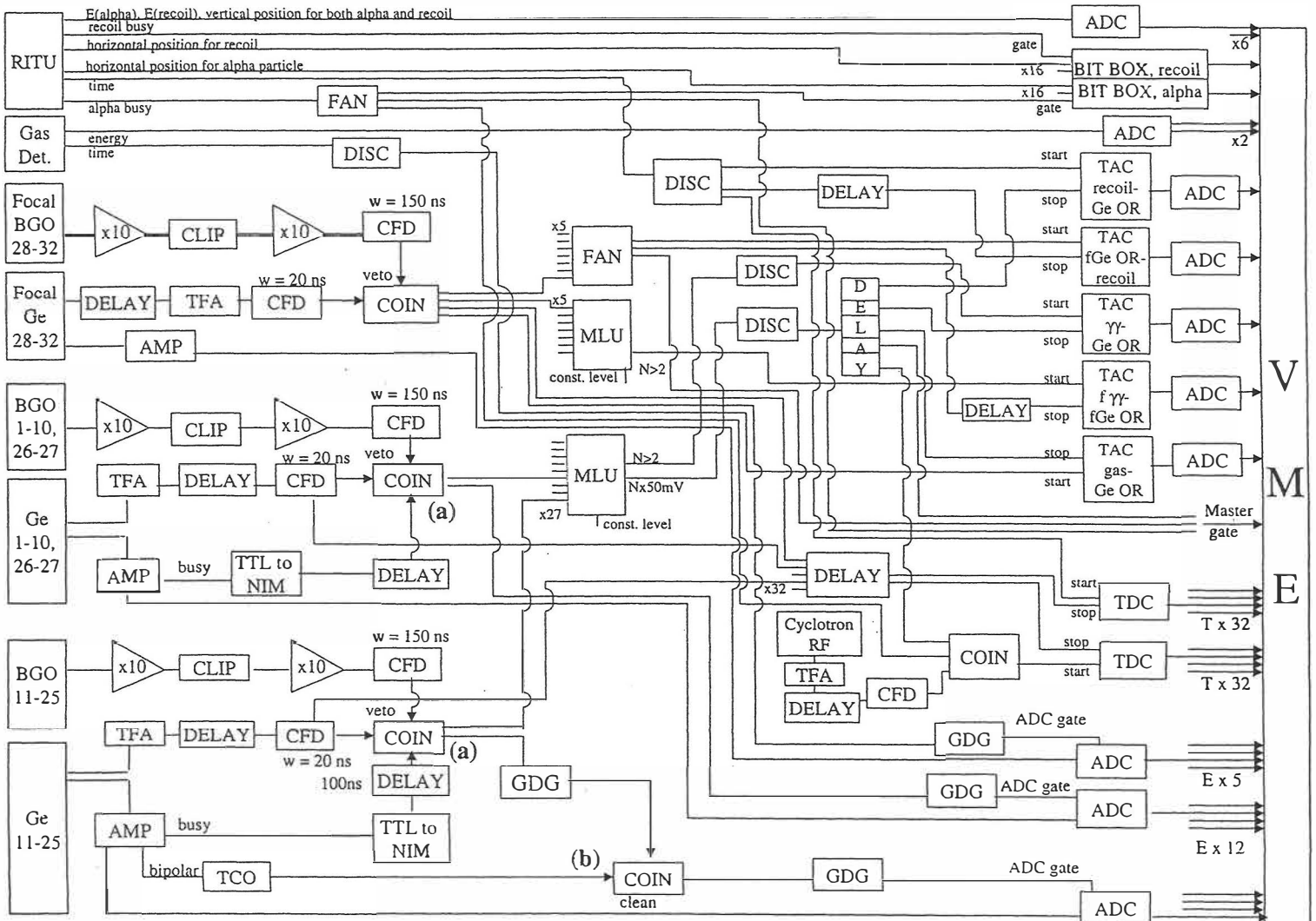

Figure 3.6 A block diagram of the data collecting electronics used in Jurosphere II set-up.

3.4.2 RITU Si detector and avalanche counter

Both ends of the strips of the focal plane Si detector were connected to charge-sensitive preamplifiers. One of the preamplifier outputs was a fast timing signal and the other was used to determine the energy of detected events. The total energy of the signal was obtained by summing the signals from both ends. Due to the resistive layer the division of the signal to the top and bottom parts was proportional to the vertical position of the event. Thus, the ratio of the signal from one end of the detector to the total energy signal was used to determine the vertical position where the event occurred. Two different amplification channels were used to process the signals from the preamplifiers: one for the decay products and one for the recoils. In total each strip had six amplifying channels: three channels for the decay-like events (top position, bottom position and sum energy) and three channels for the recoils (top position, bottom position and sum energy). The top, bottom and sum energy outputs were fed into multiplexers to reduce the quantity of the ADCs needed to process the signals. A triggering pulse for each channel of the multiplexers was formed from the sum energy signal in a pattern trigger unit. The pattern trigger unit allowed only one triggering pulse to be present. Therefore, only the outputs from one strip at a time were those read out. The triggering pulses were also fed into two bit-pattern units (one for the recoils and one for the decay events), which were used to determine the strip where the recoil and decay events were taking place i.e. the horizontal position of the event.

Two different amplification channels were also used to process the signals from the avalanche counter. In addition to the energy signals, a timing signal was extracted for every event from the avalanche counter.

3.4.3 Trigger conditions

For each event to be measured a trigger, typically any signal from the RITU focal plane Si detector, was needed. Upon generation of this signal several logic gates were produced to record all the signals from the RITU detectors and from each of the γ-ray detectors both at the target area and at the focal plane.

The time of the trigger was recorded to 1 μs precision by a 32 bit continuously running clock. This clock cycling every 72 minutes provides a global time with which to associate separate events. At the same time, short (6 μs) gates were opened to receive the prompt signals both from the γ-ray detectors at the target position together with their associate TDC and TAC signals and from the Si, MWPAC and quadrant Si detectors at the RITU focal plane. Longer (32 μs) gates were opened for the signals from the focal plane γ-ray detectors and their associate TDC and TAC signals to read isomeric information. As a common time reference (Si detector) was used for the timing of all detector systems, relative timing between the detectors can be deduced. Since every event was stamped by the absolute clock signal complete timing information was available for the RDT analysis.

3.4.4 Data acquisition

The data acquisition system consisted of two main parts: the acquisition electronics based on a set of VME crates with integrated electronics and a control workstation [Jon95]. All signals were fed via ADCs to ADC interface cards. The ADC cards were read out by the readout controller when a master trigger signal, usually the signal from the Si detector, was present. The events were stored to a high-speed memory in their raw data format. When the memory was filled the data blocks, containing several hundred events, were read out and converted into EUROGAM format [Cre91] by a Motorola Power PC processor unit. The data blocks were then transferred via a fiber distributed data interface (FDDI) card and optic fiber cables to a tapeserver, which was used to store the data blocks onto magnetic Exabyte tapes. The acquisition system was controlled using a SUN workstation running the MIDAS data acquisition control system. The workstation allowed the on-line sorting of the data using the EUROGAM type sorting programs without the need to review the data already stored onto tapes. It was also possible to view singles γ-ray energy spectra because each of the ADC controllers was able to collect singles data with on-board histogramming memory.

3.5 Data analysis

3.5.1 Data format

As mentioned in the previous section, in the present work the data were recorded on magnetic Exabyte tapes using Eurogam data format [Cre91]. The data were stored on the tape in blocks, each containing several hundred events, which consisted of all the data collected when the master trigger was present. In the first part of the ^{176}Hg measurement this master trigger was either a signal from the Si detector or a γ-γ event. One event could contain several of the following parameters:

- recoil or α-particle energy
- Si detector strip number
- vertical position of a recoil or an α-particle
- clock word
- γ-ray energy
- γ-ray detection time compared to RF signal (TDC)
- time difference between the detection of a recoil and a (prompt or delayed) γ-ray (TDC/TAC)
- time difference between the detection of the first and the second (prompt or delayed) γ-ray in a γ-γ coincidence event (TAC)
- time difference between the detection of a delayed γ-ray and an event from the gas-detector (TAC).

The data were sorted using the Eurogam type sorting programs. For the search for the γ-γ coincidences the program package RADWARE [Rad95] was used.

3.5.2 Calibrations

In this section a recipe for analysing data from a recoil-decay-tagging measurement is described. To get a clean γ-ray energy spectrum several corrections and calibrations have to be done:

- energy-position corrections for each strip of the Si detector
- energy calibration for each strip
- position-position corrections for each strip
- energy calibrations for each Ge detector

Energy-position correction

As the total energy signal of a recoil or an α-particle is the sum of the signals from the top and the bottom ends of a strip, the measured energies depend on the vertical position of the interaction in the strip. This dependence is due to the fact that amplifications of the preamplifiers used to process the top and the bottom signals are not identical. In practice, the correction is done only for the α-particle energies, because it is not necessary to measure the recoil energies with a high precision. To eliminate this position dependence a correction coefficient can be determined from the spectrum where the α-particle energies are plotted as a function of the position. In this work the α-particle energy calibration was based on the known energies of the strongest α-particle energy peaks identified in the spectrum (internal calibration).

Position-position correction

A position correction has to be done if the low energy α-particle signals and the signals from the higher energy evaporation residues have been collected via two different amplification channels. In order to be able to connect the detected recoil to its subsequent α-decay occurring in the same position in the strip, it is necessary to find the position correlation between the two scales. This was the case in the measurements discussed in the present work. To avoid accidental corrections a nucleus with sufficiently short half-life has to be chosen for the position correction. However, the production rate of the nuclei should be high enough to get good statistics. Correlated nucleus-α-particle pairs are searched for with a fully open position window, but with a short searching time (around three half-lives). For each strip the position of the subsequent α-decay is plotted as a function of the recoil position (or vice versa).

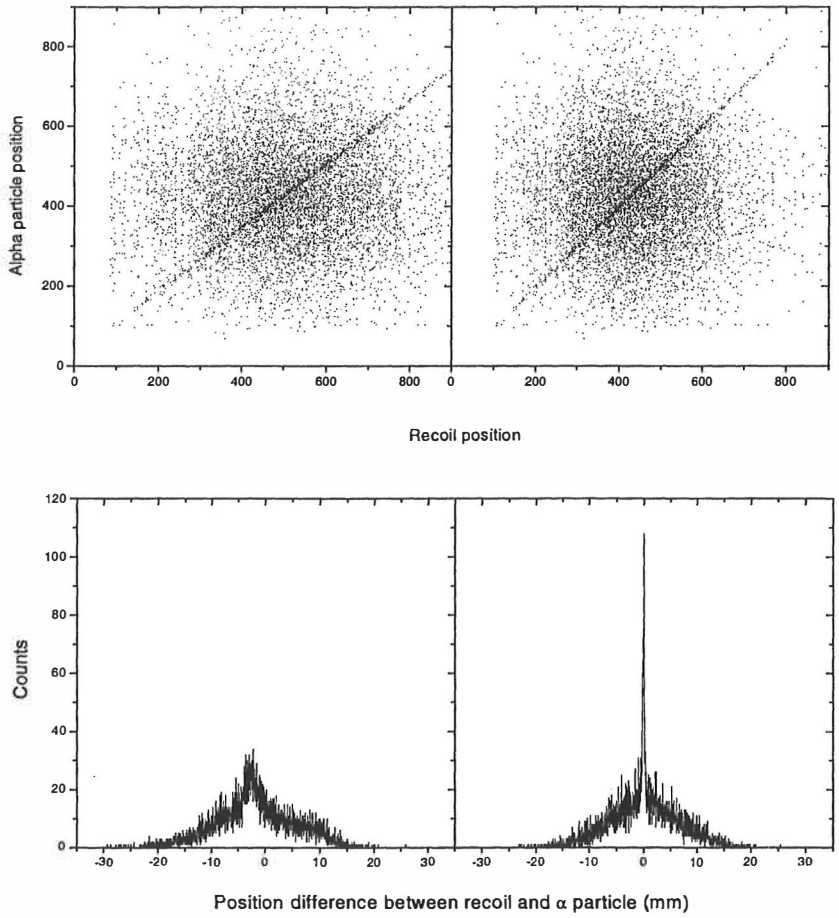

Figure 3.7 In the upper part of the figure positions of the subsequent α decays are plotted as a function of the recoil position. Position difference distributions for correlated recoil - α pairs are shown in the lower part. In both parts the figures on the left-hand and right-hand sides illustrate the situation before and after the position-position correction, respectively.

In Figure 3.7 (upper part, left-hand side) this plot is shown for strip 11 sorted from the data of the ^{182}Pb measurement. The true correlations form a straight line while random correlations are more evenly distributed. In order to make the position of the subsequent α-particle to correspond directly to the position where the recoil was detected the line is corrected to form a diagonal (Figure 3.7 upper part, right-hand side). The lower part of the Figure 3.7 illustrates the position difference between the recoil and the subsequent α-decay before and after the correction. The position resolution of the strip 11 i.e. the FWHM of the peak in Figure 3.7 (lower part, right-hand side) is about 340 μm after the correction.

Gamma-ray energy and efficiency calibrations

A mixed ^{152}Eu – ^{133}Ba source was used for the off-line energy and efficiency calibrations of the Ge detectors. The Doppler effect had to be taken into account in energy calibration because in the case of thin targets used in RDT measurements the γ rays are emitted from a moving residue. Due to the finite size of the Ge crystal the detection efficiency strongly depends on the energy of the detected γ-ray and, therefore, intensities extracted from the spectra had to be corrected for the detector efficiency when relative intensities of γ-ray transitions are needed. The absolute detection efficiencies of the Jurosphere II array and the Ge-detector array at the focal plane were measured using the 1.3 MeV energy peak from a calibrated ^{60}Co source.

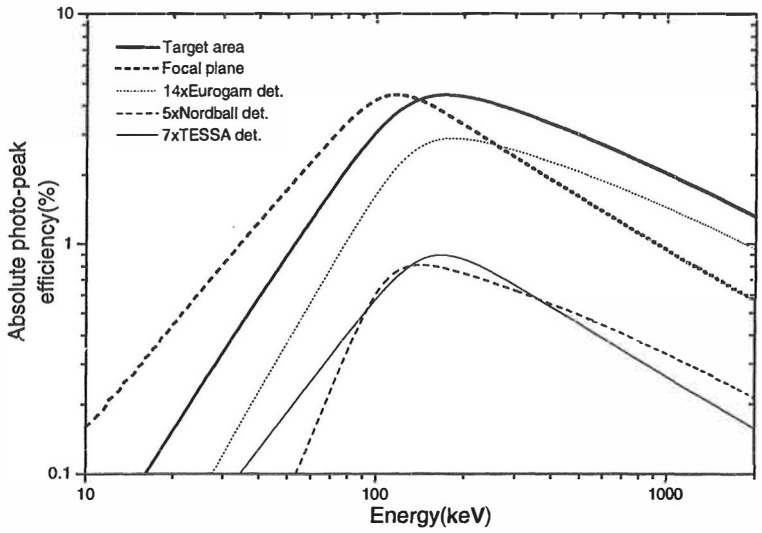

Figure 3.8 The absolute efficiency curves for the Ge-detector arrays both in the target area (thick solid line) and at the focal plane (thick dashed line) used in the Jurosphere II experiments. The absolute efficiency curves for the fourteen Eurogam Phase I (dotted line), five Nordball-type (dashed line) and seven TESSA-type (solid line) detectors are also shown.

The absolute efficiency curves for both the Jurosphere II array and the Ge-detector array at the focal plane are shown in Figure 3.8. The maximum efficiency of the Jurosphere II array is reached at the energy of 150 keV. The low-energy γ-rays are cut due to the absorbers which were used to reduce the high counting rate originating from low-energy X-rays. No absorbers were used at the focal plane. The efficiency of the Ge-detector array at the focal plane measured using the point-like source may slightly differ from the actual efficiency of the array. This is due to the fact that

during an experiment γ-rays are emitted by recoils implanted all over the 80mm×35mm Si-detector.

3.5.3 Recoil-Decay-Tagging (RDT) method

The Recoil-Decay-tagging (RDT) method is especially suitable for separating weak fusion-evaporation channels from the dominant background consisting primarily of fission products and transfer reaction products. In many cases the small fusion-evaporation cross-section is also fragmented into many channels and, therefore, it is essential to use a method, like RDT, to separate the channel of interest. If the half-life of the decaying fusion residue is short compared to the average time difference between events in one detector pixel at the focal plane Si detector a clean γ-ray energy spectrum can be generated. The RDT method was first used at GSI to probe the shape of ^{180}Hg [Sch86, Sim86]. The basic idea of the method is to identify a recoil via its subsequent characteristic radioactive decay. Only those γ-ray events detected in coincidence with the identified recoil are accepted. In the present work all nuclei studied decay via α emission and their half-lives are short enough to get sufficiently clean γ-ray energy spectrum. The correlated recoil- α pairs were searched for within a certain time limit, which usually was three times the half-life of the decaying recoil, and within a position window (about 1 mm) determined from the position difference distribution spectrum obtained from the calibrations. The time for each event was obtained from its clock stamp.

When sorting the data the first thing was to check whether a Si detector event was a good recoil or decay event i.e. whether the energy of the event passed the recoil or α energy gate. In the case of a good recoil event the detection time, the detected γ-ray energies and the recoil-γ TAC signal in the same event were stored into two-dimensional tables according to the horizontal and vertical positions of the recoil. Later, if a good decay event was found, the corresponding recoil was searched for backwards in time in the same strip and within the position window. The recoil, which was found closest in time, was chosen and its parameters were restored. The γ rays occurring in coincidence with this recoil were accepted as good γ-ray events. In practice, the coincidence requirement was filled when the recoil-γ TAC condition was

passed. In some cases the background caused by adjacent α-peaks was subtracted from the γ-ray energy spectrum.

Using the recipe described above a γ-ray energy spectrum consisting of transitions originating from the studied isotope can be generated. The efficiency of the method is demonstrated in Figure 3.9, where γ-ray energy spectra from the $^{36}Ar + ^{144}Sm \rightarrow ^{180}Hg^*$ reaction are shown. To generate the upper most spectrum only the presence of the master trigger (either a recoil event or a γ-γ event) was demanded. The centre spectrum shows γ rays in coincidence with fusion-evaporation residues, while in the lowest spectrum the γ-ray energy spectrum obtained by gating with fusion evaporation residues and tagging with ^{176}Hg α decays is shown. The lowest spectrum has also been corrected for background from adjacent α-peaks. The recoil-gated γ-ray energy spectrum is clearly dominated by γ rays from ^{176}Pt produced in the strong (^{36}Ar,2*p*2*n*) fusion-evaporation channel. These γ rays are absent in the recoil-gated α-tagged spectrum. In this spectrum there are seven strong lines, which are firmly assigned to originate from ^{176}Hg.

As mentioned above the RDT method is based on the search for correlated recoil-α-particle pairs. There is always a possibility that the found pair is produced accidentally. This is more likely when the counting rate in the focal plane Si detector is too high i.e. the time between the events is too short compared to the searching time. This can even lead to rejection of the strips, where the counting rate is so high that no clean γ-ray energy spectrum can be produced. This was the case in the ^{184}Pb measurement where one fourth of the strips were not used. This is discussed in more detailed in Chapter 4.

The number of accidental recoil-α correlation pairs (N_{acc}) can be estimated by using the following formula [Sch84]:

$$N_{acc} = DR\left[1 - e^{-rT}\right] \qquad (3.6)$$

where D is the duration of the experiment, R and r are the average counting rates of recoils and α-particles, respectively and T is the searching time. If $rT << 1$ then formula (3.6) can be expressed in the simplified form

$$N_{acc} = DRrT = \frac{n_R n_\alpha T}{D} \qquad (3.7)$$

where n_R and n_α are the number of recoils and α-particles observed during the experiment, respectively. According to formula (3.7) the number of random events grows linearly with the searching time while the amount of real events grows as $1-2^{-n}$, where n is the number of half-lives used as the searching time. This can be utilised when trying to distinguish between the real γ-ray energy peaks and the random background peaks. This is demonstrated in section 4.1.1, where the method is used to separate the ^{176}Hg γ-ray energy peaks from those of ^{176}Pt.

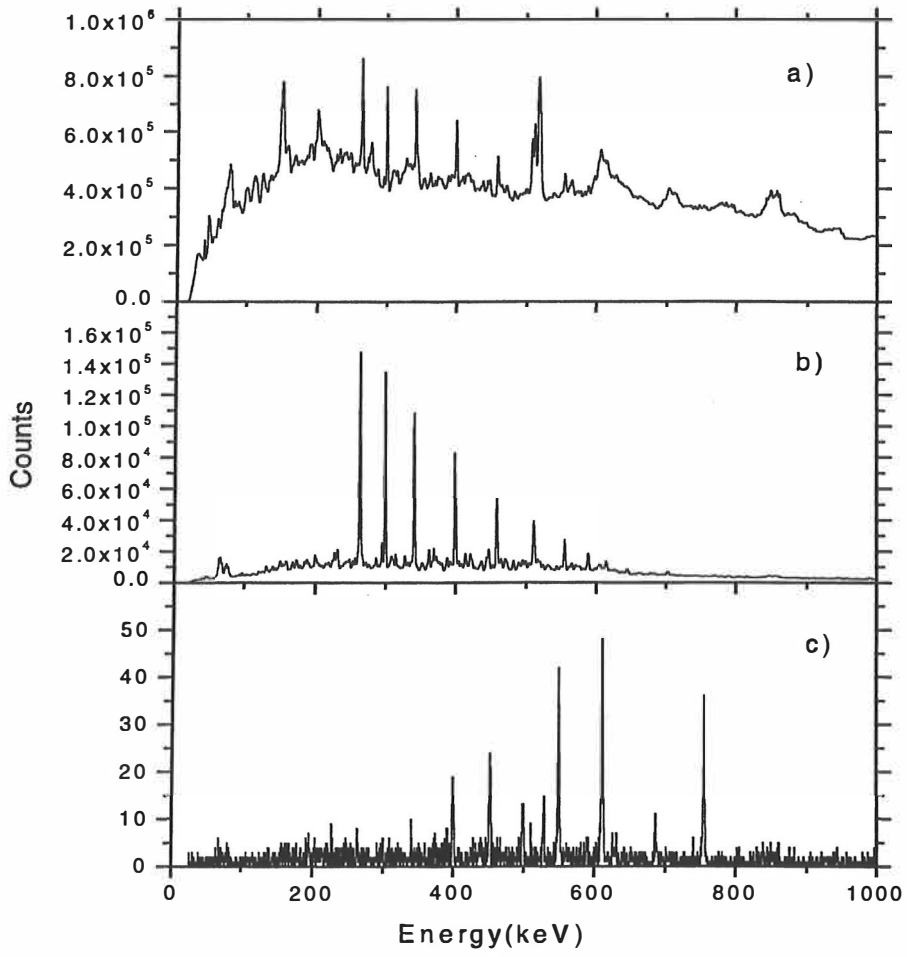

Figure 3.9 a) A γ-ray energy spectrum from the ^{36}Ar + ^{144}Sm → ^{180}Hg* reaction, b) recoil-gated energy spectrum of γ rays, c) γ-ray energy spectrum obtained by gating with fusion evaporation residues and tagging with ^{176}Hg α decays.

4. Study of neutron-deficient Hg, Tl and Pb isotopes

All the measurements in the present work have been carried out at the accelerator laboratory of the University of Jyväskylä (JYFL). The heavy ions used were produced in an ECR ion source and the acceleration of the ions was performed in the K=130 cyclotron [Hei95]. Recoiling fusion-evaporation residues were magnetically separated in flight from the background of the primary beam and fission products using the RITU gas-filled separator [Lei95a]. To detect prompt γ rays from the target Jurosphere and Jurosphere II arrays consisting of Compton-suppressed Ge detectors were used. In the Jurosphere II experiments there was also a small Ge-detector array around the focal plane Si detector to detect delayed γ rays.

4.1 Neutron-deficient Hg nuclei

The shape coexistence phenomenon in Hg nuclei was first observed when isotope shift measurements revealed a sharp shape transition in the ground states between odd-mass ^{187}Hg and ^{185}Hg isotopes. This change was interpreted as a transition from a weakly oblate shape to a more deformed prolate structure resulting from the existence of a prolate and an oblate energy minimum of nearly the same depth [Fra75, Bon76]. Nowadays there exists a large body of experimental information supporting the coexistence of different shapes at low excitation energies in mercury isotopes. In neutron-deficient even-mass Hg isotopes the properties of the weakly oblate ground-state band remain rather constant with decreasing neutron number until in ^{188}Hg, where the band is crossed by an intruding deformed band associated with a prolate-deformed energy minimum [Woo92]. The prolate states assumed to result from the excitation of four protons across the Z=82 shell gap into the $h_{9/2}$ and $f_{7/2}$ orbits [Naz93, Lan95] minimise their energies in ^{182}Hg [Dra88]. However, they still lie above the ground state [Bin95], which is predicted to evolve from the oblate shape towards a spherical shape [Naz93]. In accordance with these theoretical predictions, a further increase in the excitation energy of the prolate band was observed in ^{178}Hg [Car97]. In the same experiment three relatively high-energy γ rays were unambiguously assigned

to ^{176}Hg. However, on the basis of this experimental information the question of a possible appearance of a prolate structure in ^{176}Hg remained unresolved.

In the present work an improved in-beam γ-ray spectroscopy study of ^{176}Hg to confirm the tentative assignments of ref. [Car97] and to probe further its yrast line towards higher spin has been carried out. In addition, for the first time γ rays originating from ^{174}Hg have been observed.

4.1.1 ^{176}Hg: experimental results

Prompt γ rays from ^{176}Hg were resolved from those arising from the dominant background of fission and other reaction products by using the unique properties of the α decay of ^{176}Hg (E_α= 6750 keV, $t_{1/2}$ = (18 ± 10) ms [Pag96]) in an RDT measurement. Excited states of ^{176}Hg were populated via the ^{144}Sm(^{36}Ar,4n) fusion evaporation channel at the bombarding energy of 190 MeV. The target consisted of a single 500 μg/cm^2 self-supporting metallic ^{144}Sm foil of 92.4% enrichment. Prompt γ rays were detected by the Jurosphere array described in section 3.3.2.

The transmission of RITU for the fusion evaporation residues was determined from the fraction of the strongest γ-γ coincidences in ^{176}Pt [Ced90] which were also in coincidence with recoils detected in the focal plane Si detector. The value obtained was about 24%. Approximately 50% of the α particles emitted by the recoils were detected with full energy. At a typical beam intensity of 15 particle nA, limited by the Ge singles counting rates, the total counting rate in the Si strip detector was about 800 counts/s. The effective Si-detector granularity of about 200 was sufficiently high to allow the selection of the ^{176}Hg recoils through correlation with their subsequent α-decay.

The events corresponding to the observation of a recoil together with a subsequent α decay at the same position in the Si detector within a maximum time interval of 100 ms were selected in the data analysis. The resulting α-particle energy spectrum is shown in Figure 4.1. The α decay peaks labelled in this figure were identified using the known α-particle energies of the other isotopes produced in this reaction.

Approximately 240 hours of effective beam time yielded about 90000 ^{176}Hg recorded α-decays from which the estimated cross-section for the reaction ^{144}Sm(^{36}Ar,4n)^{176}Hg is deduced to be about 5 μb. The half-life of ^{176}Hg was determined from the spectrum of time differences between correlated recoil-^{176}Hg α pairs, shown in the inset of Figure 4.1. The first component originates from the decay of ^{176}Hg, while the second component represents the random background from false correlations. Using the method described in reference [Lei81], the value obtained was $t_{1/2}$ = (21 ± 3) ms. This is consistent with the earlier value of $t_{1/2}$ = (18 ± 10) ms measured in reference [Pag96].

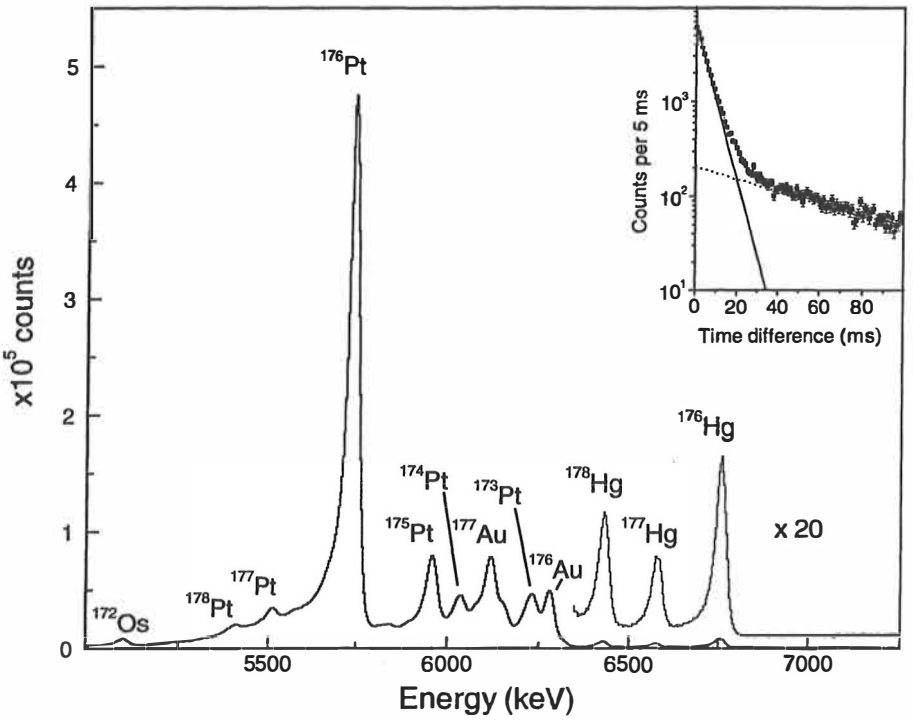

Figure 4.1 Energy spectrum of α particles observed within a 100 ms time interval after the detection of a recoil at the same position in the Si strip detector. In the inset the distribution of recoil-α time differences for events in the ^{176}Hg peak is shown. The solid line is assigned to the decay of ^{176}Hg, while the dashed line represents the random background from false correlations.

The energy spectrum of γ rays obtained in coincidence with detected recoils is shown in Figure 4.3 a). It is dominated by γ rays from ^{176}Pt produced in the (^{36}Ar,2p2n)

fusion evaporation channel. These γ rays are hardly visible in Figure 4.3 b), which shows a recoil-gated γ-ray spectrum obtained by correlating with the ^{176}Hg α-decay. In this spectrum there are seven strong lines (400.9, 453.2, 500.5, 529.9, 551.0, 613.3 and 756.4 keV) which we firmly assign to originate from ^{176}Hg. Three of these (551.0, 613.3 and 756.4 keV) were seen by Carpenter et al. [Car97]. In addition, there are clear peaks at energies of 195.5, 375.1 and 590.4 keV, which can be assigned to ^{176}Hg. These assignments can be confirmed utilising the method described in section 3.5.3. In Figure 4.2 the number of counts in the 196, 375 and 590 keV peaks together with the number of counts in the 530 and 453 keV peaks originating from ^{176}Hg and the 264 and 300 keV peaks from ^{176}Pt are plotted as a function of the searching time. The number of random events in the 264 and 300 keV peaks grows linearly with the searching time as expected. The amount of real events in the 530 and 453 keV peaks grows as $1 - 2^{-n}$, which also is in accordance with expectations. The lines representing the counts in the 196, 375 and 590 keV peaks follow the behaviour of the real events. Although the RDT method provides a unique identification of the tagged γ-rays the procedure above is used to eliminate the small possibility that the peaks were due to random events.

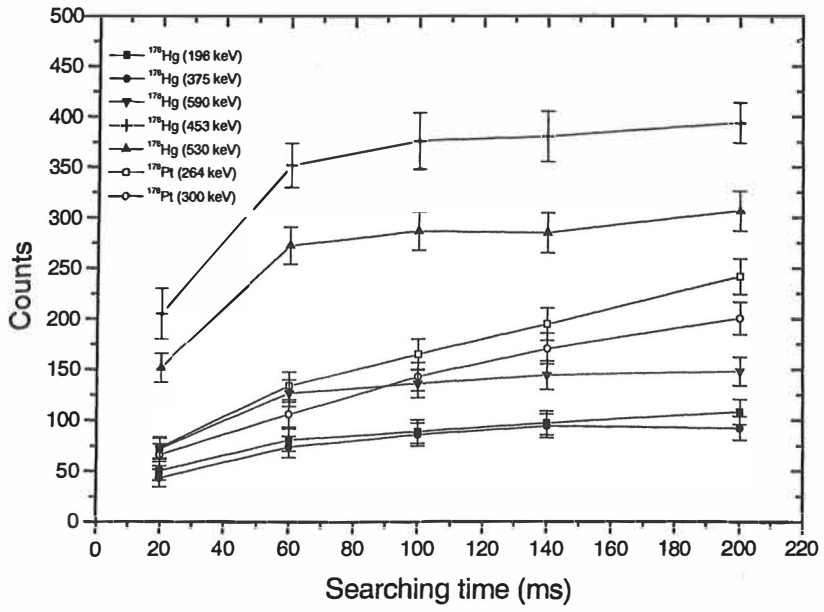

Figure 4.2 The number of counts in the 196, 375 and 590 keV peaks together with the number of counts in the 530 and 453keV peaks originating from ^{176}Hg and the 264 and 300 keV peaks from ^{176}Pt plotted as a function of the searching time.

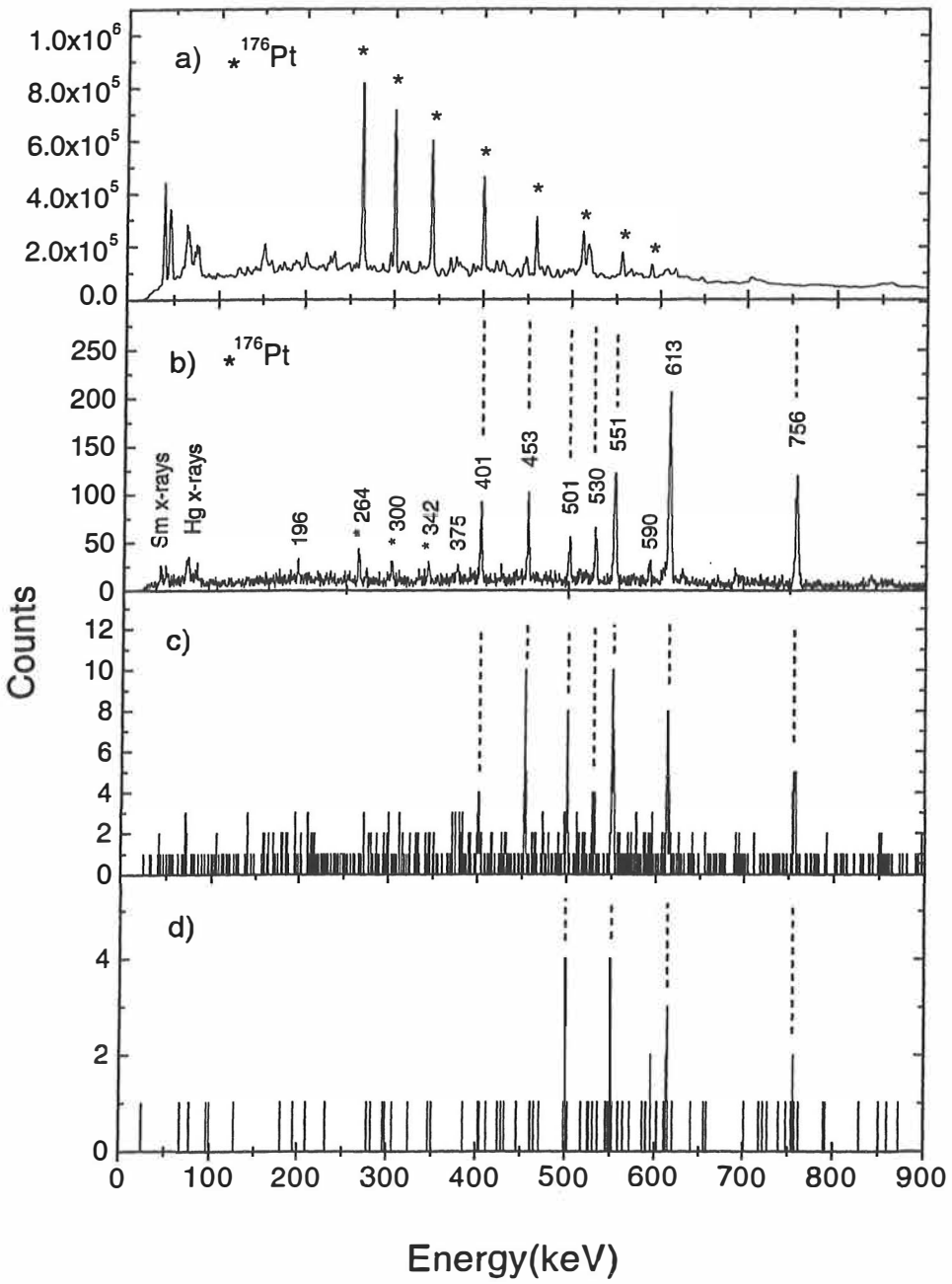

Figure 4.3 a) Energy spectrum of γ-rays in coincidence with fusion evaporation residues detected in the RITU focal-plane Si-detector. b) γ-ray energy spectrum obtained by gating with fusion evaporation residues and tagging with ^{176}Hg α-decays. c) Sum of the recoil-gated and α-tagged γ-γ coincidence spectra gated on seven strongest transitions in the spectrum of b). d) Recoil-gated and α-tagged coincidence spectrum gated on the 453 keV transition.

In order to construct the level scheme recoil-gated α-tagged γ-γ coincidence data were required. Examples of coincidence spectra are shown in the two lowest parts of Figure 4.3: Figure 4.3 c) is a sum of the coincidence spectra gated on the seven strongest peaks of Figure 4.3 b) and Figure 4.3(d) is a spectrum gated on the 453.2 keV peak. The two spectra demonstrate that the 453.2, 500.5, 551.0, 613.3 and 756.4 keV γ rays are emitted as a cascade.

The intensity ratios (R_I) of γ rays observed by the Ge detectors at 134° and 158° to those observed by the 79° and 101° Ge detectors for the known E2 transitions in ^{176}Pt marked in Figure 4.3 a) are shown in Table 4.1. The ratios extracted for the 551.0, 613.3 and 756.4 keV transitions in ^{176}Hg are within the errors bars of those for the ^{176}Pt E2 transitions thus confirming the E2 character (see Table 4.1). For the weaker 453.2 and 500.5 keV transitions only tentative E2 assignments were possible. These arguments together with γ-ray coincidence and intensity information were used to generate the decay scheme of Figure 4.4. The placement and the cascade character of the 529.9 and 400.9 keV γ rays remain tentative.

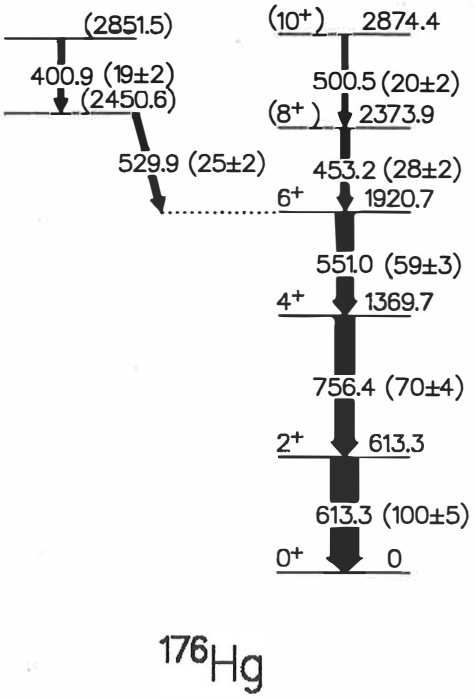

Figure 4.4 Level scheme of ^{176}Hg deduced from the present data. The measured intensities are given in parentheses next to the transition energies.

Table 4.1 Properties of γ-ray transitions of ^{176}Pt and ^{176,177}Hg obtained from the recoil-gated and recoil-gated α-tagged spectra, respectively.

E_γ(keV)	Nucleus	Intensity*	I^π_i	I^π_f	R_I
613.3(3)	^{176}Hg	100(5)	2^+	0^+	1.24(13)
756.4(3)	^{176}Hg	70(5)	4^+	2^+	1.29(17)
551.0(3)	^{176}Hg	59(3)	6^+	4^+	1.40(25)
453.2(3)	^{176}Hg	28(2)	(8^+)	6^+	
500.5(5)	^{176}Hg	20(2)	(10^+)	(8^+)	
529.9(5)	^{176}Hg	25(2)			
400.9(5)	^{176}Hg	19(2)			
590.4(5)	^{176}Hg	7(2)			
375.1(5)	^{176}Hg	6(1)			
195.5(5)	^{176}Hg	3(1)			
264	^{176}Pt		2^+	0^+	1.16(10)
300	^{176}Pt		4^+	2^+	1.26(5)
342	^{176}Pt		6^+	4^+	1.33(7)
1105	^{176}Pt		7^-	6^+	0.79(9)
1135	^{176}Pt		5^-	4^+	0.92(7)
638.3(5)	^{177}Hg	100(12)	$(17/2^+)$	$(13/2^+)$	
535.9(5)	^{177}Hg	71(8)	$(21/2^+)$	$(17/2^+)$	
621.3(5)	^{177}Hg	69(10)	$(25/2^+)$	$(21/2^+)$	
450.4(5)	^{177}Hg	54(7)			
391.3(5)	^{177}Hg	44(6)			

*The intensities are normalised to the 613 keV and 638 keV transition in the case of ^{176}Hg and ^{177}Hg, respectively.

4.1.2 ^{177}Hg: experimental results

In the measurement described in the previous section the odd-mass ^{177}Hg isotope was produced as a by-product via the ^{144}Sm(^{36}Ar, 3n) fusion evaporation channel. Although the energy of the ^{36}Ar beam was optimised for the production of ^{176}Hg isotope about 60000 α-particles from the ^{177}Hg decay were detected in total. An RDT analysis was performed to generate a recoil-gated α-tagged γ-ray energy spectrum shown in Figure 4.5 a). In the correlation analysis the relatively long half-life, $t_{1/2}$=130(5) ms [Sel91], resulted in increased amount of accidental correlations, thus increasing the number of background events in the γ-ray spectrum. In Figure 4.5 b) a γ-ray energy spectrum corrected for background from adjacent α-peaks is shown. In the spectra the γ-ray energy peaks originating from ^{176}Pt and ^{176}Hg have been marked with an asterisk and a cross, respectively and the energies of the peaks tentatively

assigned to ^{177}Hg are labelled. In Table 4.1 the energies of the seven γ-ray peaks are listed together with their intensities relative to the most intensive 638 keV peak. The amount of collected γ-ray events is low compared to the amount of correlated α-particles, which might be due to an isomeric state. Unfortunately, there was no focal plane Ge-detector array in use when the measurement was performed.

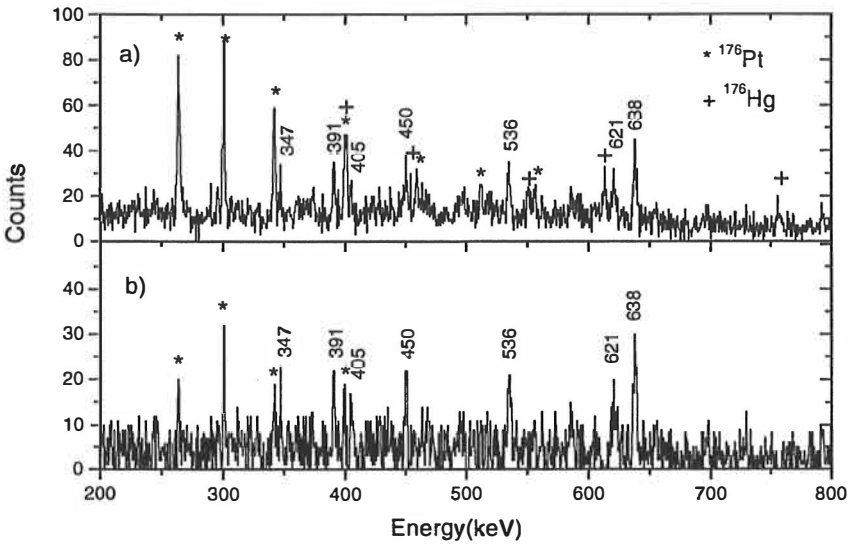

Figure 4.5 a) Energy spectrum of prompt γ-rays obtained by gating with fusion evaporation residues and tagging with ^{177}Hg α-decays. b) A recoil-gated α-tagged γ-ray energy spectrum corrected for background from adjacent α-peaks.

If a similar procedure as in the previous section is used to distinguish real events from random events the number of counts in the 391, 450, 536, 622 and 638 keV peaks is observed to follow the behaviour of the amount of real events. Therefore, these peaks can be assigned to originate from ^{177}Hg. The assignment of the 347 and 405 keV transitions remains unclear due to the limited statistics. For the same reason it has not been possible to use the γ-γ coincidence information to construct a level scheme for ^{177}Hg. A tentative level scheme plotted in Figure 4.6 has been constructed on the basis of the relative intensities of the γ-ray peaks. The 638, 536 and 621 keV transitions have been assigned tentatively as the $(17/2^+)\rightarrow(13/2^+)$, $(21/2^+)\rightarrow(17/2^+)$ and

$(25/2^+)\rightarrow(21/2^+)$ transitions, respectively on the basis of the energy level systematics of heavier odd-mass Hg isotopes.

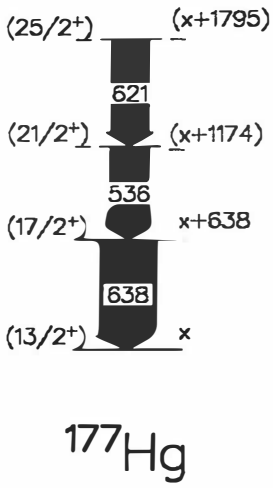

Figure 4.6 Tentative level scheme of ^{177}Hg deduced from the present data.

4.1.3 ^{174}Hg: experimental results

The Hg nuclei studied in this work lie very close to the proton drip line as illustrated in Figure 1.1. Before a very recent identification of two new isotopes, ^{172}Hg and ^{173}Hg, by their characteristic α-decay [Sew99] ^{174}Hg was the lightest known Hg isotope. Excited states in ^{174}Hg were observed for the first time in the present work although the cross-section for the production of ^{174}Hg is only of the order of 200 nb.

Excited states in ^{174}Hg were populated using the ^{112}Sn(^{64}Zn,2n) fusion evaporation channel. The Q value for the compound nucleus formation in this reaction is –142.77 MeV which is much less than that of the ^{144}Sm(^{36}Ar,6n) reaction (-92.01 MeV) used to produce ^{174}Hg isotope for the first time [Uus97]. The large negative Q value together with the used 2n fusion-evaporation channel result to a low excitation energy of the compound nucleus (~38 MeV). In general, the lower the excitation energy is the better the fusion-evaporation survives competition against fission. In addition, with higher excitation energies the charge-particle evaporation channels dominate over the neutron-evaporation channels. To obtain the optimum production yield the

excitation function for the $^{112}Sn(^{64}Zn,2n)^{174}Hg$ reaction was measured with energy in the centre of the target being 277, 280, 284 and 287 MeV. The beam energy of 280 MeV corresponded the maximum cross section of about 230 nb, which is ten times higher than that measured for the $^{144}Sm(^{36}Ar,6n)$ reaction in reference [Uus97]. The aim of the experiment was also to produce ^{173}Au nuclei via the p2n fusion-evaporation channel and thus, the higher energy of 284 MeV was used most of the time. The target used in the experiment was a 500 $\mu g/cm^2$ thick self-supporting metallic ^{112}Sn foil. Prompt γ rays from ^{174}Hg were resolved from those arising from the dominant background of fission and other reaction products by utilising the RDT method. The Jurosphere II array was used to detect prompt γ rays. One Compton-suppressed Ge detector was placed at the focal plane to detect delayed γ-rays.

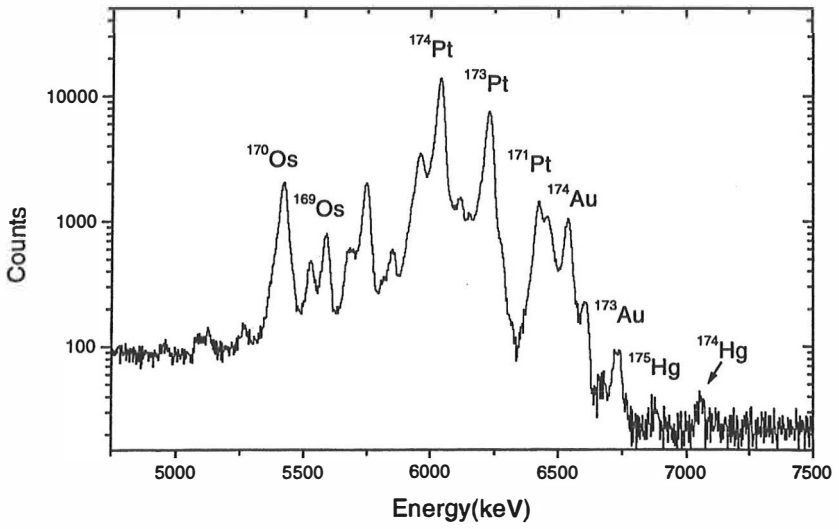

Figure 4.7 A singles energy spectrum of α particles from the ^{64}Zn + ^{112}Sn reaction at the beam energy of 280 MeV. When creating the spectrum an additional condition that the gas counter signal is not present has been demanded.

Due to the target problems only about 900 full-energy ^{174}Hg α-decays were recorded in 230 hours. A singles α-particle energy spectrum for the ^{64}Zn + ^{112}Sn reaction at the energy of 280 MeV is shown in Figure 4.7. The half-life of ^{174}Hg was determined to be $t_{1/2}$ = 1.7(4) ms using the method described in [Lei81]. This is consistent with the earlier values of $t_{1/2} = 2.1^{+1.8}_{-0.7}$ ms [Uus97] and $t_{1/2} = 1.9^{+0.4}_{-0.3}$ ms [Sew99]. Prompt γ rays emitted by ^{174}Hg were selected using the RDT technique. In Figure 4.8 a γ-ray energy

spectrum obtained by gating with recoils and tagging with ^{174}Hg α-decays is shown. In this spectrum there are two clear peaks at the energies of 647 and 588 keV. These transitions can be firmly assigned to originate from ^{174}Hg. In addition, small peaks at the energies of 159, 268 and 821 keV can be seen in the spectrum. In Table 4.2 the energies of the five γ-ray energy peaks are listed together with their intensities relative to the most intensive 647 keV peak regarded as the $2^+ \rightarrow 0^+$ transition. The level systematics in Hg, shown in Figure 4.9, supports this assignment. According to the intensity information 588 and 821 keV transitions should be assigned as the $4^+ \rightarrow 2^+$ and $6^+ \rightarrow 4^+$ transitions, respectively. However, the systematic behaviour of the $6^+$and 4^+ levels supports the reversed order. To firmly assign these transitions better statistics is needed.

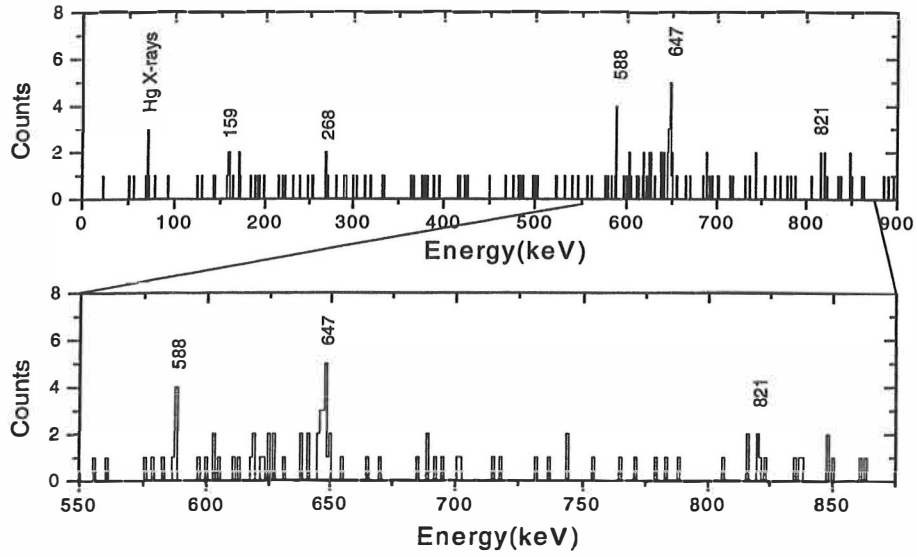

Figure 4.8 Energy spectrum of prompt γ-rays obtained by gating with fusion evaporation residues and tagging with ^{174}Hg α-decays.

Table 4.2 Properties of γ-ray transitions of ^{174}Hg.

E_γ(keV)	Nucleus	Intensity	I^π_i	I^π_f
647.3(5)	^{174}Hg	100(25)	(2^+)	(0^+)
587.9(5)	^{174}Hg	30(14)		
821.0(5)		29(15)		
268(1)		20(9)		
159(1)		14(6)		

*The intensities are normalised to the 647 keV transition.

4.1.4 Discussion

Systematics

It is interesting to span the level-energy systematics of even-mass Hg isotopes down to ^{176}Hg and ^{174}Hg. In the present work excited states have been observed for the first time in the ^{174}Hg isotope. In addition, the results confirm earlier tentative assignments of the ^{176}Hg level scheme [Car97] up to the 6^+ level. From Figure 4.9 it can be seen that the energies of the first excited 2^+ and 4^+ states in ^{176}Hg and ^{174}Hg lie higher than in any other Hg isotope except the closed-shell nucleus ^{206}Hg$_{126}$. In accordance with the theoretical predictions [Naz93], the rise in the 2^+ and 4^+ level energies suggest a transition towards a spherical ground state as already pointed out in reference [Car97].

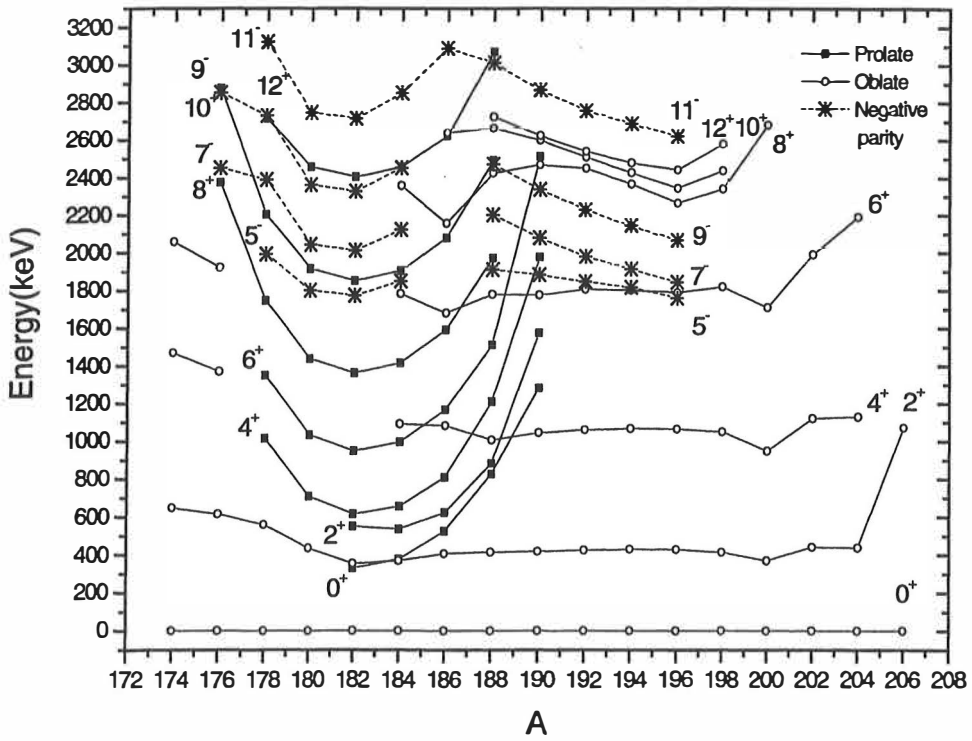

Figure 4.9 Level systematics for the even-mass Hg isotopes taken from references [Kon00, Dra88, Bin95, Den95, Ma93, Han88, Hüb86, Fot96, Meh91, Wau94, Wau94a Fir96] and present work.

The similarity between the observed intruder prolate bands in the even-mass Pt, Hg and Pb isotopes close to the neutron mid-shell is well-known [Dra94]. In Figure 4.10 the kinematic moments of inertia, J_{kin} derived from the experimental γ-ray transition energies (E_γ) for the yrast sequences in the Hg and Pt isotones with N = 96, 98 and 100, are plotted as a function of γ-ray energy. The kinematic moment of inertia can be calculated using following formula

$$J_{kin}(I) = \frac{I}{\omega(I)} \approx \hbar^2 \frac{2I-1}{E_\gamma} \qquad (4.1)$$

where I and $\omega(I) = \frac{dE(I)}{dI}$ are the angular momentum and the rotational frequency, respectively. In Figure 4.10 the appearance of the prolate band is manifested by the change towards a slightly increasing and smoothly behaving J_{kin}. Similarities in the J_{kin} values for the prolate bands are especially striking between pairs of isotones. Furthermore, the values extracted from the (10^+) to (8^+) and (8^+) to (6^+) transitions observed in the present work are very close to the corresponding values for ^{174}Pt [Dra91]. The change in J_{kin} at $E_\gamma \approx 0.5$ MeV for the yrast line in ^{176}Hg can be regarded as being due to a crossing prolate band, as seen in ^{174}Pt [Dra91].

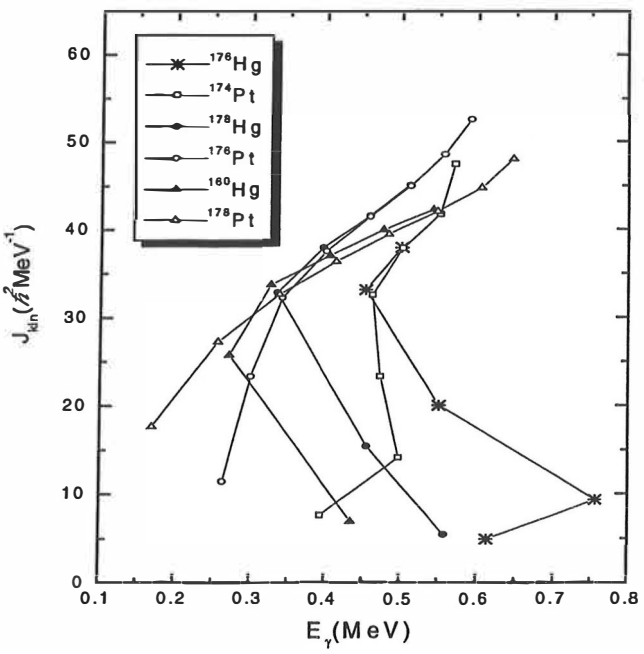

Figure 4.10 Kinematic moments of inertia J_{kin} as a function of γ-ray energy, derived from the experimental yrast level energies for the Hg and Pt isotones with N = 96 [Dra91] and from the present work, 98 [Car97,Ced90] and 100 [Dra88,Dra86].

Determination of perturbed 0^+ band-head energies

In order to extract the energy difference between the assumed prolate and weakly oblate band heads from the present data for ^{176}Hg a simple two-band mixing model similar to that in reference [Dra86] has been used. In these calculations the experimentally observed states are formed when close-lying weakly oblate and more deformed prolate states with same spin and parity interact. As a result of the interaction the states are mixed and repel each other. The interaction (V) between the unperturbed 0^+ states can be obtained from the formula [Dra86]:

$$V^2 = \left(E_u(0) - E_x(0)\right) \times \left(E_x'(0) - E_u(0)\right) \qquad (4.2)$$

where $E'_x(0)$ is the energy of the perturbed first excited 0^+ state (0^+_2) , $E_x(0)$ is the perturbed energy of the ground state i.e. 0 keV and $E_u(0)$ is the unperturbed energy of the 0^+_2 state. The unperturbed 0^+_2 energy can be obtained from a fit of the formula

$$E_x(I) = AI(I+1) + B\left|I(I+1)\right|^2 + E_u(0) \qquad (4.3)$$

to the known states of energies $E_x(I)$ assumed to be unmixed members of the prolate band. By fitting this formula to the states from I=6 to 10 for ^{176}Hg, I=4 to 12 for ^{178}Hg and I=4 to 14 for ^{180}Hg the unperturbed band-head energies of 1201(30), 717(20) and 425(13) keV were extracted, respectively. In Figure 4.11 a plot of excitation energies as a function of I(I+1) for $^{176, 178, 180}$Hg is shown. The extrapolations to zero spin used to determine the $E_u(0)$ values are marked with the dashed lines. A value of 1210(30), 730(20) and 449(13) keV for the perturbed 0^+_2 states of $^{176, 178, 180}$Hg was extracted using a prolate-oblate interaction strength of approximately 100 keV. The interaction strength has been estimated from the values used in the similar calculation in reference [Dra88], where a fit to the energies of the spin 6 to 14 states and use of an 80 keV interaction resulted in the perturbed 0^+_2 state lying at 466 keV in ^{180}Hg. The extracted band-head energy of ^{176}Hg is about 500 keV higher than in ^{178}Hg revealing a rapid increase in the excitation energy of the prolate intruder structure with decreasing neutron number. In the Nilsson-Strutinsky calculations at zero spin of reference [Naz93, Naz97], no well-developed prolate minimum but a shoulder in the potential energy curve was predicted. The corresponding prolate configuration lies at about 1 McV above a shallow near-spherical ground state. At higher spin, because of its large moment of inertia, this configuration is expected to be favoured energetically, thus giving rise to irregular behaviour of the yrast band as observed in the present work. In

Figure 4.22 the band-head energies of the unperturbed prolate bands in light Hg isotopes are plotted as a function of neutron number.

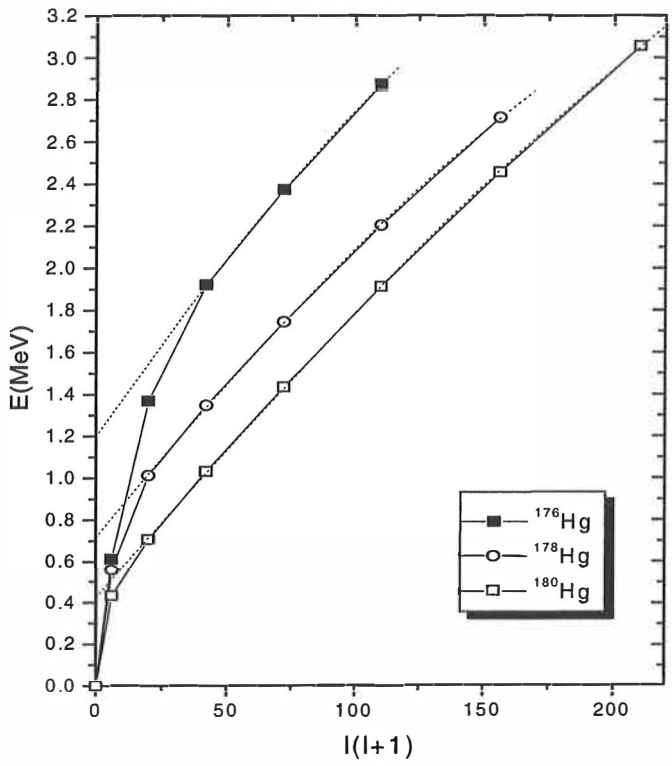

Figure 4.11 A plot of excitation energies as a function of spin for $^{176, 178, 180}$Hg. The extrapolations to zero spin used to determine the $E_u(0)$ values are marked with the dashed lines.

Non-yrast levels

The tentatively observed non-yrast levels in ^{176}Hg could be due to the negative-parity states similar to those observed in a number of even-mass isotopes of Hg as seen in Figure 4.9 [Ma93, Han88, Hub86, Den95]. The level with $I^{\pi} = 5^-$ is often the lowest observed member of the band. Near the neutron mid-shell yrast states lie very low in energy and, therefore, it is difficult to observe these negative-parity states having higher excitation energies. In $^{182, 184, 186}$Hg [Bin95, Den95, Ma93] isotopes these bands, with the deformation between normal and super deformed, are interpreted to be based on a two-quasineutron configuration ($\nu^2(g_{9/2} \otimes f_{7/2})$ or $\nu^2(g_{9/2} \otimes j_{15/2})$) intruding from above the N=126 shell gap. In lighter Os [Drac82] and Pt [Voi90, Ced90] nuclei these negative-parity bands seem to have strong octupole component at low spin

while the high-spin structure is dominated by a decoupled two-quasiparticle configuration. Recently, a rotational band based on octupole vibration crossed by a shape-driving two-quasiproton configuration ($\pi^2(i_{13/2} \otimes f_{7/2})$ or $\pi^2(i_{13/2} \otimes h_{9/2})$) has been observed in ^{178}Hg [Kon00]. In heavier Hg isotopes the negative-parity bands are based on two-quasineutron configuration [Ma93] while in lighter ones the two-quasiproton configuration becomes energetically favoured [Kon00].

Odd-mass nuclei

By comparing the level energies in even-even Hg isotopes with those of the $i_{13/2}$ bands in neighbouring odd-N isotopes, information from the coupling between the odd $i_{13/2}$ neutron and the even-even core can be obtained. In Figure 4.12 the energy level systematics of low-lying excited states of Hg isotopes is displayed. The excitation energies of the 2^+, 4^+, 6^+ and 8^+ levels for the even-N isotopes are plotted together with the energies of the $17/2^+$, $21/2^+$, $25/2^+$ and $29/2^+$ levels relative to the lowest lying $13/2^+$ states in odd-N isotopes. In Hg isotopes with $N \geq 104$ states associated with a weakly oblate shape are seen. The level energies of the odd-N isotopes (open circles) are almost degenerate with the level energies of their even-N neighbours (filled circles). The degeneracy indicates that the odd $i_{13/2}$ neutron (hole) is decoupled from the core. In other words, the nucleonic angular momentum j of the odd neutron is aligned with the rotational angular momentum of the core and thus, the neutron can be considered as a spectator not affecting the structure of the core nucleus. According to the particle-rotor model this alignment is due to the Coriolis force having a large effect on weakly deformed nuclei and nuclei having small values of the projection of j on the symmetry axis (Ω). At $100 \leq N \leq 108$ a splitting between the energies of the presumed prolate-deformed 2^+, 4^+, 6^+ and 8^+ levels in even (filled squares) and the $17/2^+$, $21/2^+$, $25/2^+$ and $29/2^+$ levels in odd (open squares) isotopes is observed. This indicates that the odd neutron is more strongly coupled to the core, which is typical for nuclei having a large prolate deformation and high value of Ω. In ^{183,185,187}Hg [Shi95, Han88a, Han88] and ^{181}Hg [Var97] isotopes these levels are associated with $9/2^+[624]$ and $7/2^+[633]$ configurations, respectively. Similar transition from the decoupled to the strongly coupled structure has also been observed in bands based on the $i_{13/2}$ configurations in odd-N Pt nuclei near N=108 [Ced98].

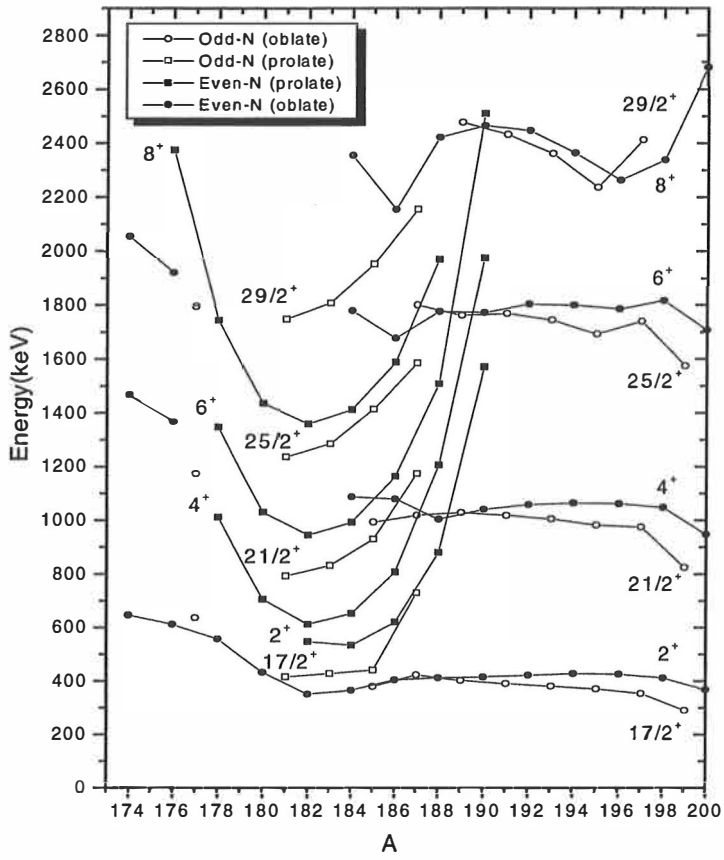

Figure 4.12 Level systematics for the Hg isotopes with 94≤N≤120 taken from references [Kon00, Dra88, Bin95, Den95, Ma93, Han88, Hüb86, Fot96, Meh91, Fir96, Var97, Shi95, Han88a, Gut83] and present work. The excitation energies of the 2^+, 4^+, 6^+ and 8^+ levels for the even-N isotopes are plotted together with the energies of the $17/2^+$, $21/2^+$, $25/2^+$ and $29/2^+$ levels relative to the lowest lying $13/2^+$ states in energy in odd-N isotopes. Filled (open) circles and squares represent the oblate and prolate deformed structures in even-N (odd-N) Hg nuclei, respectively.

In Pt [Ced98] and Os [Jos00] isotopes with N≤96 a transition into another regime, where the near-degeneracy between the level energies of the odd-N and even-N isotopes reappear, has been observed. This transition has been interpreted in two different ways [Ced98]. Firstly, assuming prolate deformation, the odd $i_{13/2}$ neutron occupies the low-Ω orbits and therefore, it is decoupled from the core. An alternative scenario suggests a transition into a regime with collective vibrational admixture in the low-lying excited states. This scenario is supported by the near-constant level spacings between the lowest excited states in $^{168, 170}$Pt [Kin98] and $^{171, 172}$Pt [Ced98].

Isotope $^{177}Hg_{97}$ seems to lie in the middle of the region where the change from the strong coupling to the decoupling of the odd $i_{13/2}$ neutron occurs if the systematic behaviour of the different structures in odd-N Hg isotopes follows that of the Pt and Os isotones. In ^{177}Hg the tentatively assigned $17/2^+$, $21/2^+$, $25/2^+$ levels lie clearly higher in energy than in the heavier ^{181,183,185}Hg isotopes. This rise in excitation energy resembles that seen in the neighbouring even-N Hg isotopes revealing a transition towards less deformed shape. The near-constant level spacings between the lowest excited states can be a sign of the change towards vibrational structures.

4.2 Neutron-deficient ^{182,184}Pb isotopes

In even-even Pb isotopes the intruder states were first identified in α- and β-decay studies using on-line isotope separators [Dup84, Dup87]. The low-lying excited 0^+ states associated with weakly deformed oblate structures have been observed to coexist with the spherical ground states in several Pb isotopes with $N \geq 106$ [Woo92, Bij96]. Evidence for a rotational structure built on such a state has been seen in ^{196}Pb [Pen87]. Low-lying deformed rotational structures have been observed at $I > 2\hbar$ by Heese et al. [Hee93] and Baxter et al. [Bax93] in ^{186,188}Pb. The bands similar to those observed in the corresponding isotones ^{184,186}Hg are associated with predicted [Naz93] prolate-deformed minima. In Pb nuclei the oblate and prolate intruder states are supposed to result from the excitation of two and four protons across the shell gap, respectively. The Nilsson-Strutinsky calculations, which reproduced the behaviour of the 0^+ energy of the intruder states in Hg isotopes, also predict lowest energies of the prolate states to appear at $N \approx 103$ for the Pb isotopes.

In the present work γ rays originating from the ^{182,184}Pb isotopes have been studied for the first time. The aim was to extend the knowledge of excited states in even-even Pb isotopes beyond the $82 < N < 126$ mid-shell.

4.2.1 Nucleus ^{184}Pb

The ^{148}Sm(^{40}Ca, 4n)^{184}Pb reaction was employed with a target thickness 500μg/cm^2 and 99.94% enrichment. The beam, consisting of 95% ^{40}Ca and 5% ^{40}Ar was delivered at the bombarding energies of 195 and 200 MeV. The q/A values of ^{40}Ca and ^{40}Ar are so close to each other, that the separation of these isotopes during the acceleration process is difficult. The use of such an impure beam increased the amount of background events. The Jurosphere array employed in conjunction with RITU was used to investigate ^{184}Pb.

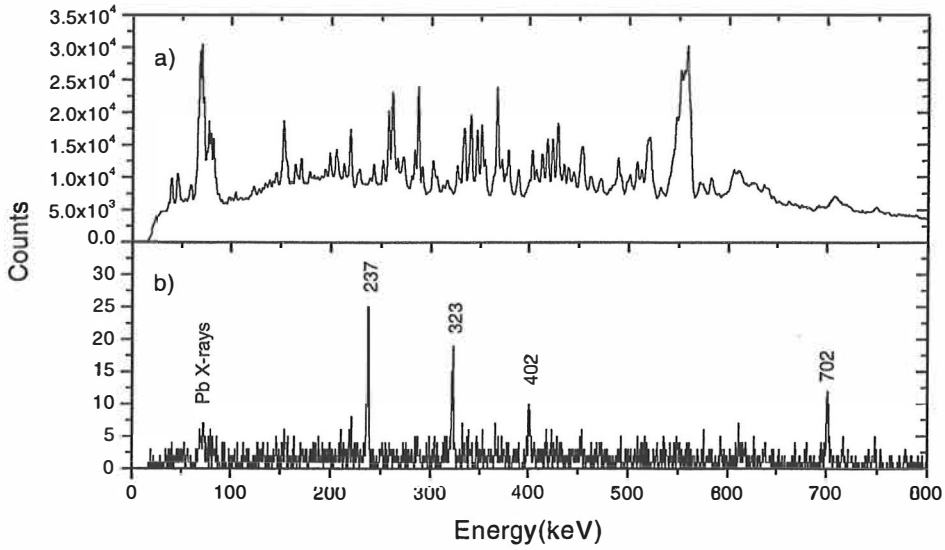

Figure 4.13 a) Energy spectrum of γ-ray transitions in coincidence with all fusion-evaporation residues detected at the RITU focal plane. b) Gamma-ray energy spectrum generated by gating with fusion evaporation residues and tagging with ^{184}Pb α-decays.

Figure 4.13 a) is a spectrum showing prompt γ rays in coincidence with all recoils detected at the RITU focal plane. It is dominated by γ rays from Hg isotopes produced in ^{148}Sm(^{40}Ca, αxn) and ^{148}Sm(^{40}Ar, xn) channels. Prompt γ rays emitted by ^{184}Pb were selected using the RDT technique. The searching time used to generate the recoil-gated α-tagged γ-ray energy spectrum shown in Figure 4.13 b) was 1.5 s. It is approximately three times the α-decay half-life of ^{184}Pb, $T_{1/2}$=0.55(6) s [Sch80].

About 9000 ^{184}Pb α-recoil correlated pairs were found. In this measurement one of the strips of the Si detector was not functioning and one quarter of the strips were not used because of too high counting rate. In those strips the probability to have an accidental correlation was too high. This is visualised in Figure 4.14 where the ^{184}Pb α-particle distribution (4.14 a)) and the distribution of all the recoils observed at the focal plane (4.14 b)) are plotted. The counting rate in the strips on the right-hand side of the Si detector is much higher than that on the left-hand side.

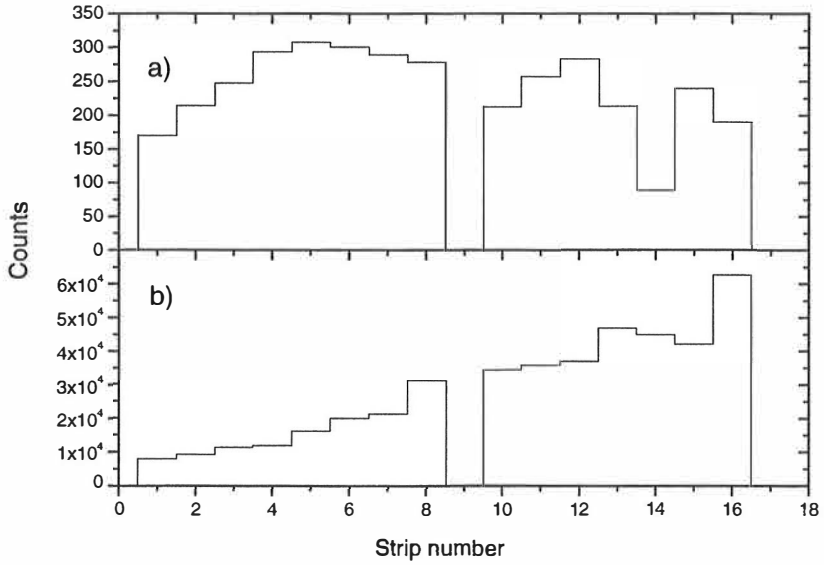

Figure 4.14 A Plot of a) the ^{184}Pb-alpha distribution and b) the distribution of all the recoils observed at the focal plane. The ^{184}Pb-alpha distribution is well centred while the total recoil counting rate in the strips on the right-hand side of the Si detector is much higher than that on the left-hand side.

Using the method described in [Lei81] a half-life value of 0.58(9) s for ^{184}Pb was deduced. This is consistent with the value obtained in the previous measurement [Sch80]. In Figure 4.13 b) the four γ-ray transitions clearly identified along with Pb X-rays can be seen. Due to the large background of γ rays from other nuclei these transitions are not observed in Figure 4.13 a). Figure 4.15 shows a tentative level scheme deduced using the α-tagged spectrum. The $I^{\pi} = (2^+)$ state is assigned an energy of 701.5 keV on the basis of 2^+ energy level systematics in Pb isotopes; the only intense peak in the region of the spectrum where the $2^+ \rightarrow 0^+$ transition is

expected has an energy of 701.5 keV. The transitions of energies 237.5, 322.5 and 401.6 keV appear to form a rotational band similar to those built on 2^+ states in ^{186,188}Pb isotopes. They are therefore assigned as the $(4^+) \rightarrow (2^+)$, $(6^+) \rightarrow (4^+)$ and $(8^+) \rightarrow (6^+)$ transitions, respectively. The relative intensities of the transitions are shown in Table 4.3.

Table 4.3 Properties of γ-ray transitions of ^{184}Pb.

E_γ(keV)	Nucleus	Intensity	I^π_i	I^π_f
701.5(5)	^{184}Pb	100(14)	(2^+)	(0^+)
237.5(5)	^{184}Pb	92(10)	(4^+)	(2^+)
322.5(5)	^{184}Pb	69(9)	(6^+)	(4^+)
401.6(5)	^{184}Pb	55(9)	(8^+)	(6^+)

*The intensities are normalised to the 702 keV transition.

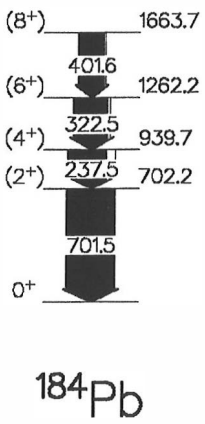

Figure 4.15 Level scheme of ^{184}Pb deduced from the present data.

4.2.2 Nucleus ^{182}Pb

The ^{144}Sm(^{42}Ca,4n) fusion evaporation channel was used to populate excited states of ^{182}Pb. The excitation function for ^{182}Pb was measured with beam energy in the centre of the target ranging from 203 MeV to 213 MeV. The optimum production yield was obtained using the beam energy of 209 MeV. Targets consisting of either one or two 500 μg/cm^2 self-supporting metallic ^{144}Sm foils of 92.4% enrichment were used. Prompt γ rays were detected by the Jurosphere II array.

Prompt γ rays emitted by ^{182}Pb were selected using the RDT technique. Roughly 140 hours of effective beam time yielded about 3500 ^{182}Pb recorded α-decays. Alpha particle energy spectrum for the ^{42}Ca + ^{144}Sm reaction observed within a 170 ms time interval after the detection of a recoil at the same position in the Si strip detector is shown in Figure 4.16. A weak α-particle energy peak of 6874 keV originating from ^{183}Pb lies on the low-energy side of the ^{182}Pb peak. The half-life of ^{183}Pb is five times longer than that of ^{182}Pb. The contribution of this contaminant to the recoil-decay tagged γ-ray spectrum is insignificant both due to the small α-decay branch of 2.5% and the longer half-life [Tot89]. The estimated cross-section for the reaction ^{144}Sm(^{42}Ca,4n)^{182}Pb is deduced to be about 300 nb. Using the method described in [Lei81] the half-life of ^{182}Pb was determined to be $t_{1/2}$ = 64(7) ms, which is consistent with the earlier value of $t_{1/2}$ = 55(5) ms measured in ref. [Tot99].

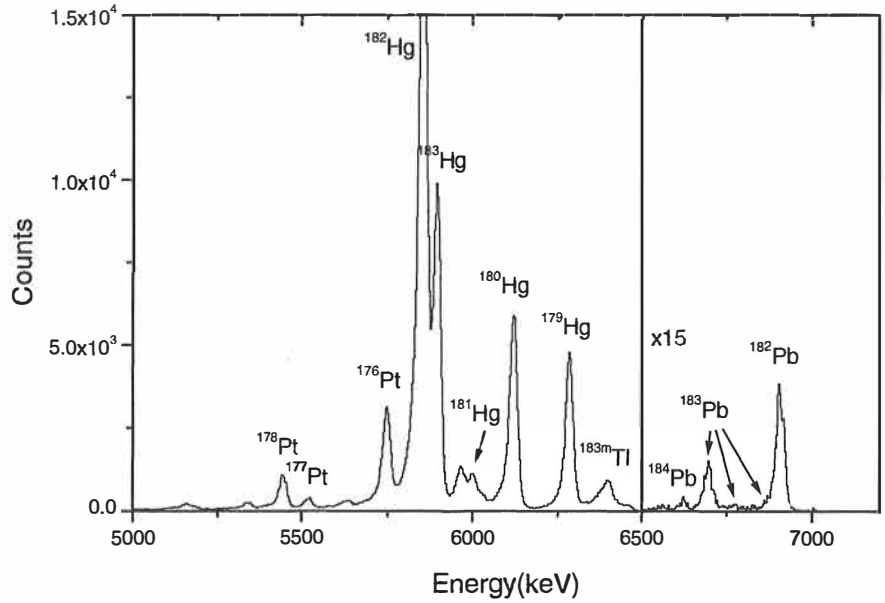

Figure 4.16 Energy spectrum of α particles from ^{42}Ca + ^{144}Sm reactions observed within a 170 ms time interval after the detection of a recoil at the same position in the Si strip detector. When creating the spectrum an additional condition that the gas counter signal is not present has been demanded.

The searching time used to generate the recoil-gated α-tagged γ-ray spectrum shown in Figure 4.17 was 170 ms, which is approximately three times the α-decay half-life of ^{182}Pb. Although the cross-section for the ^{144}Sm(^{42}Ca,4n)^{182}Pb reaction is about ten times lower than that of the ^{148}Sm(^{40}Ca,4n)^{184}Pb reaction, the shorter half-life of ^{182}Pb and pure ^{42}Ca beam (see Section 4.2.1) made it possible to generate such a clean γ-ray spectrum. The six lines marked in the spectrum are firmly assigned to originate from ^{182}Pb. The energies of these γ-ray transitions are listed in Table 4.4 with their intensities normalised to the most intensive transition of 888 keV. The proposed level scheme of ^{182}Pb, based on the relative intensity of the transitions and level systematics in Pb, is shown in Figure 4.18. The transitions of energies 231.4, 313.8, 392.3, 462.7 and 523.8 keV obviously form a rotational band similar to those built on 2^+ states in $^{184, 186, 188}$Pb isotopes and, therefore, they are tentatively assigned as E2 transitions.

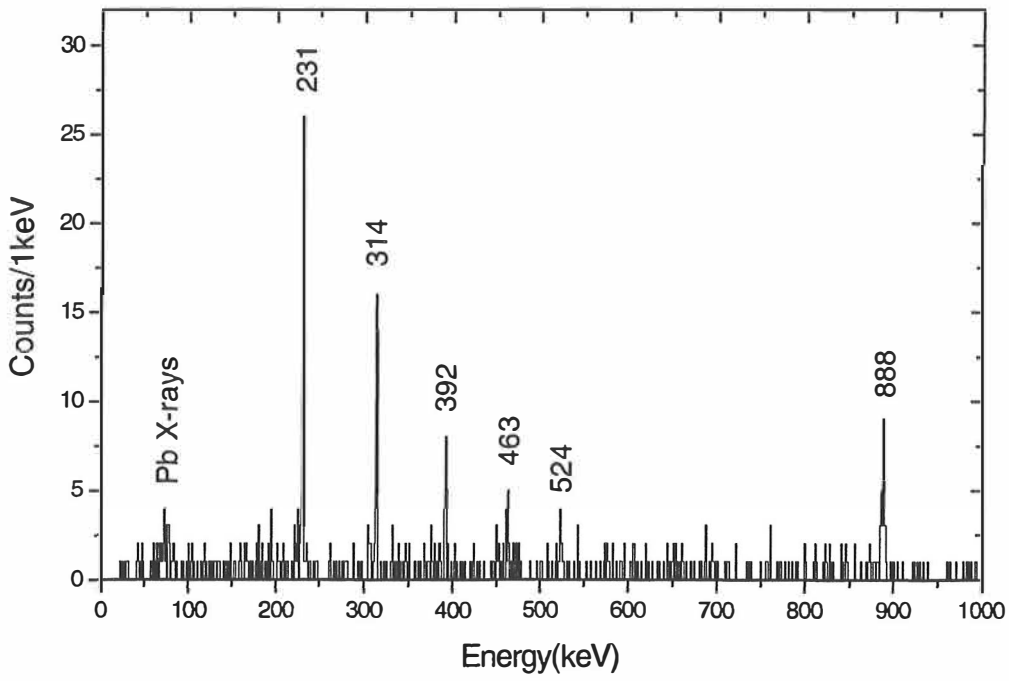

Figure 4.17 Singles γ-ray energy spectrum generated using the RDT technique showing γ-ray transitions in ^{182}Pb and Pb X-rays.

Table 4.4 Properties of γ-ray transitions of ^{182}Pb.

E_γ(keV)	Nucleus	Intensity	I^π_i	I^π_f
888.3(3)	^{182}Pb	100(21)	(2^+)	(0^+)
231.4(3)	^{182}Pb	74(15)	(4^+)	(2^+)
313.8(3)	^{182}Pb	61(14)	(6^+)	(4^+)
392.3(5)	^{182}Pb	30(10)	(8^+)	(6^+)
462.7(5)	^{182}Pb	20(8)	(10^+)	(8^+)
523.8(5)	^{182}Pb	19(8)	(12^+)	(10^+)

*The intensities are normalised to the 888 keV transition.

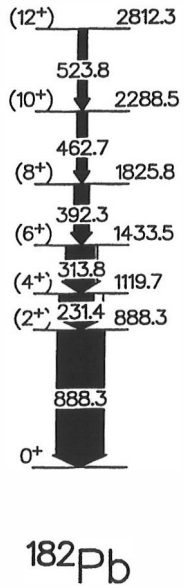

Figure 4.18 Level scheme of ^{182}Pb deduced from the present data.

4.2.3 Discussion

Systematics

Excited states in $^{182, 184}$Pb isotopes identified for the first time in the present work have been included in the systematics of positive parity levels of even-mass Pb nuclei plotted in Figure 4.19. These two nuclei are the first even-even Pb isotopes beyond the $82<N<126$ mid-shell where the γ-ray transitions are known. In the even-even Pb nuclei with $192 \leq A \leq 206$ the excitation energies of the 8^+, 10^+ and 12^+ states marked with filled squares in Figure 4.19 decrease slightly with decreasing neutron number. This behaviour can be understood assuming pure neutron $\nu(i_{13/2})^2$ configuration for these spherical states. The energies of the proposed two-proton $\pi(h_{9/2})^2$ intruder 8^+

state (open circle) and the two-proton $\pi(i_{13/2})^1(h_{9/2})^1$ (open triangle) isomeric intruder 11^- state with moderate oblate deformation [Dra98] decrease more rapidly when going towards more neutron-deficient nuclei. A similar steep down slope in the level systematics of both spherical (filled squares) and supposedly oblate (open circles) 2^+, 4^+ and 6^+ states in Pb nuclei with $N<196$ can be seen. The behaviour of oblate intruder states as a function of the neutron number follows the predictions [Naz93] and is due to the combined effect of the pairing interaction and the proton-neutron interaction (see Chapter 2). The lowering of the energy of the spherical states can be due to the considerable mixing of states with different configurations since the unperturbed energies of the deformed oblate intruder states and the spherical neutron states lie very close to each other.

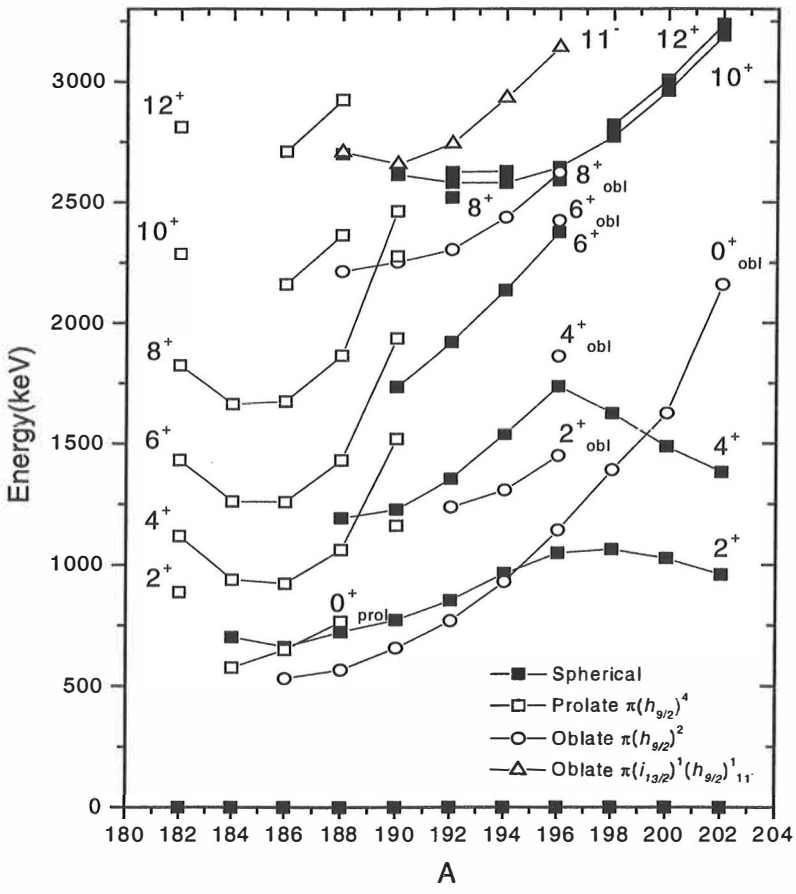

Figure 4.19 Level systematics for the even-mass Pb isotopes taken from references [Hee93, Bax93, Dra99, Dra98, Plo93, Dup87, All98, Fan91, Fen96, Bal94, Fir96] and present work.

A rotational-like band assumed to be based on the prolate 4p-4h intruder structure (open squares) was first observed in ^{188}Pb by Heese et al.[Hee93]. A similar band has also been found in ^{186}Pb [Bax93]. The heaviest Pb isotope where candidates for the prolate intruder states are found is ^{190}Pb [Dra98]. In contrast to the lighter isotopes, in ^{190}Pb the prolate-deformed states are observed to be non-yrast states. The observed energy levels in both ^{182}Pb and ^{184}Pb form a rotational pattern similar to those in the $^{186,\ 188}$Pb nuclei and therefore, they can be regarded as members of the prolate-deformed rotational bands. The excited states in ^{182}Pb lie higher in energy than the corresponding states in the neighbouring isotopes. This confirms the idea of the prolate energy minimum rising fast in energy with decreasing N and lying lowest in energy close to neutron number N=103 as it does in Hg nuclei.

More detailed information of the prolate nature of the excited states in $^{182,\ 184}$Pb can be obtained by studying the aligned angular momentum, i_x, as a function of rotational frequency ($\hbar\omega$) shown for $^{182,\ 184,\ 186,\ 188}$Pb and $^{180,\ 182,\ 184}$Hg in Figure 4.20. The aligned angular momentum is obtained by subtracting the angular momentum of the collective rotation from the total angular momentum. The same variable moment of inertia reference parameters, $J_0=27\hbar^2\text{MeV}^{-1}$ and $J_1=199\hbar^4\text{MeV}^{-3}$, have been used for all seven nuclei. The transition energies of $^{186,\ 188}$Pb and $^{180,\ 182,\ 184}$Hg are taken from ref. [Bax93, Hee93, Dra88, Bin95, Den95]. Above $I=2\hbar$ the alignment properties of the rotational bands in the four Pb isotopes are similar, but not identical. The alignment of the intruder bands increases with decreasing neutron number, indicating a slight increase in collectivity. In the Hg isotones the same trend can be seen although the increase is not so pronounced. Above 0.2 MeV the behaviour of the three Hg isotopes is almost identical to that of ^{186}Pb. The similarities between the Pb and Hg isotopes indicate that the low-lying bands in the Pb isotopes are built on the same prolate-deformed structures as the intruder bands in Hg nuclei.

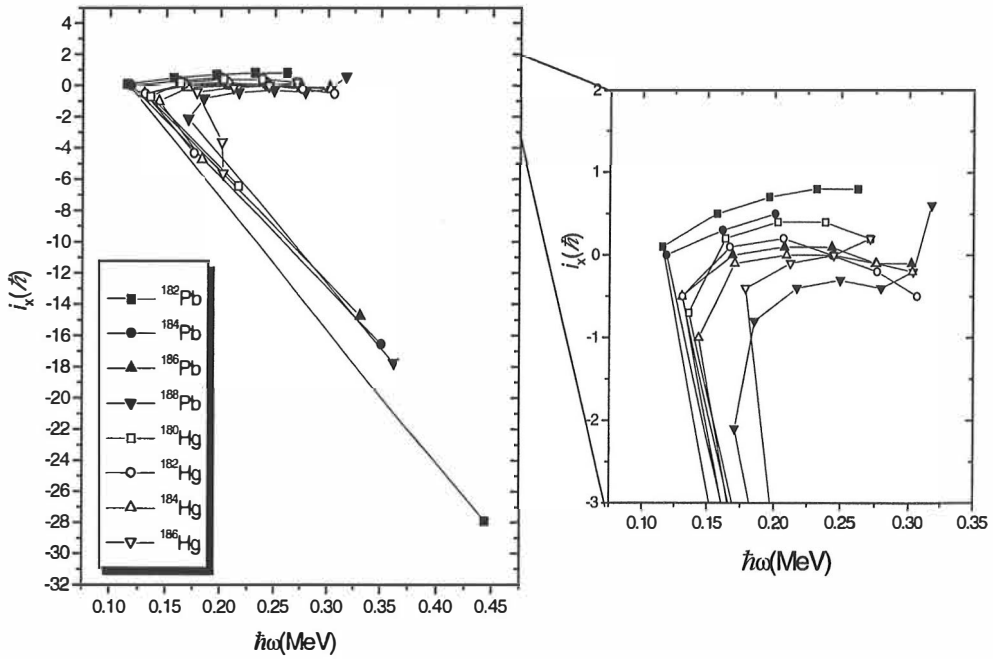

Figure 4.20 Plots of aligned angular momentum, i_x, as a function of rotational frequency, $\hbar\omega$, for ^{182,184}Pb (this work), ^{186,188}Pb [Bax93, Hee93] and ^{180,182,184}Hg [Dra88, Bin95, Den95]. Rotational references with Harris parameters of $J_0=27\hbar^2MeV^{-1}$ and $J_1=199\hbar^4MeV^{-3}$ have been subtracted.

According to the intruder spin model (Chapter 2.1) prolate intruder bands in Pb (4p-4h) and Pt (2p-6h) isotopes should belong to the same intruder spin multiplet , $I^{(i)}=2$ and thus, the level structures of these bands are expected to be similar. Indeed, the level spacings of the prolate bands in the Pb nuclei with $N\leq106$ are observed to be similar to those of the corresponding Pt isotones. As seen from above, the excitation pattern of the prolate 2p-4h intruder states in Hg isotopes also resembles that in Pb nuclei although the states are members of the $I^{(i)}=3/2$ multiplet. In this respect, in the Pb region the intruder spin model seems to fail in explaining the behaviour of the intruder states. However, this discrepancy between the model and the experimental results has been explained by assuming that the prolate bands in Pb isotopes do not have a pure intruder spin but they are rather mixtures of $I^{(i)}=2$ (4p-4h) and $I^{(i)}=3$ (6p-6h) states, that is $I^{(i)}=2.5$. In addition, instead of the 2p-4h structure the prolate bands in Hg nuclei are also assumed be based on 4p-6h structure having $I^{(i)}=2.5$ [Naz93].

Determination of perturbed 0^+ band-head energies

The procedure used in Section 4.1.4 to determine the unperturbed band-head energies in Hg isotopes can be used to extract the band heads of the assumed prolate-deformed bands in $^{182, 184, 186, 188}$Pb isotopes. In Pb nuclei, instead of two low-lying configurations, there are now three configurations (spherical, oblate and prolate) which can mix. In order to compare the band-head energies of $^{182, 184, 186, 188}$Pb isotopes it is important to ascertain the extent to which the low-spin states are perturbed by mixing with other configurations. In reference [All98] the mixing of states of different deformation in ^{188}Pb is discussed. There the spherical configuration has been found to interact very weakly with the oblate and prolate configurations. The mixing matrix elements, deduced to be about 50 keV in both cases, lead to <1% intruder wave function admixtures in the 0p-0h ground state. The oblate and prolate configurations in ^{188}Pb are found to be more strongly mixed. An admixture of 20% for the 0^+ state and the mixing matrix element of approximately 70 keV have been obtained by Allat et al. [All98]. The high-spin members of the prolate band in ^{188}Pb are assumed to be unmixed and, therefore, unperturbed. The band-head energy ($E_u(0)$) can be estimated reliably from these high-spin states.

In ^{186}Pb the oblate and prolate 0^+ states have also been observed to lie close in energy (within 120 keV) [And00], while in ^{184}Pb, a candidate only for the presumed prolate 0^+ state has been seen at the excitation energy of 577(40) keV [And99]. The experimental systematics of oblate 0^+ band heads (see Fig. 4.18) suggests that the oblate 0^+ state can be expected at a similar excitation energy in ^{184}Pb and therefore, the mixing of these states perturbs their positions. Even though the 0^+ states in $^{182, 184}$Pb are mixed the high-spin members of the observed prolate band are assumed to be unmixed and they can be used to estimate the energies of the unperturbed prolate band head. The unperturbed $E_u(0)$ energies were obtained by fitting the formula 4.3 to the known yrast states of these four nuclei. In ^{182}Pb the 2^+ state seems to follow closely the fitted line as shown in Figure 4.21 and, therefore, it is regarded as a part of the prolate-deformed band.

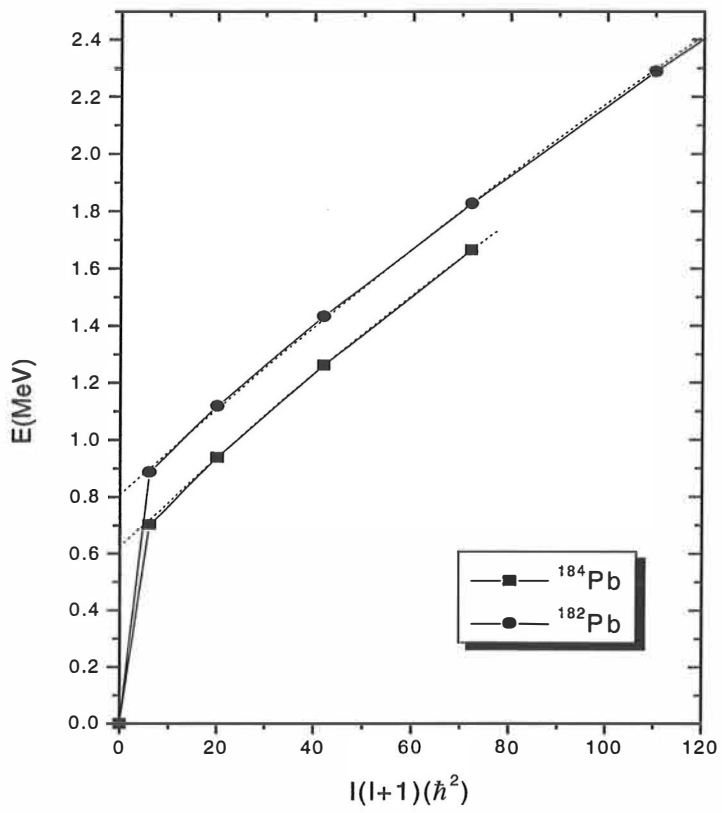

Figure 4.21 A plot of excitation energies as a function of spin for $^{182, 184}$Pb. The extrapolations to zero spin used to determine the $E_{\alpha}(0)$ values are marked with the dashed lines.

By fitting the formula to the states from I=2 to 12 for ^{182}Pb, I=4 to 8 for ^{184}Pb, I=4 to 12 for ^{186}Pb and I=4 to 14 for ^{188}Pb values of 810(12), 625(16), 621(12) and 760(20) keV for the unperturbed prolate band-head energies were extracted, respectively. The extrapolated energies of the prolate 0^+ states in $^{186, 188}$Pb are close to the measured (perturbed) 0^+ -state energies of 650 [And00] and 767 keV [All98]. In both ^{184}Pb and ^{186}Pb the excited 0^+ states are mixed and thus, it is difficult to determine the point where the prolate and oblate bands minimise their energies from the measured 0^+ energies. However, from the systematic behaviour of the extrapolated unperturbed band-head energies plotted in Figure 4.22 it can be seen that the excitation energy of the prolate-deformed configuration clearly has a minimum close to N=103 as it does also in Hg nuclei.

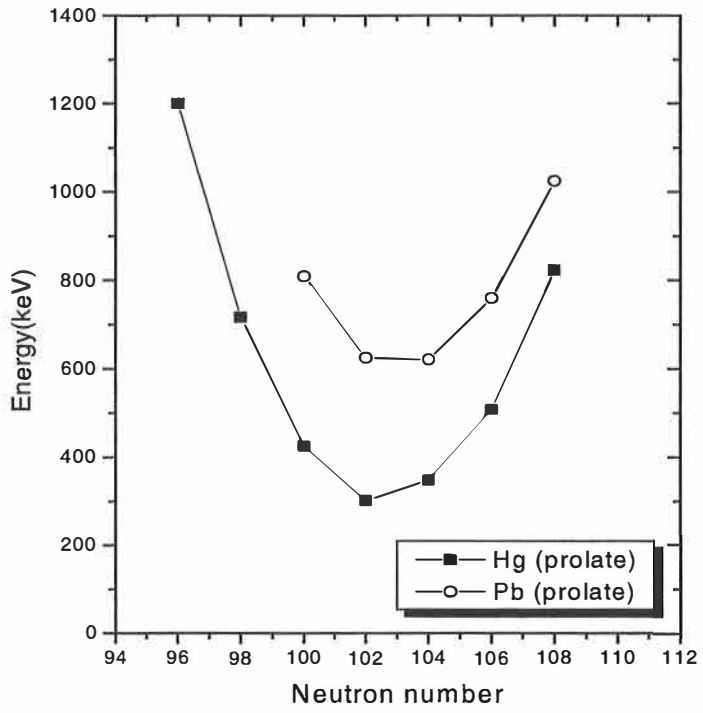

Figure 4.22 The extrapolated unperturbed band head energies of Hg and Pb isotopes. The levels of Hg (Pb) isotopes are marked with filled squares (open circles).

4.3. Odd-mass nucleus ^{183}Tl

In odd-mass Tl isotopes the discovery of 1p-2h intruder states and shape coexistence was connected to the observation of low-lying 9/2$^-$ isomeric states in the $^{193-199}_{81}$Tl isotopes [Dia63]. The structure of these isomeric states was confirmed later in an in-beam spectroscopy measurement, where a band of high-spin states was observed to be built on the 9/2$^-$ isomer in ^{199}Tl. This was suggested to be due to the odd proton occupying the $h_{9/2}$ intruder orbital and thus, giving rise to an oblate shape [New70]. Later rotational bands associated with both oblate and prolate shapes have been observed in lighter isotopes [Lan95]. The band head of the oblate $h_{9/2}$ (1p-2h) intruder band has been observed to lie lowest in energy near N=108. On the contrary, the band head of the prolate intruder band assumed to be based on the $\pi(i_{13/2})^1$ structure has been predicted to continue its dropping in excitation energy when passing the neutron

mid-shell. This prolate structure is formed presumably by coupling the odd $i_{13/2}$ proton to the prolate Hg core of the 4p-6h structure [Lan95].

By studying an odd-mass nucleus information about the orbits, which are responsible for the structure of the neighbouring even-even nuclei, can be obtained. For instance, the close similarity between the level energies of the supposedly prolate band in ^{188}Hg and the prolate band based on the $i_{13/2}$ structure in ^{189}Tl implies that the $i_{13/2}$ proton in ^{189}Tl acts as a spectator without disturbing the ^{188}Hg core. This indicates that the occupation probability of the $i_{13/2}$ prolate Nilsson orbits is small in the wave function of the prolate minimum of the core [Por91]. The calculations in reference [Lan95] also support the idea that the prolate states based on the 4p-6h and 5p-6h structures in Hg and Tl isotopes, respectively are predominantly caused by occupation of the $h_{9/2}$ and $f_{7/2}$ proton orbits.

Recently, in ^{183}Tl a rotational-like yrast cascade associated with the prolate structure was established [Rev00]. However, a linking γ-ray transition from the yrast band down to a lower lying oblate deformed structure was not observed and, thus, the band-head energy of the yrast band remained unclear. In the present work this "missing" transition has been observed.

4.3.1 Experimental results

The ^{183}Tl isotope was produced via the ^{144}Sm(^{42}Ca, 1p2n) reaction channel in the measurement where the main goal was to study the ^{182}Pb nucleus (see Section 4.2.2). Although the total α decay branch of the 9/2$^-$ level in ^{183}Tl is small (b_α~1.5% [Rev00], $t_{1/2}$=60 ms [Sch80]) the RDT analysis was carried out. The 6.343 (I_α~84%) and 6.378 MeV (I_α~16%) [Sch80] α-particle energy peaks were used in the tagging procedure. In Figure 4.23 the energy spectra of recoil gated α tagged delayed a) and prompt b) γ rays are shown. The energies of the observed 160.1, 260.1, 355.0, 439.4 and 514.6 keV peaks are in accordance with the band observed in the recent recoil-mass selected γ-ray spectroscopic measurement [Rev00]. These γ rays are also established to be in coincidence with each other, as indicated in Figure 4.23 c), which shows the γ-ray spectrum obtained by gating on the 160 keV transition.

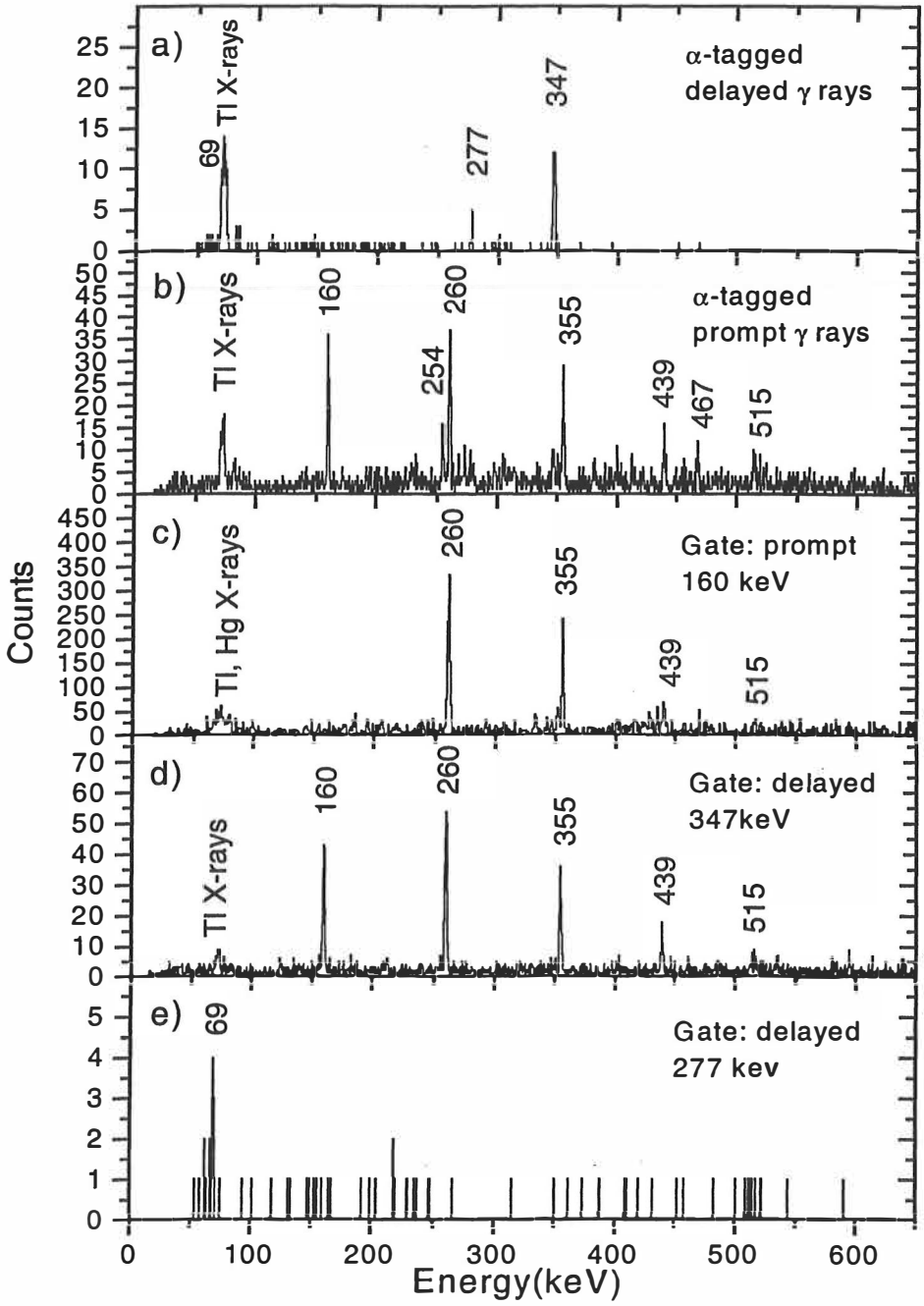

Figure 4.23 Energy spectra of a) delayed and b) prompt γ rays generated by gating with recoils and tagging with ^{183}Tl α-decays. Energy spectra of prompt γ rays obtained by gating on c) the prompt 160 keV γ-ray transition and d) the delayed 347 keV γ-ray transition. e) Spectrum showing the γ rays observed at the focal plane in coincidence with the 277 keV transition.

The intensity ratio of γ rays observed by the Ge detectors at 134° and 158° to those observed by the 79° and 101° Ge detectors for the known E2 transitions in ^{182}Hg and the 160.1 and 439.4 keV transitions in ^{183}Tl (see Table 4.5) were extracted from the recoil-gated spectra. It was not possible to determine the ratios of the other transitions in ^{183}Tl due to the overlapping ^{182}Hg γ-ray energy peaks. The ratios for the 160.1 and 439.4 keV transitions are within the error bars similar to those of the ^{182}Hg E2 transitions, thus confirming their E2 character. Consequently, taking into account internal conversion the observed γ-ray transitions form a rotational-like E2 cascade, which resembles the yrast $\pi i_{13/2}$ cascades observed in heavier odd-mass isotopes [Lan95]. On the basis of the intensity considerations, the 160.1 keV E2 transition is placed at the bottom of the band. Unlike in the heavier isotopes the tentatively assigned $\pi i_{13/2}$ band in ^{183}Tl seems to be populated down to the $(13/2^+)$ band head. The deduced level scheme is shown in Figure 4.25. The 254 and 467 keV transitions are assigned to ^{183}Tl, but their placements in the level scheme are unclear. The 467 keV transition is a good candidate for the $11/2^- \rightarrow 9/2^-$ transition seen in the heavier odd-mass Tl isotopes as the strongest transition feeding the oblate isomeric state.

In the delayed γ-ray spectrum of Figure 4.23 a) two clear peaks of 277 and 347 keV can be seen in addition to the Tl X-rays. On the low-energy side of the Tl X-rays a γ-ray energy peak of about 69 keV is also visible. When gating on the delayed 347 keV transition the energy spectrum of prompt γ rays shown in Figure 4.23 d) can be obtained. In that spectrum all the above mentioned transitions of the yrast band are seen. Therefore, the 347 keV transition is regarded as an M2 linking transition from the tentatively assigned $(13/2^+)$ isomeric state to the $9/2^-$ state. The half-life of the isomeric state has been determined by fitting a decay curve to the spectrum of the time difference between the implantation of a recoil and the detection of a 347 keV γ-ray in the Ge detectors at the RITU focal plane. In practice, the recoil signal is delayed by 30 μs and used as the stop signal for the TAC, which leads to reversed time order in the time difference spectrum shown in Figure 4.24. The extracted half-life of $t_{1/2}$=1.48(10) μs corresponds to a transition strength of B(M2)=0.059(10) W.u calculated by taking into account the 347 keV γ-ray transition proportion of about 46% of the total de-excitation of the 972 keV level in ^{183}Tl. The transition is hindered by a factor of about 17 over the single-particle Weisskopf estimate. In ^{195}Bi and ^{197}At

nuclei the $13/2^+ \rightarrow 9/2^-$ transitions have been observed to have hindrance factors of the same order of magnitude (~20 and ~45, respectively) [Smi99].

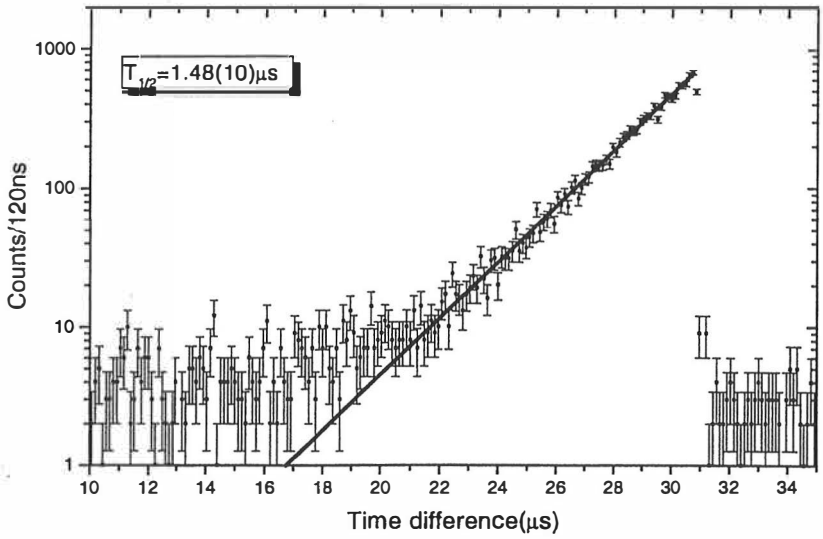

Figure 4.24 Spectrum showing the time difference between the implantation of a recoil and the detection of a 347 keV γ-ray in the Ge detectors at the RITU focal plane.

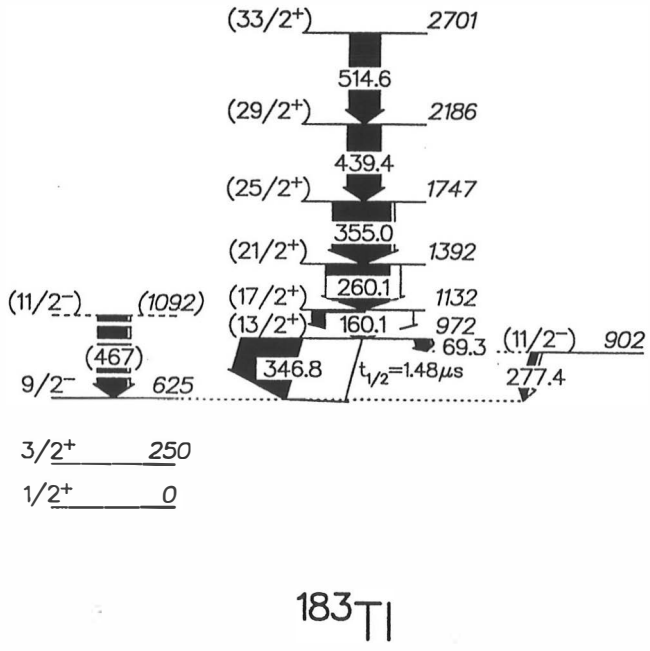

Figure 4.25 Level scheme of ^{183}Tl deduced from the present data. The energies of the $1/2^+$, $3/2^+$ and $9/2^-$ levels have been measured in an α-decay study discussed in ref. [Bat99].

The prompt 160, 260, 355 and 439 keV transitions of the yrast band in ^{183}Tl are also seen when gating on the delayed 277 keV transition. In addition, in the energy spectrum of delayed γ rays obtained by gating on the prompt 160 keV transition both the 277 and 347 keV transitions are visible. Thus, the 277 keV transition also proceeds in the de-excitation of the $(13/2^+)$ isomeric state. In the lowest part of Figure 4.23 an energy spectrum of delayed γ rays in coincidence with the 277 keV transition is shown. There is one peak in the spectrum at the energy of 69 keV, but there is no sign of Tl X-rays of 72.9, 70.8 and 82.6 keV although low energy transitions are usually highly converted. The binding energy of the K electron in Tl nuclei is 85.5 keV and thus, only the L X-rays accompanying the conversion electrons are seen in the case of the 69 keV transition. It is not possible to detect such low energy γ rays using the γ-detector array placed at the focal plane. Therefore no X-rays are observed in coincidence with 277 keV transition. A half-life of $t_{1/2} = 1.3 \pm 4 \mu s$ has been determined from the time difference between the implantation of a recoil and the detection of a 69 keV γ-ray. Within error bars this is in accordance with the value obtained above by using the 347 keV transition. If assuming E1 and M1 character for the 69 and 277 keV transitions, respectively and taking into account the electron conversion the intensities of these transitions in the α-tagged spectrum of the delayed γ rays are equal within the errors. These facts together with the fast coincidence relationship and energy sum information support the assumption that the 69 keV and 277 keV transitions are the $(13/2^+) \rightarrow (11/2^-)$ and $(11/2^-) \rightarrow (9/2^-)$ transitions, respectively.

If assuming M2 and M1 multipolarities for the 347 and 277 keV transitions the internal K conversion coefficients for these transitions are about 0.7 and 0.4, respectively. In the recoil-gated α-tagged spectrum of delayed γ rays the number of observed Tl X-rays corresponds within the error bars these coefficients.

Table 4.5 Properties of γ-ray transitions of ^{183}Tl

E_γ(keV)	Nucleus	Intensity*	I^π_i	I^π_f	R_I
160.1(3)	^{183}Tl	100(14)	$(17/2^+)$	$(13/2^+)$	1.06(13)
260.1(3)	^{183}Tl	74(10)	$(21/2^+)$	$(17/2^+)$	
355.0(3)	^{183}Tl	61(9)	$(25/2^+)$	$(21/2^+)$	
439.4(5)	^{183}Tl	33(7)	$(29/2^+)$	$(25/2^+)$	1.21(23)
514.6(5)	^{183}Tl	30(7)	$(33/2^+)$	$(29/2^+)$	
467.5(5)	^{183}Tl	30(8)			
254.1(5)	^{183}Tl	17(7)			
346.6(3)	^{183}Tl	114(19)	$(13/2^+)$	$(9/2^-)$	
277.4(5)	^{183}Tl	10(4)	$(11/2^-)$	$(9/2^-)$	
69.3(5)	^{183}Tl	20(8)	$(13/2^+)$	$(11/2^-)$	
352	^{182}Hg		2^+	0^+	1.11(4)
414	^{182}Hg		8^+	6^+	1.26(9)

*The intensities are corrected for the internal conversion and normalised to the 160 keV transition.

4.3.2 Discussion

The systematic behaviour of observed and extrapolated band-head energies in odd-mass Tl isotopes with $96 \leq N \leq 120$ is plotted in Figure 4.26 a). The two lowest levels of most of these isotopes are the $1/2^+$ (filled circles) and $3/2^+$ (open circles) levels based on the $\pi(s_{1/2})^1$ and $\pi(d_{3/2})^{-1}$ structure, respectively. Near the neutron number N=108 the $9/2^-$ level (filled triangles), the band head of the oblate (1p-2h) $\pi(h_{9/2})^1$ intruder band, comes steeply down in energy and it even becomes the second lowest level in Tl isotopes with N=108,110. Both the $9/2^-$ and $11/2^-$ levels of this oblate $\pi h_{9/2}$ band are plotted. The 1092 keV level, tentatively assigned to $11/2^-$ in the present work, has been added to the plot. It follows nicely the systematic trend of the $11/2^-$ members of the oblate band. The band-head energies of the presumed oblate and prolate $\pi i_{13/2}$ intruder bands are marked with open and filled squares, respectively. The prolate band heads for $^{185\text{-}189}$Tl represent extrapolated values based on VMI fits of the $i_{13/2}$ band and they have been taken from ref. [Lan95]. The band head of ^{183}Tl has been determined in the present work. In $^{193\text{-}201}$Tl the $11/2^-$ level (asterisks) based on the $\pi(h_{11/2})^{-1}$ structure can be seen at the energy of about 1400 keV [Hey83 and references therein]. This $\pi(h_{11/2})^{-1}$ structure is supposedly formed when a $h_{11/2}$ proton hole is weakly coupled to the spherical Pb core. In ^{187}Tl a $11/2^-$ band-head tentatively assigned to a weakly prolate-deformed $\pi(h_{11/2})^{-1}$ band has been observed to lie at the energy of 952 keV [Lan95]. In addition, the high spin isomer in ^{177,179}Tl has been assigned as the

$\pi(h_{11/2})^{-1}$ configuration rather than the $\pi(h_{9/2})^{1}$ configuration seen in the heavier isotopes [Pol99, Tot98]. The lowering in the excitation energy of the $11/2^-$ states as a function of neutron number can be explained by assuming that the odd proton is coupled to the prolate Pb core instead of the spherical one. The systematic behaviour of the $11/2^-$ levels supports the assumption that the 902 keV level, tentatively assigned in the present work, is the band-head of the $\pi(h_{11/2})^{-1}$ band.

In Figure 4.26 b) the experimentally obtained band-head energies of the oblate $\pi h_{9/2}$ and prolate $\pi i_{13/2}$ bands are plotted together with the energies of the excited 0^+ states in Hg and Pb isotopes. The observed 0^+ states in Pb isotopes based on the oblate structure have been marked with open triangles. The band-head energies of the oblate $\pi h_{9/2}$ bands in the Tl nuclei with $108 \leq N \leq 114$ are approximately half of the excitation energies of the oblate 0^+ states in the corresponding Pb isotones. This is in accordance with the discussions presented in Chapter 2.1. The excited 0^+ states in Hg and Pb nuclei assumed to have the prolate shape are marked with open squares and asterisks, respectively and they have been obtained using the extrapolation procedure described in Section 4.1.4. Near the N=103 the prolate intruder bands in Hg and Pb nuclei reach their minimum energies as already pointed out in Sections 4.1.4 and 4.2.3. As a function of the neutron number, the band-head energy of the prolate $\pi i_{13/2}$ band in Tl isotopes with $N \leq 108$ follows the trend seen in the corresponding Hg isotones. Therefore, if assuming the 4p-6h configuration for the prolate bands in the Hg nuclei [Naz93, Lan95], the prolate $\pi i_{13/2}$ bands in the Tl nuclei are likely to be based on the 5p-6h structure. In the Tl nuclei the single $i_{13/2}$ proton seems to act as a spectator without disturbing the prolate structure of the Hg core. Thus, the occupation probability of the $i_{13/2}$ prolate orbits is small in the wave function of the prolate minimum of the core as already noted in reference [Por91]. The question whether the band-head of this $\pi i_{13/2}$ prolate band in odd-mass Tl isotopes continues to drop in excitation energy when going towards the more neutron-deficient side still remains open. In the neighbouring odd-mass Au isotopes the $\pi i_{13/2}$ prolate band (filled diamonds in Figure 4.26 b)) does not seem to reach the minimum energy above N=100 although the calculations [Mue99] predict that the energy of this configuration should lie lowest at N=102. In reference [Lan95] the prolate states in odd-mass Tl isotopes are predicted to continue to drop in energy when passing the mid-shell, while

the calculations presented in reference [Rev94] show a rise in excitation energy at N≤104. In this respect, it would be of interest to probe the level structure of the ^{181}Tl isotope.

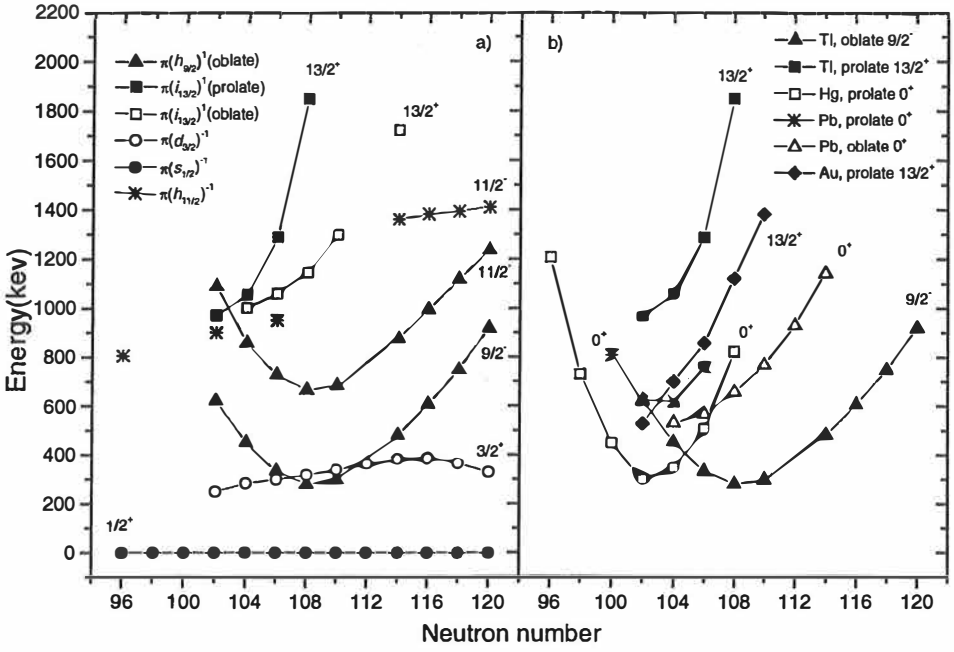

Figure 4.26 Comparison of experimentally obtained band-head energies of a) odd-mass Tl isotopes b) oblate and prolate deformed bands in Au, Hg, Tl and Pb isotopes. The data have been taken from Refs. [Rev00, Lan95, Por91, Bat99, Ket99, Wau97, Mue99, Lar86, Tot98, Fir96, Pol99, Hey83] and the present work.

5. Summary

In the present work the power of the Recoil-Decay-Tagging method has been demonstrated in the study of very neutron-deficient nuclei near the Z=82 shell closure. In order to be able to utilise this method Jurosphere and Jurosphere II γ-ray detector arrays have been installed in conjunction with the gas-filled recoil separator RITU at JYFL. Via in-beam γ-ray spectroscopic studies it has been possible to extent the knowledge of the coexisting structures in the neutron-deficient Hg, Tl and Pb nuclei beyond the 82<N<126 neutron mid-shell.

In this work the ^{176}Hg and ^{174}Hg nuclei have been studied utilising the RDT technique. In ^{176}Hg yrast states up to I=10$\hbar$ have been observed. The deduced yrast sequence of γ-ray transitions can be associated with a near-spherical ground state band crossed at I=6$\hbar$ by a prolate intruder band similar to those seen at much lower excitation energies in Hg isotopes near the neutron mid-shell. In the present work γ rays originating from the ^{174}Hg isotope have been observed for the first time. The energies of the tentatively assigned excited 2^+ and 4^+ states in ^{174}Hg are higher than in any other Hg isotope except the closed-shell nucleus $^{206}Hg_{126}$. The new data supports the theoretical calculations by Nazarewicz [Naz93] which predict that the ground state in even-even Hg nuclei should evolve from the oblate shape towards a spherical shape with decreasing neutron number. The near-constant level spacings between the lowest excited states both in ^{176}Hg and ^{174}Hg can also be a sign of the change towards vibrational structures.

The RDT method has also been employed in studies of the very neutron-deficient ^{184}Pb and ^{182}Pb nuclei. In these nuclei the γ-ray transitions have been identified for the first time. Low-lying rotational bands similar to those seen in the heavier ^{186,188}Pb isotopes and Hg isotones have been observed in both nuclei. These bands can be associated with a prolate-deformed structure. The extrapolated unperturbed band-head energies for the presumable prolate-deformed rotational bands in Pb and Hg isotopes with 100≤N≤108 and 96≤N≤108, respectively reveal that the prolate-deformed states minimise their energies near the neutron mid-shell as predicted by both the spherical [Hey83] and deformed [Naz93] shell-model calculations.

In the present work the band-head energy of the yrast band in ^{183}Tl has also been determined. As a function of neutron number, the band-head energy of this prolate $\pi i_{13/2}$ band in odd-mass Tl isotopes with $N \leq 108$ follows approximately the trend seen in the energies of the prolate intruder 0^+ states in the corresponding Hg isotones. Thus, the single $i_{13/2}$ proton in these Tl nuclei seems to be coupled to the prolate-deformed Hg core without disturbing the structure of the core. However, the question whether the band head continues to drop in excitation energy when going towards more neutron-deficient side still remains open.

Utilising the RDT method a considerable amount of valuable information about the structure of the neutron-deficient nuclei near the $Z = 82$ shell gap has been obtained. With further developments it is possible to extent the region of the nuclei studied using this technique. The identification of prompt emission by β-γ tagging and β-delayed proton emission can be used to probe the nuclei near the proton drip line with $A < 150$. This can be realised for example by using highly granulated Si and Ge detectors to detect X-rays and β-particles. By using a box-like Si detector to surround the Si strip detector the observation of conversion electrons is possible. In this way the focal plane spectrometers will be capable of detecting most of the decay processes of the separated reaction products. This work shows the capabilities of the current system when probing the structure of nuclei decaying via α-particle emission.

References

[All98] R.G. Allatt, R.D. Page, M. Leino, T. Enqvist, K. Eskola, P.T. Greenlees, P. Jones, R. Julin, P. Kuusiniemi, W.H. Trzaska and J. Uusitalo,
Phys. Lett. B **437**, 29 (1998)

[And99] A.N. Andreyev, D. Ackermann, P. Cagarda, J. Gerl, F. Heβberger, S. Hofmann, M. Huyse, A. Keenan, H. Kettunen, A. Kleinböhl, A. Lavrentiev, M. Leino, B. Lommel, M. Matos, G. Münzenberg, C. Moore, D.C. O'Leary, R.D. Page, S. Reshitko, S. Saro, C. Schlegel, H. Schaffner, M. Taylor, P. Van Duppen, L. Weissman and R. Wyss,
Eur. Phys. J. A **6**, 381 (1999)

[And00] A.N. Andreyev, M. Huyse, P. Van Duppen, L. Weissman D. Ackermann, J. Gerl, F. Heβberger, S. Hofmann, A. Kleinböhl, G. Münzenberg, S. Reshitko, C. Schlegel, H. Schaffner, P. Cagarda, M. Matos, S. Saro, A. Keenan, C. Moore, D.C. O'Leary, R.D. Page, M. Taylor, H. Kettunen, M. Leino, A. Lavrentiev, B. Lommel, R. Wyss and K. Heyde
Nature, **405**, 430 (2000)

[Arm71] P. Armburuster, J. Eidens, J.W. Grüter, H. Lawin, E. Roeckl and K. Sistemich,
Nucl. Instr. and Meth. **91**, 499 (1971)

[Bal94] G. Baldsiefen, H. Hübel, W. Korten, D. Mehta, N. Nenoff, B.H. Thirumala Rao, P. Willsau, H. Grawe, J. Heese, H. Kluge, K.H. Maier, R. Schubart, S. Frauendorf and H.J. Maier,
Nucl. Phys. **A574**, 521 (1994)

[Bat99] J.C. Batchelder, K.S. Toth, C.R. Bingham, L.T. Brown, L.F. Conticchio, C.N. Davids, R.J. Irvine, D. Seweryniak, W.B. Walters, J. Wauters, E.F. Zganjar, J.L. Wood, C. DeCoster, B. Decroix and K. Heyde,
Eur. Phys. J A **5**, 49 (1999)

[Bax93] A.M. Baxter, A.P. Byrne, G.D. Dracoilis, R.V.F. Janssens, I.G. Bearden, R.G. Henry, D. Nisius, C.N. Davids, T.L. Khoo, T. Lauritsen, H. Penttilä, D.J. Henderson and M.P. Carpenter,
Phys. Rev. C **48**, 2140 (1993)

[Bea92] C.W. Beausang, S.A. Forbes, P. Fallon, P.J. Nolan, P.J. Twin, J.N. Mo, J.C. Lisle, M.A. Bentley, J. Simpson, F.A. Beck, D. Curien, G. deFrance, G. Duchêne, and D. Popescu,
Nucl. Instr. and Meth. A **313**, 37 (1992)

[Ben87] R. Bengtsson, T. Bengtsson, J. Dudek, G. Leander, W. Nazarewicz and J. Zhang,
Phys. Lett. B **183**, 1 (1987)

[Ben89] R. Bengtsson and W. Nazarewicz,
Z. Phys. A **334**, 269 (1989)

[Bij96] N. Bijnens, I. Ahmad, A.A. Andreyev, J.C. Batchelder, C.R. Bingham, D. Blumenthal, B.C. Busse, X.S. Chen, L.F. Conticchio, C.N. Davids, M .Huyse, R.V.F. Janssens, P. Mantica, H .Penttilä, W. Reviol, D. Severyniak, P. Van Duppen, W.B. Walters and B.E. Zimmerman,
Z. Phys. A **356**, 3 (1996)

[Bin95] K.S. Bindra, P.F. Hua, B.R.S. Babu, C. Baktash, J. Barreto, D.M. Cullen, C.N. Davids, J.K. Deng, J.D. Garrett, M.L. Halbert, J.H. Hamilton, N.R. Johnson, A. Kirov, J. Kormicki, I.Y. Lee, W.C. Ma, F.K. McCowan, A.V. Ramayya, D.G. Sarantites, F. Soramel and D. Winchell,
Phys. Rev. C **51**, 401 (1995)

[Boh41] N. Bohr,
Phys. Rev. **59**, 270 (1941)

[Bon76] J. Bonn, G. Huber, H.-J. Kluge and E.W. Otten,
Z. Phys. A **276**, 203 (1976)

[Car90] M.P. Carpenter, C.R. Bingham, L.H. Courtney, V.P. Janzen, A.J. Larabee, Z.-M. Liu, L.L. Riedinger, W. Schmitz, R. Bengtsson, T. Bengtsson, W. Nazarewicz, J.-Y. Zhang, J.K. Johansson, D.G. Popescu, J.C. Waddington, C. Baktash, M.L. Halbert, N.R. Johnson, I.Y. Lee, Y.S. Schutz, J. Nyberg, A. Johnson, R. Wyss, J. Dubuc, G. Kajrys, S. Monaro, S. Pilotte, K. Honkanen, D.G. Sarantites and D.R. Haenni,
Nucl. Phys. **A513**, 125 (1990)

[Car97] M.P. Carpenter, R.V.F. Janssens, H. Amro, D.J. Blumenthal, L.T. Brown, D. Seweryniak, P.J. Woods, D. Ackermann, I. Ahmad, C. Davids, S.M. Fischer, G. Hackman, J.H. Hamilton, T.L. Khoo, T. Lauritsen, C.J. Lister, D. Nisius, A.V. Ramayya, W. Reviol, J. Schwartz, J. Simpson and J. Wauters,
Phys. Rev. Lett. **78**, 3650 (1997)

[Ced90] B. Cederwall, R. Wyss, A.Johnson, J. Nyberg, B. Fant, R. Chapman, D. Clarke, F. Khazaie, J.C. Lisle, J.N. Mo, J. Simpson and I. Thorslund,
Z. Phys. A **337**, 283 (1990)

[Ced98] B. Cederwall, T. Bäck, R. Bark, S. Törmänen, S. Ødegård, S.L. King, J. Simpson, R. D. Page, N. Amzal, D.M. Cullen, P.T. Greenlees, A. Keenan, R. Lemmon, J.F.C. Cocks, K. Helariutta, P. Jones, R. Julin, S.

Juutinen, H. Kankaanpää, H. Kettunen, P. Kuusiniemi, M. Leino, M. Muikku, P. Rahkila, A.Savelius, J. Uusitalo, P. Magierski and R. Wyss
Phys. Lett. B **443**, 69 (1998)

[Coh58] B.L. Cohen and C.B. Fulmer,
Nucl. Phys. **6**, 547 (1958)

[Cos00] C. De Coster, B. Decroix and K. Heyde,
Phys. Rev. C **61**, 067306 (2000)

[Cre91] J. Cresswell,
Eurogam project documentation, EDOC073, Nuclear Structure Software Support Group, Liverpool University, February 1991

[Dia63] R.M. Diamond and F.S. Stephens,
Nucl. Phys. **45**, 632 (1963)

[Den95] J.K. Deng, W.C. Ma, J.H. Hamilton, A.V. Ramayya, J. Kormicki, W.B. Gao, X. Zhao, D.T. Shi, I.Y. Lee, J.D. Garrett, N.R. Johnson, D. Winchell, M. Halbert and C. Baktash,
Phys. Rev. C **52**, 595 (1995)

[Dra82] G.D. Dracoulis, C. Fahlander and M.P. Fewell,
Nucl. Phys. **A383**, 119 (1982)

[Dra86] G.D. Dracoulis, A.E. Stuchbery, A.P. Byrne, A.R. Poletti, S.J. Poletti, J. Gerl and R.A. Bark,
J. Phys. G **12**, L97 (1986)

[Dra88] G.D. Dracoulis, A.E. Stuchbery, A.O. Macchiavelli, C.W. Beausang, J. Burde, M.A. Deplanque, R.M. Diamond and F.S. Stephens,
Phys. Lett. B **208**, 365 (1988)

[Dra91] G.D. Dracoulis, B. Fabricius, A.E. Stuchbery, A.O. Macchiavelli, W. Korten, F. Azaiez, E. Rubel, M.A. Deplanque, R.M. Diamond and F.S. Stephens,
Phys. Rev. C **44**, 1246 (1991)

[Dra94] G.D. Dracoulis,
Phys. Rev. C **49**, 3324 (1994)

[Dra98] G.D. Dracoulis, A.P. Byrne and A.M. Baxter,
Phys. Lett. B **432**, 37 (1998)

[Dra99] G.D. Dracoulis, A.P. Byrne, A.M. Baxter, P.M. Davidson, T. Kibédi, T.R. McGoram, R.A. Bark and S.M. Mullins,
Phys. Rev. C **60**, 014303 (1999)

[Dup84] P. Van Duppen, E. Coenen, K. Deneffe, M. Huyse, K. Heyde and P. Van Isacker,
Phys. Rev. Lett. **52**, 1974 (1984)

[Dup87] P. Van Duppen, E. Coenen, K. Deneffe, M. Huyse and J.L Wood,
Phys. Rev. C **35**, 1861 (1987)

[Fan91] B. Fant, R.J. Tanner, P.A. Butler, A.N. James, G.D. jones, R.J. Poynter, C.A. White, K.L. Ying, D.J.G. Love, J. Simpson and K.A. Connell,
J. Phys. G **17**, 319 (1991)

[Fir96] R.B. Firestone, V.S. Shirley, C.M. Baglin, S.Y. Frank Chu and J. Zipkin,
Table of Isotopes, 8th ed. Vol. II, John Wiley & sons, Inc. 1996 New York

[Fot96] N. Fotiades, S. Harissopulos, C.A. Kalfas,S. Kossionides, C.T. Papadopoulos, R. Vlastou, M. Serris, J.F. Sharpey-Schafer, M. J. Joyce, C.W. Beausang, P.J. Dagnall, P.D. Forsyth, S.J. Gale, P.M. Jones, E.S. Paul, P.J. Twin, J. Simpson, D.M. Cullen, P. Fallon, M.A. Riley, R.M. Clark, K. Hauschild and R. Wadsworth,
Z. Phys. A **354**, 169 (1996)

[Fra75] S. Frauendorf and V.V. Pashkevich,
Phys. Lett. **55B**, 365 (1975)

[Ghi88] A. Ghiorso, S. Yashita, M.E. Leino, L. Frank, J. Kalnins, P. Armbruster, J.-P. Dufour and P.K. Lemmertz,
Nucl. Instr. and Meth. A **269**, 192 (1988)

[Gut83] M. Guttormsen, K.P. Blume, Y.K. Agarwal, A.V. Grumbkow, K. Hardt, H. Hübel, J. Recht and P. Schüler
Z. Phys. A **312**, 155 (1983)

[Han88] F. Hannachi, G. Bastin, M.G. Porquet, C. Schück, J.P. Thibaud, C. Bourgeois, L. Hildingsson, D. Jerrestam, N. Perrin, H. Sergolle, F.A. Beck, T. Byrski, J.C. Merdinger and J. Dudek,
Nucl. Phys. **A481**, 135 (1988)

[Han88a] F. Hannachi, G. Bastin, M.G. Porquet, C. Schück, J.P. Thibaud, C. Bourgeois, L. Hildingsson, D. Jerrestam, N. Perrin, H. Sergolle, F.A. Beck, T. Byrski, J.C. Merdinger and J. Dudek,
Z. Phys. A **330**, 15 (1988)

[Heb90] G. Hebbinghaus, T. Kutsarove, W. Gast, A. Krämer-Flecken, R.M. Leider and W. Urban,
Nucl. Phys. **A514**, 225 (1990)

[Hee93] J. Heese, K.H. Maier, H. Grawe, J. Grebosz, H. Kluge, W. Meczynski, M. Schramm, R. Schubart, K. Spohr and J. Styczen,
Phys. Lett. B **302**, 390 (1993)

[Hei95] P. Heikkinen and E. Liukkonen,
14th International Conference on Cyclotrons and Their Applications, Cape Town, October 8-13, 1995

[Hey83] K. Heyde, P. Van Isacker, M. Waroquier, J.L. Wood and R.A. Meyer
Phys. Rep. **102**, 291 (1983)

[Hey87] K.Heyde, J. Jolie, J. Moreau, J. Ryckebusch, M. Waroquier, P. Van Duppen, M .Huyse and J.L. Wood,
Nucl. Phys. **A466**, 189 (1987)

[Hey88] K.Heyde, J. Ryckebusch, M. Waroquier and J.L. Wood,
Nucl. Phys. **A484**, 275 (1988)

[Hey89] K. Heyde, C. De Coster, J. Ryckebusch and M. Waroquier,
Phys. Lett. B **218,** 287 (1989)

[Hey92] K. Heyde, C. De Coster, J. Jolie and J.L. Wood,
Phys. Rev. C **46**, 541 (1992)

[Hey94] K. Heyde, P. Van Isacker and J.L. Wood,
Phys. Rev. C **49**, 559 (1994)

[Hüb86] H. Hübel A.P. Byrne, S. Ogaza, A.E. Stuchbery, G.D. Dracoulis and M Guttormsen,
Nucl. Phys. **A453**, 316 (1986)

[Jon95] P. Jones,
Ph. D. thesis, University of Liverpool, September 1995 (unpublished)

[Jos00] D.T. Joss, S.L. King, R. D. Page, J. Simpson, A. Keenan, N. Amzal, T. Bäck, B. Cederwall, J.F.C. Cocks, D.M. Cullen, P.T. Greenlees, K. Helariutta, P. Jones, R. Julin, S. Juutinen, H. Kankaanpää, H. Kettunen, P. Kuusiniemi, M. Leino, M. Muikku, A. Savelius and J. Uusitalo
To be published

[Kar69] V.A. Karnaukov, L. Rubinkya, G. Terakop'yan, V. Titov and V.A. Chugreev,
JINR-Report No. P13-4454, Dubna (1969)

[Ket99] H. Kettunen, J.F.C. Cocks, A.N. Andreyev, O. Dorvaux, K. Eskola, P.T. Greenlees, K. Helariutta, M. Huyse, P. Jones, R. Julin, S. Juutinen, P. Kuusiniemi, M. Leino, W.H. Trzaska, J. Uusitalo, K. Van de Vel, and P. Van Duppen,
AIP conference proceedings **495**, 125 (1999)

[Kin98] S.L. King, J. Simpson, R. D. Page, N. Amzal, T. Bäck, B. Cederwall, J.F.C. Cocks, D.M. Cullen, P.T. Greenlees, M.K. Harder, K. Helariutta, P. Jones, R. Julin, S. Juutinen, H. Kankaanpää, A. Keenan, H. Kettunen, P. Kuusiniemi, M. Leino, R. Lemmon, M. Muikku, A. Savelius, J. Uusitalo and P. Van Iscker
Phys. Lett. B **443**, 82 (1998)

[Kon00] F.G. Kondev, M.P. Carpenter, R.V.F. Janssens, I. Wiedenhöver, M. Alcorta, P. Bhattacharyya, L.T. Brown, C.N. Davids, S.M. Fischer, T.L. Khoo, T. Lauritsen, C.J. Lister, R. Nouicer, W. Reviol, L.L. Riedinger, D. Seweryniak, S. Siem, A.A. Sonzogni, J. Uusitalo and P.J. Woods,
Phys. Rev. C **61**, 011303(R) (2000)

[Kur92] T. Kuroynagi, S. Mitarai, S. Suematsu, B.J. Min, H. Tomura, J. Mukai, T. Maeda, R. Nakatani, G. Sletten, J. Nyberg and D. Jerrestam
Nucl. Instr. and Meth. A **316**, 289 (1992)

[Lan95] G.J. Lane, G.D. Dracoulis, A.P. Byrne, P.M. Walker, A.M. Baxter, J.A. Sheikh and W. Nazarewicz,
Nucl. Phys. **A586**, 316 (1995)

[Lar86] A.J. Larabee, M.P. Carpenter, L.L. Riedinger, L.H. Courtney, J.C. Waddington, V.P. Janzen, W. Nazarewicz, J.-Y. Zhang, R. Bengtsson and G.A. Leander,
Phys. Lett. **169B**, 21 (1986)

[Laz93] Yu.A. Lazarev et al.,
JINR-Report No. E7-93-274, **2B497**, Dubna 1993

[Lei77] M. Leino
Licentiate Thesis, University of Helsinki, 1977 (unpublished)

[Lei81] M. Leino, S. Yashita and A. Ghiorso,
Phys. Rev. C **24**, 2370 (1981)

[Lei95a] M. Leino, J. Äystö, T. Enqvist, P. Heikkinen, A. Jokinen, M. Nurmia, A. Ostrowski, W.H. Trzaska, J. Uusitalo, K. Eskola, P. Armbruster and V. Ninov,
Nucl. Instr. Meth. B **99**, 653 (1995)

[Lei95b] M. Leino, J. Äystö, T. Enqvist, A. Jokinen, M. Nurmia, A. Ostrowski, W.H. Trzaska, J. Uusitalo, K. Eskola, P. Armbruster and V. Ninov,
Acta Physica Polonica B **26**, 309 (1995)

[Lir76] S. Liran and N. Zeldes,
At. Data Nucl. Data Tables **17**, 431 (1976)

[Ma93] W.C Ma, J.H. Hamilton, A.V. Ramayya, L. Chaturvedi, J.K. Deng, W.B. Gao, Y.R. Jiang, J. Kormicki, X.W. Zhao, N.R. Johnson, J.D.

Garrett, I.Y. Lee, C. Baktash, F.K. McGown, W. Nazarewicz and R. Wyss,
Phys. Rev. C **47**, R5 (1993)

[May77] F.R. May, V.V. Pashkevich and S. Frauendorf
Phys. Lett. **68B**, 113 (1977)

[Meh91] D. Mehta, Y.K. Agarwal, K.P. Blume, S. Heppner, H. Hübel, M. Murzel, K. Theine, W. Gast, G. Hebbinghaus, R.M. Lieder and W. Urban,
Z. Phys. A **339**, 317 (1991)

[Miy87] H. Miyatake, T. Nomura, H. Kawakami, J. Tanaka, M. Oyaizu, K. Morita, T. Shinozuka, H. Kudo, K. Sueki and Y. Iwata,
Nucl. Instr. and Meth. B **26**, 309 (1987)

[Mos89] M. Moszyński, J.H. Bjerregard, J.J. Gaardhøje, B. Herskind, P. Knudsen and G. Sletten,
Nucl. Instr. and Meth. A **280**, 73 (1989),

[Mot55] B.R. Mottelson and S.G. Nilsson,
Phys. Rev. **99**, 1615 (1955)

[Mue99] W.F. Mueller, H.Q. Jin, J.M. Lewis, W. Reviol, L.L. Riedinger, M.P. Carpenter, C. Baktash, J.D. Garrett, N.R. Johnson, I.Y. Lee, F.K. McGowan, C.-H. Yu and S. Cwiok,
Phys. Rev. C **59**, 2009 (1999)

[Naz93] W. Nazarewicz,
Phys. Lett. B **305**, 195 (1993)

[Naz97] W. Nazarewicz, private communication

[New70] J.O. Newton, S.D. Cirilov, F.S. Stephens and R.M. Diamond,
Nucl. Phys. A 148, 593 (1970)

[Nil55] S.G. Nilsson,
Mat. Fys. Medd. Dan. Vid. Selsk. **29**(1955) No.16

[Nin99] V. Ninov and K.E. Gregorich,
ENAM98, edited by B.M. Sherrill, D.J. Morissey and C.N. Davids (AIP, Woodbury, 1999) p. 704
And http://bgsmc01.lbl.gov

[Nol85] P.J. Nolan, D.W. Gifford and P.J. Twin,
Nucl. Instr. and Meth. A **236**, 95 (1985),

[Pag96] R.D. Page, P.J. Woods, R.A. Cunningham, T. Davidson, N.J. Davids, A.N. James, K. Livingston, P.J. Sellin and A.C. Shotter,
Phys. Rev. C **53**, 660 (1996)

[Pau95] E.S. Paul, P.J. Woods, T. Davidson, R.D. Page, P.J. Sellin, C.W. Beausang, R.M. Clark, R.A. Cunningham, S.A. Forbes, D.B. Fossan, A. Gizon, J. Gizon, K. Hauschild, I.M. Hibbert, A.N. James, D.R. LaFosse, I. Lazarus, H. Schnare, J. Simpson, R. Wadsworth and M.P. Waring,
Phys. Rev. C **51**, 78 (1995)

[Pen87] J. Penninga, W.H.A. Hesselink, A. Balanda, A. Stolk, H. Verheul, J. van Klinken, H.J. Riezebos and M.J.A. de Voigt,
Nucl. Phys. **A471**, 535 (1987)

[Plo93] A.J.M. Plompen, M.N. Harakeh, W.H.A. Hesselink, G. van 't Hof, N. Kalantar-Nayestanaki, J.P.S. van Schagen, M.P. Carpenter, I. Ahmad, I.G. Bearden, R.V.F.Janssens, T.L. Khoo, T. Luaritsen, Y. Liang, U. Garg, W. Reviol and D. Ye,
Nucl. Phys. **A562**, 61 (1993)

[Pol99] G.L. Poli, C.N. Davids, P.J. Woods, D. Severyniak, J.C. Batchelder, L.T. Brown, C.R. Bingham, M.P. Carpenter, L.F. Conticchio, T. Davinson, J. DeBoer, S. Hamada, D.J. Henderson, R.J. Irvine, R.V.F. Janssens, H.J. Maier, L. Müller, F. Soramel, K.S. Toth, W.B. Walters and J. Wauters
Phys. Rev. C **59**, R2979 (1999)

[Por91] M.-G. Porquet, A.J. Kreiner, F. Hannachi, V. Vanin, G. Bastin, C. Bourgeois, J. Davidson, M. Debray, G. Falcone, A. Korichi, H. Mosca, N. Perrin, H. Sergolle, F.A. Beck and J.-C. Merdinger,
Phys. Rev. C **44**, 2445 (1991)

[Rad95] D.C. Radford,
Nucl. Instr. and Meth. A **361**, 297 and 306 (1995),

[Rev94] W. Reviol, L.L. Riedinger, J.-Y. Zhang, C.R. Bingham, W.F. Mueller, B.E. Zimmerman, R.V.F. Janssens, M.P. Carpenter, I. Ahmad, I.G. Bearden, R.G. Henry, T. L. Khoo, T. Lauritsen and Y. Liang
Phys. Rev. C **49**, R587 (1994)

[Rev00] W. Reviol, M.P. Carpenter, R.V.F. Janssens, D. Jenkins, K.S. Toth, C.R. Bingham, L.L. Riedinger, W. Weintraub, J.A. Cizewski, T. Lauritsen, D. Seweryniak, J. Uusitalo, I. Wiedenhöver, R. Wadsworth, A.N. Wilson, C.J. Gross, J.C. Batchelder, K. Helariutta and S. Juutinen
Phys. Rev. C **61**, 044310 (2000)

[Sar96] D.G. Sarantites, P.-F. Hua, M. Devlin, L.G. Sabotka, J. Elson, J. T. Hood, D.R. LaFosse, J.E. Sarantites and M.R. Maier
Nucl. Instr. and Meth. A **381**, 418 (1996)

[Sav98] A. Savelius,
Ph. D. thesis, University of Jyväskylä, Research report No. 9/1998 (unpublished)

[Sch80] U.J. Schrewe, P. Tidemand-Petersson, G.M. Gowdy, R. Kirchner, O. Klepper, A. Plochocki, W. Reisdorf, E. Roeckl, J.L. Wood, J. Żylicz, R. Fass and D. Schardt,
Phys. Lett. **91B**, 46 (1980)

[Sch84] K.-H. Schmidt, C.-C. Sahm, K. Pielenz and H.-G. Clerc
Z. Phys. A **316**, 19 (1984)

[Sch86] K.-H. Schmidt, R.S. Simon, J.-G. Keller, F.P. Heβberger, G. Münzenberg, B. Quint, H.-G. Clerc, W. Schwab, U. Gollerthan and C.-C. Sahm,
Phys. Lett. **168B**, 39 (1986)

[Sel91] P.J. Sellin, P.J. Woods, R.D. Page, S.J. Bennett, R.A. Cunningham, M. Freer, B.R. Fulton, M.A.C. Hotchkis and A.N. James,
Z. Phys. A **338**, 245 (1991)

[Sew99] D. Seweryniak, J. Uusitalo, M.P. Carpenter, D. Nisius, C.N. Davids, C. Bingham, L.T. Brown, L. Conticchio, D.J. Henderson, R.V.F. Janssens, W.B. Walters, J. Wauters and P.J. Woods
Phys. Rev. C **60**, 031304 (1999)

[Shi95] D.T. Shi, W.C. Ma, A.V. Ramayya, J.H. Hamilton, B.R.S. Babu, J. Kormicki, L. Chaturvedi, Q.H. Lu, L.T. Brown, S.L. Tabor, M.A. Riley, J. Döring, D.E. Archer, T. Brown, S.K. Jewell, R.A. Kaye, O.J. Tekyi-Mensah and P.B. Semmes
Phys. Rev. C **51**, 1720 (1995)

[Sim86] R.S. Simon, K.-H. Schmidt, F.P. Heβberger, S. Hlavac, M. Honusek, G. Münzenberg, H.-G. Clerc, U. Gollerthan and W. Schwab,
Z. Phys. A **325**, 197 (1986)

[Smi99] M.B. Smith, R. Chapman, J.F.C. Cocks, O. Dorvaux, K. Helariutta, P.M. Jones, R. Julin, S .Juutinen, H. Kankaanpää, H. Kettunen, P. Kuusiniemi, Y. Le Coz, M. Leino, D.J. Middleton, M Muikku, P. Nieminen, P. Rahkila, A. Savelius and K.-M. Spohr,
Eur. Phys. J. A **5**, 43 (1999)

[Tot89] K.S. Toth, D.M. Moltz and J.D. Robertson,
Phys. Rev. C **39**, 1150 (1989)

[Tot98] K.S. Toth, X.-J. Xu, C.R. Bingham, J.C. Batchelder, L.F. Conticchio, W.B. Walters, L.T. Brown, C.N. Davids, R.J. Irvine, D. Severyniak, J. Wauters and E.F. Zganjar,
Phys. Rev. C **58**, 1310 (1998)

[Tot99] K.S. Toth, C.R. Bingham, J.C. Batchelder, L.T. Brown, L.F. Conticchio, C.N. Davids, R.J. Irvine, D. Severyniak, D.M. Moltz, W.B. Walters, J. Wauters and E.F. Zganjar,
Phys. Rev. C **60**, 011302(R) (1999)

[Twi83] P.J. Twin,
Proc. Int. Conf. Nucl. Phys., Florence, 1983
Vol. II, 527 (1983)

[Uus97] J. Uusitalo, M. Leino, R.G. Allat, T. Enqvist, K. Eskola, P.T: Greenlees, S. Hurskanen, A. Keenan, H. Kettunen, P. Kuusiniemi, R.D. Page and W.H. Trzaska
Z. Phys. A **358**, 375 (1997)

[Var97] P.G. Varmette, D.T. Shidot, W.C. Ma, A.V. Ramayya, R.V.F. Janssens, C.N. Davids, J.H. Hamilton, I. Ahmad, H. Amro, B.R.S. Babu, B. Back, K.S. Bindra, D.J. Blumenthal, L.T. Brown, M.P. Carpenter, W.L. Croft, B. Crowell, S.M. Fischer, U. Garg, R.G. Henry, T. Ishii, T.L. Khoo, J. Kormicki, T. Lauritsen, C.J. Lister, D. Nisius, H. Penttilä, R.B. Piercey, J.A. Winger, S.J. Zhu and P.B. Semmes
Phys. Lett. B **410**, 103 (1997)

[Voi90] M.J.A. de Voigt, R. Kaczarowski, H.J. Riezebos, R.F. Noorman, J.C. Bacelar, M.A. Deleplanque, R.M. Diamond, F.S. Stephens, J. Sauvage and B. Roussière,
Nucl. Phys. **A507**, 472 (1990)

[Wau94] J. Wauters, N. Bijnens, P. Dendooven, M. Huyse, Han Yull Hwang, G. Reusen, J. von Schwarzenberg, P. Van Duppen, R. Kirchner and E. Roeckl,
Phys. Rev. Lett. **72**, 1329 (1994)

[Wau94] J. Wauters, N. Bijnens, H. Folger, M. Huyse, Han Yull Hwang, R. Kirchner, J. von Schwarzenberg and P. Van Duppen
Phys. Rev. C **72**, 2768 (1994)

[Wau97] J. Wauters, J.C. Batchelder, C.R. Bingham, D.L. Blumenthal, L.T. Brown, L.F. Conticchio, C.N. Davids, T. Davidson, R.J. Irvine, D. Severyniak, K.S. Toth, W.B. Walters, P.J. Woods and E.F. Zganjar,
Phys. Rev. C **55**, 1192 (1997)

[Woo92] J.L. Wood, K. Heyde, W. Nazarewicz, M. Huyse and P. Van Duppen,
Phys. Rep. **215**, 101 (1992)